Fluid Dynamics of Inlet Swirl Distortions for Turbofan Engine Research

Tamara Guimarães Bucalo

Dissertation submitted to the Faculty of the
Virginia Polytechnic Institute and State University
in partial fulfillment of the requirements for the degree of

Doctor of Philosophy
in
Mechanical Engineering

K. Todd Lowe, Chair
Walter F. O'Brien
Clinton L. Dancey
Aurélien Borgoltz
Wing F. Ng

March 20, 2018
Blacksburg, Virginia

Keywords: fluid dynamics, swirl distortion, inlet distortion, vortex dynamics, particle image velocimetry, turbomachinery, StreamVane

Fluid Dynamics of Inlet Swirl Distortions for Turbofan Engine Research

Tamara Guimarães Bucalo

(Abstract)

Significant effort in the current technological development of aircraft is aimed at improving engine efficiency, while reducing fuel burn, emissions, and noise levels. One way to achieve these is to better integrate airframe and propulsion system. Tighter integration, however, may also cause adverse effects to the flow entering the engines, such as total pressure, total temperature, and swirl distortions. Swirl distortions are angular non-uniformities in the flow that may alter the functioning of specific components of the turbomachinery systems. To investigate the physics involved in the ingestion of swirl, pre-determined swirl distortion profiles were generated through the StreamVane^{TM} method in a low-speed wind tunnel and in a full-scale turbofan research engine. Stereoscopic particle image velocimetry (PIV) was used to collect three-component velocity fields at discrete planes downstream of the generation of the distortions with two main objectives in mind: identifying the physics behind the axial development of the distorted flow; and describing the generation of the distortion by the StreamVane and its impact to the flow as a distortion generating device.

Analyses of the mean velocity, velocity gradients, and Reynolds stress tensor components in these flows provided significant insight into the driving physics. Comparisons between small-scale and full-scale results showed that swirl distortions are Mach number independent in the subsonic regime. Reynolds number independence was also verified for the studied cases. The mean secondary flow and flow angle profiles demonstrated that the axial development of swirl distortions is highly driven by two-dimensional vortex dynamics, when the flow is isolated from fan effects. As the engine fan is approached, the vortices are axially stretched and stabilized by the acceleration of the flow. The flow is highly turbulent immediately downstream of the StreamVane due to the presence of the device, but that vane-induced turbulence mixes with axial distance, so that the device effects are attenuated for distances greater than a diameter downstream, which is further confirmed by the turbulent length scales of the flow. These results provide valuable insight into the generation and development of swirl distortion for ground-testing environments, and establishes PIV as a robust tool for engine inlet investigations.

(349 words)

This work received support from NASA and NIA through Contract 2917. Additional support was offered by *Coordenação de Aperfeiçoamento de Pessoal de Nível Superior (CAPES).*

Fluid Dynamics of Inlet Swirl Distortions for Turbofan Engine Research

Tamara Guimarães Bucalo

(General Audience Abstract)

In order to improve performance of the next generation of aircraft, engineers are developing research that aims at reducing fuel consumption, improving the efficiency of engines, and also decreasing the levels of produced noise. There are several ways to achieve these goals, but significant effort has been focused on modifying the position of the engines on the aircraft to improve the properties of the airflow entering them. Computational simulations and small-scale tests have shown that this approach can be beneficial, while also showing that adverse effects to the properties of the air can be caused, affecting the behavior of the propulsion system. This current work makes use of a technique called StreamVane^{TM} to reproduce those modified airflows in laboratory testing environments in order to understand how that flow might behave in the inlet of an engine, and what effects it could cause. This helps scientists and engineers decide if those modifications to the engine would be worth the time and money investments to the aircraft even before a full-scale model of the aircraft is built. More specifically, this work is an experimental investigation of two different types of distortions to the inlet airflow that could be caused by the aforementioned novel aircraft configurations, or by existing ones that have not been fully described yet.

Dedication

To my family: Mãe, Vovó e Vovô.

“Ela me disse assim:
Meu filho, vá com Deus.
Que este mundo inteiro é seu.”

Acknowledgements

It isn't until you go through your hardest times that you know who your true friends are. Going through my PhD is no doubt the hardest thing I have ever done in my life. And I could not have done it without the help of several people, who deserve to be mentioned here.

I could not start this any other way than by thanking my advisor, Dr. K. Todd Lowe. He believed in me from day one, even when I did not believe in myself. He was the best mentor I could have asked for, and I am beyond grateful for all the contributions, the knowledge, and the guidance that he has given me in these past years. I also need to thank Dr. Walter F. O'Brien, who welcomed me into his laboratory, and supported me through these years. I further wish to thank my dissertation committee members Dr. Aurélien Borgoltz, Dr. Clint Dancey, and Dr. Wing Ng for the very valuable advice to improve the quality of my dissertation.

One of my mentors at VT deserves a special thank you. Dr. William 'Bill' Copenhaver, thank you for everything you have taught me and shared with me in these past few years. I am thankful for having you as a co-worker, as a mentor, as a running buddy, and most of all, as a friend. Thank you for simply being there for me, whenever things were easy, but also when things were hard (like in the final stretch of the 2017 Hokie Half Marathon).

Two people get their own special thank you paragraph. For being my friends, counselors, mentors, and role models: Dr. Tobias Ecker, and Dr. Daniel 'DR' Cadel. You guys inspired me to keep going, and seeing all you've achieved made me believe I could do it too. I knew it was going to be a hard way, but I am so glad to have had both of you by my side through it all, from the very first lab group meetings, up to my defense, and afterwards as well. I know you two are friends I will have with me my whole life, and I have grad school to thank for that.

Several people made my time in grad school more enjoyable, fun, and pleasant. And if it wasn't for grad school, I would never have met you all, and my life wouldn't be as fun. Tim and Em Pote, Marcie Stuber Geesey, Will George, Nick Molinaro (and Kristina), Tyler Vincent, Sean Shea, Dr. Liselle Joseph, Dr. 'Other' Dan, Kyle Daniel, Chi Young Moon (and Cindy, and Aurora), Anthony Millican, Agastya Neehar, Kara Crosser, Eric Rolfe, Dr. Ken Brown, Henry Murray, thank you so so much for everything! You made it all bearable. Dustin Frohnapfel, Justin Bailey, Caroline Kirk, Matt Savage, thanks for the help with engine PIV. Thank you to my dance family, TEVT, and Little Leapers, for giving me something to distract myself and not go crazy! Thank you to my Natty Boys, especially Nizar, Kevin, Will, Gavin, Jared, Donnie, and the karaoke regulars. And also thank you to my friends in Brazil, who understood I needed to leave to pursue my career, but have never left me.

Furthermore, I would like to thank NASA Langley, NASA Glenn, and CAPES for the financial

support during my studies. I have learned so much, and it was all because of these amazing research centers.

And last, but definitely not least, I have my family to thank: Mãe, obrigada por me apoiar durante todos esses anos, mesmo doendo em você estar longe de mim. Doeu em mim cada dia longe de você e do vovô, mas sem o apoio e o carinho de vocês, eu não seria nada do que eu sou hoje. Você é a mulher mais forte que eu já conheci, a melhor engenheira, e a minha maior inspiração. Você e a vovó me fazem querer acordar todo dia e ser uma mulher melhor do que no dia anterior. Eu amo vocês pra sempre, e dedico tudo que eu já conquistei ao amor que vocês duas me ensinaram a sentir.

E Pedro, meu marido, obrigada por tudo. Sem o seu apoio durante todos os segundos desses anos, eu jamais teria chegado até aqui. Você é o melhor companheiro que alguém poderia ter, e eu tenho a sorte de ser a sua esposa, e de olhar pra trás e ver tudo que nós construímos para a nossa família (e pra Arya e pra Luna) nesses anos. Obrigada!

Tamy Guimarães

March 2018

Contents

List of Figures

List of Tables

Attributions

Several professors and colleagues contributed to the research and writing contained in this dissertation. A brief description of their contributions is included below:

Dr. K. Todd Lowe is the primary advisor and committee chair for this research. He provided extensive guidance on the research plan and provided editorial revisions and advice on the analysis of the experimental data on all manuscripts.

Dr. Walter F. O'Brien is a committee member and Co-PI for this research. He provided extensive guidance on the research plan.

Dr. William W. Copenhaver is a research scientist at the Turbomachinery and Propulsion Laboratory. He provided numerous contributions to this work, especially in the experimental part and analysis of Chapter 4.

Dustin J. Frohnapfel is a fellow doctoral candidate, member of the Turbomachinery and Propulsion Laboratory. The analyses presented in Appendix A were developed jointly, and he is also an author of the paper from which those results were extracted.

[this page intentionally left blank]

1. Introduction

The work on this dissertation is focused on the aerodynamics and testing of propulsion system inlets subject to secondary flow distortions. The advancements in propulsion systems technologies rely heavily on increasing the efficiency of said systems, while reducing fuel consumption and noise emissions. Novel aircraft configurations often make use of boundary layer ingestion (BLI), which is a technique in which the engine is either embedded in the aircraft surface, or mounted very close to the surface. This allows for the low energy boundary layer to be ingested by the engine and energized, reducing the energy necessary for the propulsor to achieve the same level of thrust, and reducing drag. The net gain of BLI aircraft leads to reductions in fuel consumption and emissions.

The ingestion of a boundary layer is beneficial to the overall engine performance, but it also comes with adverse effects to the flow entering the engine. Different types of distortions are generated, which might ultimately influence the performance of the various stages of the turbofan engine. Total pressure and total temperature distortions in the inlets of engines have been well characterized by the turbomachinery community. Swirl distortions are angular distortions that may affect the performance of the engine by modifying the incidence angle of the flow in the blades of the engine, and generating a temperature distortion behind the compressor related to work variations. This type of distortion is very common in BLI applications, and has been the focus of more recent studies, both numerically and experimentally. Most of the experimental work that has been developed so far has made use of traditional engine instrumentation, such as pressure probes, but particle image velocimetry (PIV) has shown its benefits to this application, mainly due to being a less intrusive measurement technique, and also for providing higher spatial resolution, so it has also been used in distorted engine inlet research.

In parallel, the development of ground testing techniques is also a necessity in order to fully investigate the effects of such distortions in full-scale engines. Using the StreamVane technology, in combination with PIV, this work describes a unique approach to investigating the fluid dynamics of distorted flows in ducts, both in small-scale wind tunnels, and also in a full-scale research engine, under the influence of the turbofan system, and describing the turbulent characteristics of said flows.

1.1 Structure and Contents

This dissertation is divided into six chapters, described as follows:

Chapter 1 describes the structure of this dissertation and the contributions of the Ph.D. candidate to the scientific community during the development of her work.

Chapter 2 presents a literature review of the relevant theory behind the work.

Chapter 3 is the research study published in the AIAA Journal of Propulsion and Power, Vol 34, No. 2, pp 340-353, entitled "StreamVane Turbofan Inlet Swirl Distortion Generator: Mean Flow and Turbulence Structure", (doi: 10.2514/1.B36422). This was the first journal paper published on the StreamVane technology, and contains an in-depth description of the concept behind the StreamVane distortion generator, its dependence on Reynolds and Mach number, and highlights important properties of the experiments performed using this technology, including the application of PIV in the harsh environment of a full-scale turbofan engine.

Chapter 4 is a research study of a single-vortex fundamental type of inlet distortion, named "Experimental Investigation of Fundamental Vortical Flow Development across Scales". It will be submitted for publication in the journal Experiments in Fluids. This study analyzes the details of the axial development of a fundamental distorted flow in a small-scale duct, and in a full-scale environment.

Chapter 5 is the research study published in ASME Journal of Engineering for Gas Turbines and Power, entitled "Complex Flow Generation and Development in a Full-Scale Turbofan Inlet" (doi: 10.1115/1.4039179). This chapter focuses on the behavior of a highly complex distorted flow when developing in the inlet of a turbofan engine.

Chapter 6 summarizes the findings of the studies presented in this dissertation, and opens doors for possible future work that could arise from this.

Formatting of each chapter contents and citation style may deviate due to the different publication guidelines of the journal in which they have been published, or will be submitted to.

1.2 Achievements

Some primary accomplishments of this work are:

- Experiments were performed in two different scales, a low-speed wind tunnel, and a full-scale engine, which allowed for physical relationships between the two scales to be determined, such as Reynolds and Mach number independence.
- Particle Image Velocimetry was matured as a successful technique to investigate highly distorted flows inside the harsh environment of the Virginia Tech full-scale research engine.
- The development of the secondary distorted flow has been proved to be mostly dominated by two-dimensional (2D) vortex dynamics.
- The turbulent length scales of the StreamVane and the flow were also investigated, and it was concluded that the StreamVane can be used to generate distortions when positioned at least one diameter upstream of the measurement plane of interest.

1.2.1 Claims

The key contributions and main claims of this work are as follows:

- Swirl distortions are Reynolds number independent for flows ranging between 0.5 and 3 million. Flows with lower Reynolds numbers will likely be affected by viscous effects, influencing the behavior of those distortions, but the results of the theory used improve with increasing Reynolds number levels.
- Swirl distortions are Mach number independent for subsonic flows until the point where transonic levels are achieved locally over the vanes of the StreamVane.
- 2D vortex dynamics is the main driver of the secondary flow development. Turbulent diffusion also has a role in the flow development when engine effects are present.
- Turbulent length scales introduced to the flow by StreamVane devices are very small when compared to the turbulent length scales of the distorted flow, and their effects are negligible for distances above one diameter downstream of the StreamVane.

1.2.2 List of Publications

The scientific publications of the author during her Ph.D. work are listed in this section.

Peer-reviewed Journal Publications:

- T. Guimarães, K. T. Lowe, and W. F. O'Brien. The StreamVane turbofan inlet swirl distortion generator: mean flow and turbulence structure. In *Journal of Propulsion and Power.* Vol 34, No 2, pp. 340-353, 2018.
- T. Guimarães, K. T. Lowe, and W. F. O'Brien. Complex flow generation and development in a full-scale turbofan inlet. In *Journal of Engineering for Gas Turbines and Power.* doi: 10.1115/1.4039179

Conference Proceedings:

- T. Guimarães, K. T. Lowe, M. Nelson, W. F. O'Brien, and C. G. Kirk. Stereoscopic PIV measurements in a turbofan engine inlet with tailored swirl distortion. In *31st AIAA Aerodynamic Measurement Technology and Ground Testing Conference*, number AIAA 2015-2866, 2015.
- T. Guimarães, K. T. Lowe, and W. F. O'Brien. An overview of recent results using the StreamVane method for generating tailored swirl distortion in jet engine research. In *54th AIAA Aerospace Sciences Meeting*, number AIAA 2016-0534, 2016.
- T. Guimarães and K. T. Lowe. Application of fluorescent particles for particle tracking velocimetry in wind tunnels. In *Proceedings of the 18th International Symposium on the Application of Laser and Imaging Techniques to Fluid Mechanics*, 2016.
- T. Guimarães, W. W. Copenhaver, W. C. Schneck, K. T. Lowe, and W. F. O'Brien. Swirling Flow Evolution Part 1: Design and Stereo PIV Measurements at Select Planes. In *55th AIAA Aerospace Sciences Meeting*, number AIAA 2017-1620, 2017.
- W. C. Schneck, T. Guimarães, D. J. Frohnapfel, K. T. Lowe, W. F. O'Brien, and W. W. Copenhaver. Swirling Flow Evolution Part 2: StreamFlow 2D+t Model Validated with Stereo PIV Measurements. In *55th AIAA Aerospace Sciences Meeting*, number AIAA 2017-1622, 2017.
- T. Guimarães, K. T. Lowe, and W. F. O'Brien. Complex flow generation and development in a full-scale turbofan inlet. In *Proceedings of ASME Turbo Expo 2017*, number ASME GT2017-64756, 2017.
- T. Guimarães, D. J. Frohnapfel, K. T. Lowe, and W. F. O'Brien. Streamwise Development and Turbulence Characterization of a Twin-Vortex Inlet Distortion for Turbofan Applications. In *53rd AIAA/SAE/ASEE Joint Propulsion Conference, AIAA Propulsion and Energy*

Forum., number AIAA 2017-4992, 2017.

- T. Guimarães, A. Marin, C. J. Kähler, R. Barnkob. Acoustic-assisted fluidic hourglasses. In *Bulletin of the American Physical Society*, 2017.
- T. Guimarães, K. T. Lowe, and W. F. O'Brien. Particle Image Velocimetry for Distorted Turbofan Engine Inlet Applications. *Abstract accepted for the 19th International Symposium on the Application of Laser and Imaging Techniques to Fluid Mechanics*.

2. Literature Review

2.1 Turbofan Engine Inlet Distortion

The development of air-breathing engine technology relies heavily on successful and efficient integration between airframe and propulsion system of an aircraft. Boundary Layer Ingestion (BLI) is one of the main ways to increase the efficiency of modern engines, and it can be achieved by embedding the engine in the airframe or mounting the engine case very close to the aircraft surface, as shown in Figure 2.1, allowing for the low energy boundary layer to be ingested by the engine and energized (Smith, 1993; Felder et al., 2009; Greitzer et al., 2010). The net gain of BLI aircraft is a reduction in drag and required thrust, reducing, therefore, the fuel consumption and emissions (Daggett, 2002; Kawai et al., 2006). Studies have shown that the use of BLI can reduce fuel consumption in up to 10% (Daggett et al., 2003; Kawai et al., 2006; Owens et al., 2008).

Figure 2.1: Example of boundary layer ingesting aircraft concept *(Image courtesy NASA Langley)*

The ingestion of a boundary layer is beneficial to engine performance, but may also adversely affect the flow entering the engine. Nonuniformities in the flow may be generated, influencing the performance of the various stages of the turbomachinery components. Total pressure and total temperature distortions in the inlets of engines have been studied in depth and are very well characterized. Total pressure distortions will be briefly discussed in this section, and for a review of total temperature distortions, refer to Society of Automotive Engineers (2017b). Swirl distortions, the main object of this study, are a relatively new concern in the turbomachinery community, and are still not fully understood, so focus will be given to it in the following section.

Pressure and temperature distortions have been of interest for the turbomachinery community since the beginning of the development of turbo engines (Sussman, 1968; Robbins and Glaser,

1958; Katz, 1958; Farmer, 1972). These distortions influence the behavior of turbo engines by affecting the characteristics of the flow entering the system, and therefore changing the thermodynamic and aerodynamics relationships in the flow, mainly in the fan interactions and the first stages of the compressor. To investigate that, engine manufacturers developed their own metrics to evaluate the performance of engines subject to distortions, and the need for a unifying approach led to the creation of the Society of Automotive Engineers (SAE) S-16 Committee. An aerospace recommended practice (ARP) document was developed by this committee, entitled "Gas Turbines Inlet Flow Distortion Guidelines" (Society of Automotive Engineers, 1978). In this document, a set of new methods for assessing inlet distortion was presented. The document has been updated over the years to incorporate new best practices developed by the industry and academia, and remains as the main guide for the analysis of inlet distortions by the community.

Complex pressure distortions are generated in certain configurations of inlets, mainly due to growing boundary layers and adverse pressure gradients in the flow. To assess the effects of these in real engines, several methods to generate pressure distortions in laboratory scale have been developed, one of which is the use of compositions of meshes that increase local blockage in the flow, generating a pressure deficit equivalent to the one of interest (Beale et al., 2002). This technique has been used to assess pressure distortions for several years, and extensive research has been developed in the full-scale turbofan research engine located at the Virginia Tech Turbomachinery and Propulsion Laboratory (Ferrar and O'Brien, 2012; Lucas et al., 2014; Ferrar, 2015). Bailey and O'Brien (2013) recognized that most of these efforts focused on the analysis of the pressure distortions going through the compressor stage, but failed to address the upstream conditions of the distorted flow, identifying that the pressure distortions redistribute with the axial development of the flow, due to high pressure gradients.

2.1.1 Swirl Distortion

The third type of inlet distortion that is also of concern when analyzing turbo engine inlets is swirl. Swirl distortions are angular nonuniformities in the flow that may affect the performance of the engine by modifying the incidence angle of the flow in the blades of the engine (Fredrick and Davis, 2011), and generating a temperature distortion behind the compressor due to work variations (Genssler et al., 1987; Pazur and Fottner, 1991; Sheoran et al., 2009). This type of distortion is very common in BLI applications, and has been receiving more attention from the turbomachinery community in the recent years. Several computational investigations have been done ((Anderson and

Gibb, 1993; Sheoran et al., 2009, 2012)), and experimental work has been developed as well. One of the main challenges with experimental validation of the computational investigations is generating the equivalent distortion in the experimental environment. Several methods to generate swirl distortion have been developed throughout the years (Genssler et al., 1987; Sheoran et al., 2009; Lesser et al., 2010), and this work makes use of the StreamVane™ distortion generator, developed by Hoopes and O'Brien (2013). It consists of a cascade of pre-defined vanes that generate a predetermined swirl distortion in the experimental facility. Main achievements of the aforementioned investigations will be summarized and discussed in this chapter.

There are different types of swirl distortions that may arise from BLI or from ground vortex ingestion, shown in Figure 2.2 (Society of Automotive Engineers, 2017a). Furthermore, combinations of these types of swirl are very common, as is the case with the Hybrid Wing Body (HWB) inlet distortion, analyzed in Chapters 3 and 5, which consist of a combination of counterclockwise bulk swirl and a clockwise tightly-wound vortex.

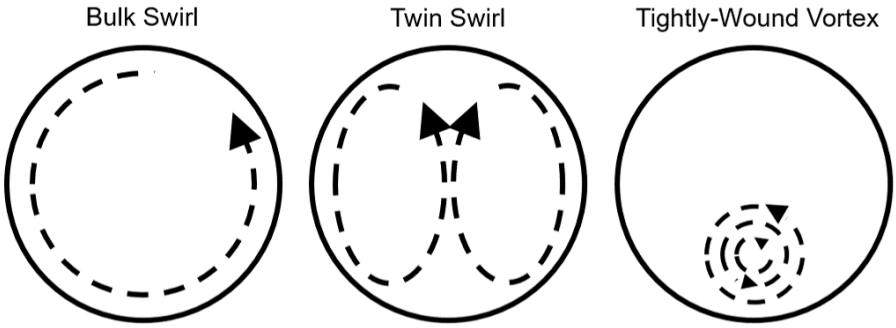

Figure 2.2: Types of swirl distortion.

These flow angularities may affect engine performance by modifying the angle of incidence on the rotor blade or inlet guide vane, modifying the velocity components of the velocity triangle that approaches the fan blades, and ultimately influencing the pressure rise or flow capacity of the fan or compressor stages (Fredrick, 2011; Society of Automotive Engineers, 2017a; Davis et al., 2002). Counter-rotating swirl causes an increase in work applied to the fluids, leading to greater loading of the blade and a reduction of stall margin, whereas co-rotating swirl causes a decrease in work, and increase in margin (Cousins, 2004). Inlet swirl may also decrease the performance of the compressor and generate a temperature distortion behind it due to work variations (Pazur and Fottner, 1991; Sheoran et al., 2009; Genssler et al., 1987).

Much of the efforts in this area have focused on the generation and control of secondary

flows in the inlets of engines. Anderson and Gibb (1993) used a Navier-Stokes code to develop a vortex generator to minimize inlet distortion by controlling the secondary flow. Davis and Hale (2007) developed a parametric study of the effects of bulk swirl and twin swirl in engine inlets, but acknowledged that their results should only be used as guides since they did not accompany any experimental results. Sheoran et al. (2012) developed a swirl generating model and used it to assess the affects it would have on compressor performance, showing that it significantly decreases for a co-rotating swirl and increases for counter-rotating swirl. This was also observed by Pardo et al. (2014) when simulating the ingestion of multiple tightly-wound vortices. Furthermore, they also observed a relationship between the number of vortices ingested and change in rotor performance. MacManus et al. (2017) have also numerically assessed the unsteady characteristics of distorted flow in full-scale engine applications.

Significant advancements have also been made in experimental work investigating swirl distortions. Small-scale investigations have been carried out by Genssler et al. (1987) and Gunn and Hall (2014), shedding light into the physics involved in swirl distortions, and aid in the confirmation of the simulation results presented previously. To fully identify the characteristics of the influence of swirl in real full-scale engines, ground tests have also been performed. Zachos et al. (2016) and Gil-Prieto et al. (2017) have experimentally observed the unsteadiness of distorted flows in full-scale engines described numerically by MacManus et al. (2017).

In summary, investigations of inlet swirl distortions are necessary to understand how they affect the turbomachinery performance. Frohnapfel has experimentally observed that swirl distortions survive through the engine fan, and are ingested by the following stages of the engine, having possible effects mainly in the first stages of the compressor and its performance (Frohnapfel et al., 2015, 2016, 2018). The present work focuses on the development of the distorted flow in the inlet before it reaches the fan and the subsequent stages of the engine, in order to describe the physics involved in the development of those distortions.

The StreamVane^{TM} Method

As mentioned previously, this work made use of the StreamVane technology to generate inlet swirl distortions in the experimental investigations. This technology was developed by Hoopes and O'Brien (2013) during a research project sponsored by NIA / NASA Langley, as part of the Environmentally Responsible Aviation (ERA) Project, with the main objective of being a tool for researchers and propulsion engineers to reproduce predetermined swirl distortions. Those dis-

tortions can be determined from computational studies of engine inlet flows, through small-scale experiments of aircraft models, or even from vortical flow models, as a single-vortex inlet distortion. This allows for real engine inlet flows to be reproduced in small experimental scales and in ground-testing facilities, so that engine behavior and safety can be analyzed before flight tests, at a lower cost.

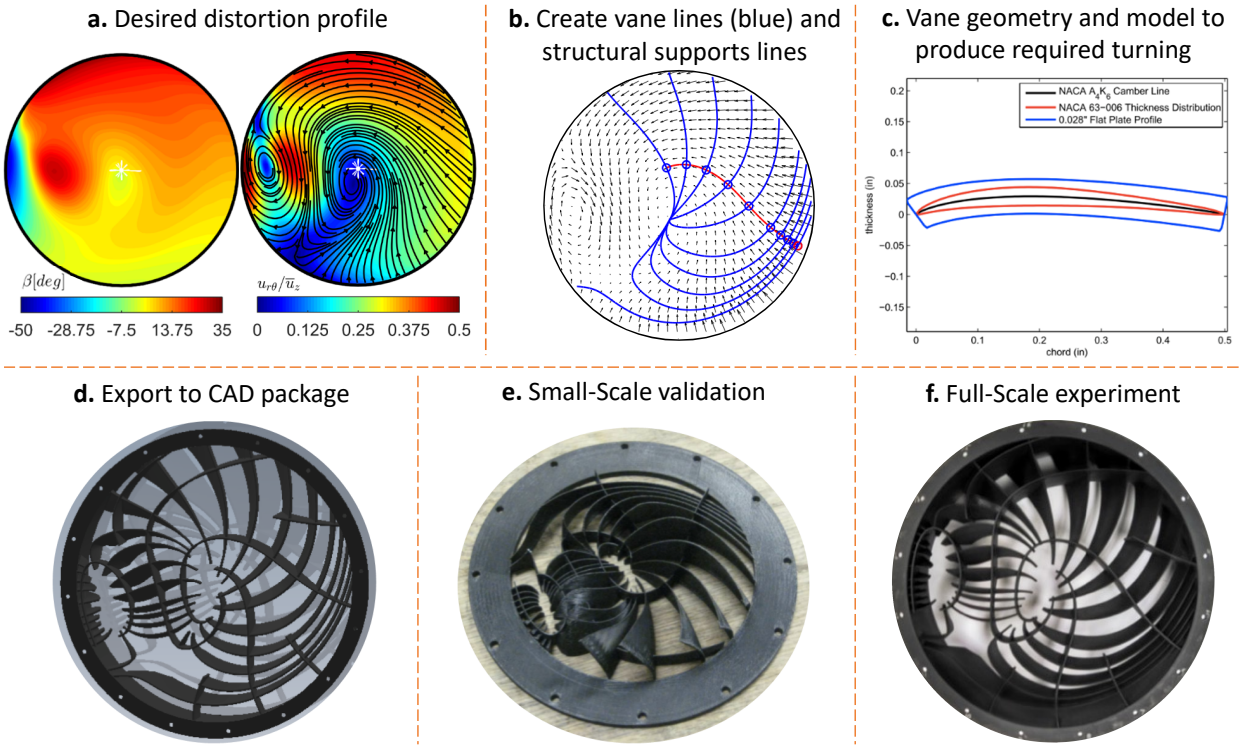

Figure 2.3: Steps to design a StreamVane™ swirl distortion generator.

The StreamVane consists of a manufactured screen with non-uniform turning vanes, positioned at a determined distance upstream of the fan face in a ground-testing research engine to generate swirl distortions. The process of designing and manufacturing a StreamVane starts with a known in-plane velocity profile and a swirl angle profile, such as the ones shown in Figure 2.3a, based on the inlet of an engine on a hybrid wing body (HWB) aircraft concept. Once the desired velocity profile has been determined, the turning vanes must be generated. For this, lines parallel to the velocity vectors are created at certain points defined by the user. Then, perpendicular lines are created in relation to the parallel lines at determined points, which may be uniformly spaced or not, depending on the velocity gradient in the profile. These lines are represented in blue in Figure 2.3b.

A study on vane geometry profiles was performed by Hoopes (2013) and, due to limitations in the additive manufacturing resources, an approximation to a flat plate profile was made and vanes were designed with constant thickness, as shown in Figure 2.3c. Solidity is set to be constant between all the vanes, yielding variable chord length vanes. The desired turning angles along the turning vanes are obtained from the determined profile, and the chord length of each vane is determined based on the parameters obtained in the previous step, leading to variable lengths across the StreamVane profile, as seen in Figure 2.3e.

Along with the turning vanes, structural support is added at chosen locations to interconnect the vanes and increase its rigidity and resistance to drag. The geometry of the supports is calculated in a similar manner as the turning vanes, except that in this case the original vector field is integrated at a single location per structural line. The vane profiles are then exported to a computer-aided design (CAD) package for solid body creation, flanging, and manufacturing. An automation script is applied to the geometry to automate the conversion of these profiles into solid bodies by sweeping the vane profiles along their corresponding vane lines, resulting in the 3D profile shown in Figure 2.3d.

After this step, the StreamVane is ready for manufacturing. A small-scale model, as shown in Figure 2.3e is printed for experimental validation of the manufactured profile in a low-speed wind tunnel. Once validation is completed, a full-scale StreamVane, as shown in Figure 2.3f is printed and used for experimental investigations in the inlet of a full-scale ground-testing engine.

2.2 Fluid Mechanics of Vortex-Dominated Flows

As described in the previous section, swirl distortions can be classified into three types, described by combinations of vortical flow features. Vortices are defined as compact regions of concentrated vorticity surrounded by irrotational fluid Saffman and Baker (1979).

Vortex-dominated flows are observed in numerous applications, across physical scales, from micro-flows in nature, to large atmospheric scales, as in tornadoes, and meteorologic applications. These flows hold fundamental interest due to the similarities of their behaviors across those scales. The work of Rockwell (1998) has confirmed the usefulness of Helmholtz's vortex theorems in practical flows such as the formation of leading-edge vortices on delta-wings and on the interaction of vortices with strain and surfaces. The scale independence of vortex-dominated flows is an important point to be noted about Rockwell's and others' work. Results from very low Reynolds

number experiments have been shown to match the aerodynamics encountered for full-scale vehicles since the phenomena can be scaled on geometry and circulation of the vortex, as shown in the Biot-Savart law (Saffman, 1992).

2.2.1 Vortex Dynamics

Vortex dynamics is the description of the behavior of vortical flows when subject to effects from other vortices, or to the self-induced velocity field (Saffman and Baker, 1979). Many have described mechanisms of vortex formation, but here focus will be given to vortices that are present in engine inlet applications. Inlet vortices can be formed via two different mechanisms: the headwind mechanism, in which the ambient vortex lines are intensified by being concentrated and stretched as flow is drawn into the engine inlet; and crosswind, when the vorticity associated with external surfaces is responsible for the vortex generation (De Siervi et al., 1982; Shin et al., 1986; Brix et al., 2000).

To investigate vortical flows, it is interesting to break complex flows into elementary ones, whose physics are described in a simpler manner. Karamcheti (1980) describes this procedure in detail in his book. Moore and Saffman (1971) described the basic theory on two-dimensional vortex interactions, including an analysis of the effects of disturbances in the development of the vortex. The majority of calculations of vortex interactions make use of a combination of point or discrete vortices to generate the flow field of interest (Saffman and Baker, 1979). There are several approaches to simplifying the description of vortical flows, as the ones presented by Leonard (1980) and Steger and Kutler (1977). When analyzing elementary flows, as an axial flow with a single-vortex distortion, for example, the flow may be generated by a two-dimensional single point vortex, with a flow field around it described by 2.1

$$W_c(x+iy) = u - iv = -\frac{\Gamma}{2i\pi}\frac{1}{x+iy} \tag{2.1}$$

where Γ is the circulation of the point vortex. For a twin-vortex distortion, the velocity field would be the sum of two point vortices, and for N vortices, the flow field would be described as 2.2.

$$W_c(x+iy) = \sum_{n=1}^{N} -\frac{\Gamma_n}{2i\pi}\frac{1}{x_n+iy_n} \tag{2.2}$$

Moore and Saffman (1971), Moore and Saffman (1975), and Acton (1976) performed inviscid calculations of vortices and interactions by simulating flows as a direct summation of point vortices. Chorin (1973) used the same method to describe interactions between a high-Reynolds number flow and a cylinder, including viscous effects. When generating an elementary flow, it is almost always necessary to also generate the bounds of the flow, whether it is a wall, a duct, or some solid body with which the flow will interact. This can be done by means of an image flow (Saffman and Baker, 1979). To calculate the induced velocity on a particular feature of the flow (e.g a single vortex), the complex velocity will take into account the flow generated by every flow feature, except the one that is being investigated.

The downstream development of simple vortical flows can be predicted by the calculation of the velocity induced by vortex lines, described by the Biot-Savart law, shown in the diagram in Figure 2.4, and described in 2.3 as presented by Leonard (1985).

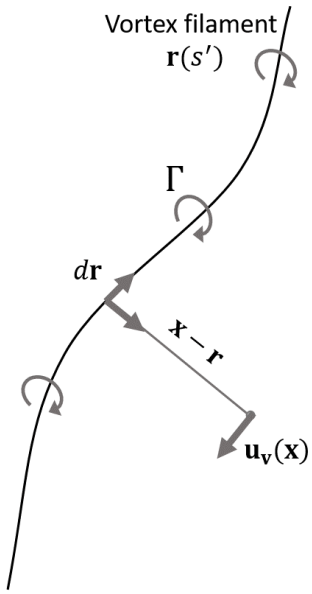

Figure 2.4: Velocity induced by a vortex filament as described by the Biot-Savart law.

$$\mathbf{u_v}(\mathbf{x}) = -\frac{\Gamma}{4\pi}\int_C \frac{\left[\mathbf{x}-\mathbf{r}\left(s'\right)\right]\times\frac{\partial \mathbf{r}}{\partial s'}ds'}{|\mathbf{x}-\mathbf{r}|^3} \tag{2.3}$$

where $\mathbf{u_v}$ is the velocity induced by a filamente of circulation Γ in an unbounded domain, with no interior boundaries. Tsien and Leesf (1945) broadened this analysis by deriving the components of the 3D induced velocity vector for a subsonic compressible flow. Equation 2.4 describes the

component $\mathbf{u}$ of the induced velocity field. Components $\mathbf{v}$ and $\mathbf{w}$ are analogous.

$$\mathbf{u_v}(\mathbf{x},\mathbf{y},\mathbf{z}) = \frac{1-M^2}{4\pi}\int \frac{\Gamma\left[(z-\mathbf{z})\,d\mathbf{y} - (y-\mathbf{y})\,d\mathbf{z}\right]}{\left\{(x-\mathbf{x})^2 + (1-M^2)\left[(y-\mathbf{y})^2 + (z-\mathbf{z})^2\right]\right\}^{3/2}} \tag{2.4}$$

2.2.2 Turbulence in Vortex-Dominated Flows

Most of the flows of interest for this work are of very high Reynolds number (above 1.5 million), which means that they present turbulent characteristics. Turbulence is characterized by the presence of coherent and incoherent instabilities in the flow, in several different scales. These flow structures can be described by means of vortex structures that either evolve internally or interact dynamically (Pullin and Saffman, 1998). The main goal of investigating these flows is to ultimately achieve the limit of infinite Reynolds number, where viscous effects are negligible, and the inviscid Euler equations describe the flow dynamics (Pullin and Saffman, 1998). Extensive literature has been published on the statistical analysis of turbulent flows (Pope, 2000; Bendat and Piersol, 2011).

When taking into consideration a single-vortex, studies have been performed on the turbulence characteristics around its development. Devenport et al. (1996) did an extensive experimental investigation of the turbulence involved in the development of a wing-tip vortex, concluding that outside of the core region of the vortex, the flow is dominated by the remaining effects of the wake, the edge of which is wound into a spiral by the rotation of the vortex. He also observed that, as one approaches the core of the vortex, there is a maximum in the turbulence at the beginning of the spiral structure, and that it grows with the streamwise development of the vortex, as sketched in Figure 2.5, eventually evolving into an approximately self-similar form. In situations where the axial flow surrounding the vortex is relevant, it has been observed that the axial stretching of vortices restricts the disturbances around it, and slows the development of turbulence (Moore and Saffman, 1971; Nolan, 2001). However, Delbende et al. (2002) has observed that the stretching of a vortex, if combined with the actions of vorticity in the azimuthal direction, may cause destabilization of the vortex, ultimately causing its breakdown.

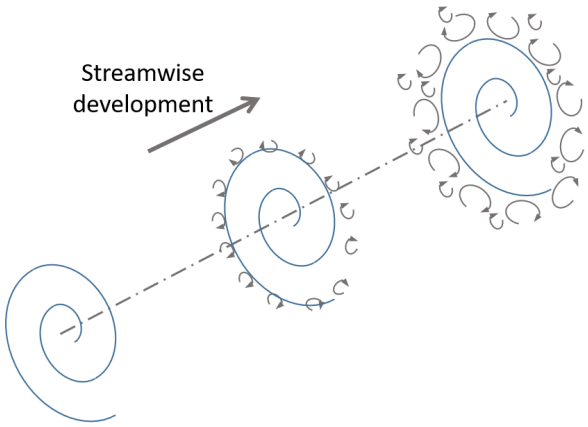

Figure 2.5: Sketch of turbulence growth during the streamwise development of a single-vortex.

2.3 Flow Measurement Techniques for Engine Inlets

There are several flow measurement techniques that can be used to experimentally determine velocities in a fluid flow. Choosing the most appropriate method for a certain application depends on what is being measured, and the characteristics of the experimental facility. Traditionally, the turbomachinery community makes use of pressure-based measurement techniques to determine the static pressure in certain locations of a flow, which after calibration, can be correlated to velocity measurements. These measurements are acquired by means of a pressure probe (e.g. pitot, 3-hole, 5-hole) that is inserted into the flow. This creates a disturbance in the flow, which may influence the measurements and create undesired effects.

One solution to that problem is to make use of non-intrusive measurement techniques, such as image- or laser-based techniques. Image-based techniques such as Schlieren flow visualization have been used in supersonic jet exhaust measurements (Mach and Salcher, 1890). As for laser-based techniques, Particle Tracking Velocimetry and Particle Image Velocimetry (PIV) are among the most used to measure fluid flows nowadays. They are not completely non-intrusive, however, since it is necessary to add small particles to the flow. These techniques and their benefits will be described further in this chapter.

2.3.1 Pressure-based Techniques

The Society of Automotive Engineers (SAE) S-16 Turbine Engine Inlet Flow Distortion Committee has determined several procedures and standards for acquiring data in distorted inlet flows. The most common way to experimentally measure this type of flow is by using pressure rakes, consisting of several rakes populated with pressure probes in one measurement plane, usually denominated Aerodynamic Interface Plane (AIP) . These pressure probes can provide information about the distortions present in the flow by measuring the static pressure at discrete positions. The ARP-1420 used a set of 8 rakes with 5 probes in each rake, because it provided a good data set distribution for the engines in which it was used at the time, since most of the distortion that was known was once-per-rev, due to their low bypass ratio and high length-to-diameter ratio inlets. (Society of Automotive Engineers, 1978)

However, with the advancing technologies in turbofan engine manufacturing and configuration, it is important to make sure that the measurement/probe locations will provide the manufacturer and the experimentalists with the most adequate and relevant data. For that, different combinations of rake and probe numbers can be used to better acquire information about the flow, while also ensuring that the instrumentation does not cause excessive blockage and disturbance of the flow. One way to maximize the acquisition of data is to rotate either the pressure rake or the pressure distortion, in the case that the distortion is generated by pressure screens, in relation to each other, as done by Bailey and O'Brien (2013); Frohnapfel et al. (2016); Ferrar and O'Brien (2012).

With the increasing interest in swirl distortions in engine inlets, it is not enough to obtain information about the static pressure at single probe locations. More advanced probes, such as 3-hole and 5-hole probes are preferred, since they have the capability of measuring static pressures at discrete locations around one central hole, which, by means of a probe calibration, are correlated with local flow angles. Through an automated measurement system, it is possible to plunge a complex probe radially into an engine inlet, and even behind the fan blades, to analyze how distortions interact with the fan, as done by Bailey (2016) and Frohnapfel et al. (2016, 2017).

2.3.2 Laser-based Techniques

Besides the traditional techniques, alternative approaches need to be taken when looking at different aspects of the flows of interest. There are several laser-based techniques that aim at minimizing

the intrusiveness of flow measurements, mainly by eliminating the necessity to insert probes into the flow.

Particle-based imaging methods are not non-intrusive *per se*, since they need to introduce particles into the flow, generating some disturbance. Besides, these technologies require modifications to test sections, in which it is necessary to insert windows to illuminate and image the flow. However, with the appropriate particle size to the flow of study, the impact has shown to be less than with traditional probes.

Particle Image Velocimetry

Particle image velocimetry is one of the most robust laser-based measurement techniques used nowadays. It has been under development for over 30 years (Adrian, 2005; Raffel et al., 2007), and the technology keeps developing with advances in computer processing capacity, resolution and speed of cameras, and laser power and speed.

The flow is seeded with particles sized appropriately to the flow, which should yield a Stokes number of less than 1, ensuring that they will follow the flow streamlines (Dring, 1982). Different types and sizes of particles are used, depending on the medium, and the velocity of the flow. For air flows, the most commonly used particles are either water or oil-based, ideally with sub-micron diameter sizes.

Sections of the flow are then illuminated with a laser sheet in short pulses with a determined time delay between them. The pulses are synchronized with the camera(s) trigger, so that images of the illuminated particles are captured. Using cross correlation algorithms, the raw images are processed to determine the particle displacement between the first and the second image frame, which yields velocity vectors of the local flow.

The main advantages of using PIV when compared with probe measurements are related to image resolution. While probes capture information about one specific location of the flow, instantaneous snapshots of the entire flow, or of large sections of the flow, can be captured with PIV. That allows experimentalists to extract information about instantaneous motions of the flow, including turbulence characteristics, depending on the speed of the system being used. High speed systems are able to capture time-resolved information of the flow, while low speed systems lack that ability, but can make use of statistical analysis to determine turbulent and random motions of the flow.

There are several challenges in applying PIV to the harsh environment of full-scale engine

experiments, mainly related to difficulties in seeding the flow, and in obtaining optical access to illuminate and image the flow. However, PIV has successfully been used as an engine inlet measurement technique in inlet flow investigations. Murphy et al. (2010); Murphy and MacManus (2011); Zachos et al. (2016); Gil-Prieto et al. (2017) have used PIV in full-scale configurations at Cranfield University, in the United Kingdom, to investigate different types of inlet distortions; and Schröder et al. (2014) have used PIV to perform an investigation of the flow in the inlet of the engine on a full-scale Airbus A320, in a special hangar at the airport of Hamburg, in Germany.

Summary

This chapter was intended to give a brief overview of the main concepts that are relevant for the development of the present work. Air-breathing propulsion technology development relies on successful integration between airframe and propulsion system, which provides several benefits for the efficiency of the aircraft, but also causes adverse effects, such as swirl distortions. These need to be characterized, so that the design process of new engines can be improved. The use of particle image velocimetry for flow measurements is beneficial due to the ability to collect instantaneous information about the flow to be used to calculate its turbulent characteristics.

Nomenclature

AIP	Aerodynamic Interface Plane
ARP	Aerospace recommended practice
BLI	Boundary Layer Ingestion
HWB	Hybrid Wing Body
PIV	Particle Image Velocimetry
SAE	Society of Automotive Engineers
C	space curve
i	imaginary unit number
n	index
M	Mach number
$\mathbf{r}(s')$	space curve of filament parameterized by arc length s'
$\mathbf{u_v}$	induced velocity

W_c	complex velocity field
x, y, z	cartesian coordinates
$\mathbf{x}, \mathbf{y}, \mathbf{z}$	cartesian vectors
Γ	circulation

References

E. Acton. The modelling of large eddies in a two-dimensional shear layer. *Journal of Fluid Mechanics*, 76(3):561–592, 1976. doi: 10.1017/S0022112076000785.

R. J. Adrian. Twenty years of particle image velocimetry. *Experiments in Fluids*, 39(2):159–169, 2005. doi: 10.1007/s00348-005-0991-7.

B. H. Anderson and J. Gibb. Study on vortex generator flow control for the management of inlet distortion. *Journal of Propulsion and Power*, 9(3):422–430, 1993. doi: 10.2514/3.23638.

J. Bailey and W. O'Brien. The Influence of Duct Development Distance on Screen-Generated Total Pressure Distortion Profiles. In *49th AIAA/ASME/SAE/ASEE Joint Propulsion Conference*, number AIAA 2013-3602, 2013. doi: 10.2514/6.2013-3602.

J. M. Bailey. *Full Scale Experimental Transonic Fan Interaction with a Boundary Layer Ingesting Total Pressure Distortion*. PhD thesis, Virginia Tech, 2016.

D. Beale, K. Cramer, and P. King. Development of Improved Methods for Simulating Aircraft Inlet Distortion in Turbine Engine Ground Tests (Invited). In *22nd AIAA Aerodynamic Measurement Technology and Ground Testing Conference*, number AIAA 2002-3045, 2002. doi: 10.2514/6.2002-3045.

J. Bendat and A. Piersol. *Random data: analysis and measurement procedures*. John Wiley & Sons, 2011. ISBN 978-0-470-24877-5.

S. Brix, G. Neuwerth, and D. Jacob. The inlet-vortex system of jet engines operating near the ground. In *18th Applied Aerodynamics Conference*, number AIAA 2000-3998, 2000. doi: 10.2514/6.2000-3998.

A. J. Chorin. Numerical study of slightly viscous flow. *Journal of Fluid Mechanics*, 57(04): 785–796, 1973. doi: 10.1017/S0022112073002016.

W. T. Cousins. History, philosophy, physics, and future directions of aircraft propulsion system/inlet integration. In *ASME Turbo Expo 2004*, number GT2004-54210, 2004. doi: 10.1115/GT2004-54210.

D. L. Daggett. Ultra Efficient Engine Technology Systems Integration and Environmental Assessment. Technical Report NASA/CR-2002-211754, NASA, 2002. URL https://ntrs.nasa.gov/archive/nasa/casi.ntrs.nasa.gov/20020064732.pdf.

D. L. Daggett, R. T. Kawai, and D. M. Friedman. Blended Wing Body Systems Studies: Boundary Layer Ingestion Inlets With Active Flow Control. Technical Report NASA/CR-2003-212670, NASA, 2003. URL https://ntrs.nasa.gov/archive/nasa/casi.ntrs.nasa.gov/20040031343.pdf.

M. Davis and A. Hale. A Parametric Study on the Effects of Inlet Swirl on Compression System Performance and Operability Using Numerical Simulations. In *ASME Turbo Expo 2007*, number ASME GT2007-27033, 2007. doi: 10.1115/GT2007-27033.

M. Davis, A. Hale, and D. Beale. An Argument for Enhancement of the Current Inlet Distortion Ground Test Practice for Aircraft Gas Turbine Engines. *Journal of Turbomachinery*, 124(2): 235–241, 2002. ISSN 0889504X. doi: 10.1115/1.1451087.

F. De Siervi, H. Viguier, E. Greitzer, and C. Tan. Mechanisms of inlet-vortex formation. *Journal of Fluid Mechanics*, 124:173–207, 1982. doi: 10.1017/S0022112082002456.

I. Delbende, M. Rossi, and S. Le Dizès. Stretching effects on the three-dimensional stability of vortices with axial flow. *Journal of Fluid Mechanics*, 454:419–442, 2002. doi: 10.1017/S0022112001007261.

W. J. Devenport, M. C. Rife, S. I. Liapis, and G. J. Follin. The structure and development of a wing-tip vortex. *Journal of Fluid Mechanics*, 312:67–106, 1996. doi: 10.1017/S0022112096001929.

R. P. Dring. Sizing criteria for laser anemometry particles. *Journal of Fluids Engineering*, 104(1): 15–17, 1982. doi: 10.1115/1.3240844.

C. J. Farmer. Inlet distortion, vorticity, and stall in an axial-flow compressor. Master's thesis, Naval Postgraduate School, 1972.

J. Felder, H. Kim, and G. Brown. Turboelectric Distributed Propulsion Engine Cycle Analysis for Hybrid-Wing-Body Aircraft. In *47th AIAA Aerospace Sciences Meeting*, number AIAA 2009-1132, 2009. doi: 10.2514/6.2009-1132.

A. Ferrar. *Measurement and Uncertainty Analysis of Transonic Fan Response to Total Pressure Inlet Distortion*. PhD thesis, Virginia Tech, 2015.

A. Ferrar and W. O'Brien. Fan Response to Total Pressure Distortions Produced by Boundary Layer Ingesting Serpentine Inlets. In *48th AIAA/ASME/SAE/ASEE Joint Propulsion Conference & Exhibit*, number AIAA 2012-3996, 2012. doi: 10.2514/6.2012-3996.

N. Fredrick. *Investigation of the Effects of Inlet Swirl on Compressor Performance and Operability Using a Modified Parallel Compressor Model*. PhD thesis, University of Tennessee, Knoxville, 2011.

N. Fredrick and M. Davis. Investigation of the Effects of Inlet Swirl on Compressor Performance and Operability Using a Modified Parallel Compressor Model. In *ASME Turbo Expo 2011*, number ASME GT2011-45553, 2011. doi: 10.1115/GT2011-45553.

D. J. Frohnapfel, W. F. O'Brien, and K. T. Lowe. Fan Response to Inlet Swirl Distortions Produced by Boundary Layer Ingesting Aircraft Configurations. In *51st AIAA/SAE/ASEE Joint Propulsion Conference*, number AIAA 2015-3804, 2015. doi: 10.2514/6.2015-3804.

D. J. Frohnapfel, A. M. Ferrar, J. Bailey, W. F. O'Brien, and K. T. Lowe. Measurements of Fan Response to Inlet Total Pressure and Swirl Distortions Produced by Boundary Layer Ingesting Aircraft Configurations. In *54th AIAA Aerospace Sciences Meeting*, number AIAA 2016-0533, 2016. doi: 10.2514/6.2016-0533.

D. J. Frohnapfel, W. F. O'Brien, and K. T. Lowe. Fan Rotor Flow Measurements in a Turbofan Engine Operating with Inlet Swirl Distortion. In *55th AIAA Aerospace Sciences Meeting*, number AIAA 2017-1623, 2017. doi: 10.2514/6.2017-1623.

D. J. Frohnapfel, K. T. Lowe, and W. F. O'Brien. Experimental Quantification of Fan Rotor Effects on Inlet Swirl Using Swirl Distortion Descriptors. *Journal of Engineering for Gas Turbines and Power*, 2018. doi: 10.1115/1.4039425.

H. P. Genssler, W. Meyer, and L. Fottner. Development of Intake Swirl Generators for Turbo Jet Engine Testing. In *Conference Proceedings of the Propulsion and Energetics Specialists' Meeting*, 1987.

D. Gil-Prieto, D. G. MacManus, P. K. Zachos, G. Tanguy, and K. R. Menzies. Convoluted Intake Distortion Measurements Using Stereo Particle Image Velocimetry. *AIAA Journal*, 55(6):1878–1892, 2017. doi: 10.2514/1.J055467.

E. Greitzer, P. Bonnefoy, E. D. la Rosa Blanco, C. Dorbian, M. Drela, D. Hall, R. Hansman, J. Hileman, R. Liebeck, J. Lovegren, P. Mody, J. Pertuze, S. Sato, Z. Spakovszky, C. Tan, J. Hollman, J. Duda, N. Fitzgerald, J. Houghton, J. Kerrebrock, G. Kiwada, D. Kordonowy, J. Parrish, J. Tylko, E. Wen, and W. Lord. N+3 Aircraft Concept Designs and Trade Studies, Final Report, Volume 1. Technical report, NASA Contractor Report, 2010. URL https://ntrs.nasa.gov/search.jsp?R=20100042401.

E. J. Gunn and C. A. Hall. Aerodynamics of Boundary Layer Ingesting Fans. In *ASME Turbo Expo 2014*, number ASME GT2014-26142, 2014. doi: 10.1115/GT2014-26142.

K. M. Hoopes. The StreamVane Method: A New Way to Generate Swirl Distortion for Jet Engine Research. Master's thesis, Virginia Tech, 2013.

K. M. Hoopes and W. F. O'Brien. The StreamVane Method: A New Way to Generate Swirl Distortion for Jet Engine Research. In *49th AIAA/ASME/SAE/ASEE Joint Propulsion Conference*, number AIAA 2013-3665, 2013. doi: 10.2514/6.2013-3665.

K. Karamcheti. *Principles of Ideal-Fluid Aerodynamics*, chapter Two-dimensional motion and the complex variable, pages 444–458. Krieger Pub Co, 1980. ISBN 0898741130.

R. Katz. Performance of axial compressors with asymmetric inlet flows. Technical Report TR-58-89, Air Force Office of Scientific Research, 1958. URL http://resolver.caltech.edu/CaltechAUTHORS:20151105-165306203.

R. T. Kawai, D. M. Friedman, and L. Serrano. Blended Wing Body (BWB) Boundary Layer Ingestion (BLI) Inlet Configuration and System Studies. Technical Report NASA/CR-2006-214534, NASA, 2006. URL https://ntrs.nasa.gov/archive/nasa/casi.ntrs.nasa.gov/20070006754.pdf.

A. Leonard. Vortex methods for flow simulation. *Journal of Computational Physics*, 37(3):289–335, 1980. doi: 10.1016/0021-9991(80)90040-6.

A. Leonard. Computing three-dimensional incompressible flows with vortex elements. *Annual Review of Fluid Mechanics*, 17(1):523–559, 1985. doi: 10.1146/annurev.fl.17.010185.002515.

A. Lesser, S. Schulze, R. Niehuis, C. J. Kähler, and J. Lieser. *New Results in Numerical and Experimental Fluid Mechanics VIII*, chapter Analytical Design of an Inlet Distortion Generator and Its Experimental and Numerical Validation, pages 33–41. Springer, 2010. ISBN 978-3-642-35680-3. doi: 10.1007/978-3-642-35680-3_5.

J. R. Lucas, W. F. O'Brien, and A. M. Ferrar. Effect of BLI–Type Inlet Distortion on Turbofan Engine Performance. In *ASME Turbo Expo 2014*, number ASME GT2014-26666, 2014. doi: 10.1115/GT2014-26666.

E. Mach and P. Salcher. Optische untersuchung der luftstrahlen. *Annalen der Physik und Chemie*, 277(9):144–150, 1890. doi: 10.1002/andp.18902770910.

D. G. MacManus, N. Chiereghin, D. G. Prieto, and P. Zachos. Complex Aeroengine Intake Ducts and Dynamic Distortion. *AIAA Journal*, 55(7):2395–2409, 2017. doi: 10.2514/1.J054905.

D. W. Moore and P. G. Saffman. Structure of a line vortex in an imposed strain. In *Aircraft Wake Turbulence and Its Detection*, pages 339–354. Springer US, 1971. doi: 10.1007/978-1-4684-8346-8_20.

D. W. Moore and P. G. Saffman. The density of organized vortices in a turbulent mixing layer. *Journal of Fluid Mechanics*, 69(3):465–473, 1975. doi: 10.1017/S0022112075001528.

J. P. Murphy and D. G. MacManus. Ground vortex aerodynamics under crosswind conditions. *Experiments in Fluids*, 50(1):109–124, 2011. doi: 10.1007/s00348-010-0902-4.

J. P. Murphy, D. G. MacManus, and C. T. Sheaf. Experimental Investigation of Intake Ground Vortices During Takeoff. *AIAA Journal*, 48(3):688–701, 2010. doi: 10.2514/1.45896.

D. S. Nolan. The stabilizing effects of axial stretching on turbulent vortex dynamics. *Physics of Fluids*, 13(6):1724–1738, 2001. doi: 10.1063/1.1370390.

L. R. Owens, B. G. Allan, and S. A. Gorton. Boundary-Layer-Ingesting Inlet Flow Control. *Journal of Aircraft*, 45(4):1431–1440, 2008. doi: 10.2514/1.36989.

A. C. Pardo, A. Mehdi, V. Pachidis, and D. G. MacManus. Numerical Study of the Effect of Multiple Tightly-Wound Vortices on a Transonic Fan Stage Performance. In *ASME Turbo Expo 2014*, number ASME GT2014-26481, 2014. doi: 10.1115/GT2014-26481.

W. Pazur and L. Fottner. The Influence of Inlet Swirl Distortions on the Performance of a Jet Propulsion Two-Stage Axial Compressor. *Journal of Turbomachinery*, 113(2):233, 1991. doi: 10.1115/1.2929091.

S. B. Pope. *Turbulent Flows*. Cambridge University Press, 2000. ISBN 9780511840531. doi: 10.1017/CBO9780511840531.

D. Pullin and P. Saffman. Vortex Dynamics in Turbulence. *Annual Review of Fluid Mechanics*, pages 31–51, 1998. doi: 10.1017/CBO9780511624063.

M. Raffel, C. Willert, S. Wereley, and J. Kompenhans. *Particle Image Velocimetry: A Practical Guide*. Springer Berlin Heidelberg, 2 edition, 2007. ISBN 978-3-540-72307-3. doi: 10.1007/978-3-540-72308-0.

W. Robbins and F. Glaser. Experimental investigation of the effect of circumferential inlet flow distortion on the performance of a five-stage axial flow research compressor with transonic rotors in all stages. Technical Report NACA RM E57J17, 1958. URL `https://ntrs.nasa.gov/archive/nasa/casi.ntrs.nasa.gov/19930090098.pdf`.

D. Rockwell. VORTEX-BODY INTERACTIONS. *Annual Review of Fluid Mechanics*, 30:199–229, 1998. doi: 10.1146/annurev.fluid.30.1.199.

P. Saffman. *Vortex Dynamics*. Cambridge University Press, 1992. ISBN 0-521-477395.

P. G. Saffman and G. R. Baker. Vortex Interactions. *Annual Review of Fluid Mechanics*, 11(1): 95–121, 1979. doi: 10.1146/annurev.fl.11.010179.000523.

A. Schröder, R. Geisler, D. Schanz, J. Agocs, D. Pallek, M. Scholl, J. Klinner, M. Beversdorff, M. Voges, and C. Willert. Application of image based measurement techniques for the investigation of aeroengine performance on a commercial aircraft in ground operation. In *17th International Symposium on Applications of Laser Techniques to Fluid Mechanics*, 2014.

Y. Sheoran, B. Bouldin, and P. M. Krishnan. Advancements in the Design of an Adaptable Swirl Distortion Generator for Testing Gas Turbine Engines. In *ASME Turbo Expo 2009*, number ASME GT2009-59146, 2009. doi: 10.1115/GT2009-59146.

Y. Sheoran, B. Bouldin, and P. M. Krishnan. Compressor Performance and Operability in Swirl Distortion. *Journal of Turbomachinery*, 134(4):041008, 2012. doi: 10.1115/1.4003657.

H. W. Shin, W. K. Cheng, E. M. Greitzer, and C. S. Tan. Inlet vortex formation due to ambient vorticity intensification. *AIAA Journal*, 24(4):687–689, 1986. doi: 10.2514/3.9330.

L. H. Smith. Wake ingestion propulsion benefit. *Journal of Propulsion and Power*, 9(1):74–82, 1993. doi: 10.2514/3.11487.

S. Society of Automotive Engineers. Gas Turbine Engine Inlet Flow Distortion Guidelines. Technical Report ARP 1420, SAE, 1978. URL https://saemobilus.sae.org/content/arp1420.

S. Society of Automotive Engineers. A Methodology for Assessing Inlet Swirl Distortion. Technical Report AIR 5686, SAE, 2017a. URL https://doi.org/10.4271/AIR5686http://standards.sae.org/air5686/.

S. Society of Automotive Engineers. Assessment of the inlet/engine total temperature distortion problem. Technical Report AIR5867, SAE, 2017b. URL https://www.sae.org/standards/content/air5867/.

J. L. Steger and P. Kutler. Implicit finite-difference procedures for the computation of vortex wakes. *AIAA Journal*, 15(4):581–590, 1977. doi: 10.2514/3.60663.

M. B. Sussman. A remark concerning engine-inlet distortion. *Journal of Aircraft*, 5(1):95–96, 1968. doi: 10.2514/3.43914.

H. Tsien and L. Leesf. The glauert-prandtl approximation for subsonic flows of a compressible fluid. *Journal of the Aeronautical Sciences*, 12(2):173–187, 1945. doi: 10.2514/8.11219.

P. K. Zachos, D. G. MacManus, D. G. Prieto, and N. Chiereghin. Flow Distortion Measurements in Convoluted Aeroengine Intakes. *AIAA Journal*, 54(9):2819–2832, 2016. doi: 10.2514/1.J054904.

3. StreamVane Turbofan Inlet Swirl Distortion Generator: Mean Flow and Turbulence Structure

The contents of this chapter were published in *AIAA Journal of Propulsion and Power* (Tamara Guimarães, K. Todd Lowe, and Walter F. O'Brien. "StreamVane Turbofan Inlet Swirl Distortion Generator: Mean Flow and Turbulence Structure", J Prop Power. 34(2):340-353. doi: 10.2514/1.B36422).

Significant portions were previously presented as "Tamara Guimarães, K. Todd Lowe, Michael Nelson, Walter F. O'Brien, and Caroline Kirk. Stereoscopic PIV measurements in a turbofan engine inlet with tailored swirl distortion. In *31st AIAA Aerodynamic Measurement Technology and Ground Testing Conference*, number AIAA 2015-2866, 2015. doi: 10.2514/6.2015-2866".

StreamVane Turbofan Inlet Swirl Distortion Generator: Mean Flow and Turbulence Structure

Tamara Guimarães,* K. Todd Lowe,† and Walter F. O'Brien‡
Virginia Polytechnic Institute and State University, Blacksburg, Virginia 24061-0203

DOI: 10.2514/1.B36422

Engine/airframe integration in advanced aircraft concepts must account for nonuniform flows ingested by turbofan engines. In this work, flow details from a vane-based distortion generator were analyzed for turbulence structure and aerodynamic scaling of the mean flow. Experimental results were obtained using particle image velocimetry in a small-scale facility and a full-scale research turbofan engine for the same vane geometry. Tests were performed at nearly the same Mach number to isolate Reynolds number effects, but analysis and prior work indicate that the flow development downstream of the vanes is Mach number independent in the subsonic regime. As hypothesized from inviscid vortex dynamics, the secondary mean flow angles were consistent across scales, indicating Reynolds number independence of the large-scale secondary flow profile generated. Vane wakes produced a complex structure in the streamwise velocity component not seen in the streamwise vorticity, which resembles the distribution from the desired secondary flow profile. The most intense turbulence is concentrated in the outer radial regions of the duct and, as shown by contrast to vane wake-dominated regions, is dominated by shear flow turbulence and unsteadiness due to the distortion profile itself rather than vane wakes. Taken together, these results provide fundamental understanding of the aerodynamics of swirling flows needed for implementing complex turning vanes in the design of distortion generators.

Nomenclature

D	=	duct diameter, m
L	=	integral length scale, mm
l	=	wavelength
M_∞	=	freestream Mach number
Q	=	peak ratio
Re	=	Reynolds number
Re_{L_T}	=	transition length Reynolds number
U	=	fan rotation velocity
u_r, u_v, u_x, u_z, u_θ	=	radial, vertical, horizontal, axial, and azimuthal velocity, m/s
u'_y	=	secondary velocity fluctuations
u'_z	=	velocity fluctuations in the axial direction
u'_θ	=	fluctuations in the azimuthal velocity component, m/s
$\overline{u'_i u'_i}$	=	normal component of Reynolds stress tensor
$\overline{u'_i u'_j}$	=	shear component of Reynolds stress tensor
w	=	relative velocity
α	=	flow angle
β	=	angle of relative velocity vector
$\delta(\cdot)$	=	uncertainty in a given quantity
θ	=	swirl angle, deg
ν	=	kinematic viscosity, m^2/s
ρ_{ij}	=	Reynolds shear stress correlation coefficient
σ	=	standard deviation
ϕ	=	velocity potential
ω	=	streamwise vorticity, s^{-1}

Presented as Paper 2016-0534 at the 54th AIAA Aerospace Sciences Meeting, San Diego, CA, 4–8 January 2016; received 11 August 2016; revision received 1 June 2017; accepted for publication 19 September 2017; published online 30 October 2017.

*Graduate Research Assistant, Mechanical Engineering, 100S Randolph Hall, CAPES Grantee. Student Member AIAA.

†Associate Professor, Crofton Department of Aerospace and Ocean Engineering, 215 Randolph Hall. Associate Fellow AIAA.

‡J. Bernard Jones Endowed Professor, Mechanical Engineering, 100S Randolph Hall. Fellow AIAA.

I. Introduction

CONCENTRATED interest in the effects of inlet swirl distortion on fan and compressor performance and operability persists [1–5] and will continue to be of critical importance as aircraft engine/airframe systems technology evolves. Despite its importance in affecting rotor performance and aeromechanics, flow distortion due to swirl, perceived as flow angle nonuniformities and characterized by the angle between the azimuthal and the axial velocity of the flow, have received little systematic study. As noted by the Society of Automotive Engineers (SAE) S-16 Turbine Engine Inlet Flow Distortion Committee [6], there are several classical case studies illustrating the need to consider not just total pressure and temperature distortions but also swirl during operability assessments. The azimuthal velocity component strongly affects the angle of incidence on a rotor blade or inlet guide vane and can therefore strongly influence the pressure rise or flow capacity of the fan or compressor stages [6]. However, even the standards for characterizing swirl distortions are lagging in detail compared with the well-established standards for pressure distortion. For instance, the SAE S-16 committee has set as the standard a parameter based upon azimuthally integrated swirl angle [6]. Such characterization ignores local effects of high turning that cause major changes in unsteady rotor loading.

The need for understanding swirl impact on rotor performance has led to studies involving computational and experimental approaches to simulate and analyze the behavior of turbomachines. It has been experimentally observed that inlet swirl distortion decreases the performance of a compressor and generates a temperature distortion behind it due to work variations [3,7,8]. Nonuniformities present in inlet flows affect efficiency by modifying the velocity components of the velocity triangle that approaches the fan blades, as shown in Fig. 1 [9]. Because distorted inflows are characteristically inhomogeneous in the azimuthal direction, the rotor design will not account for instantaneous flow angle changes. As depicted in Fig. 1, the primary effect of swirl is a shift in work done by the rotor. The shift may be an increase in work applied to the fluid, causing a greater loading of the blade and a reduction of stall margin, or a decrease in work and an increase in margin. Either case affects performance in complex ways and, in the extreme, will cause stall of the rotor.

Because of difficulty in performing flight tests for swirl distortion effects on engine performance, ground testing is a necessity. Most of the existing inlet swirl analysis has been done with computational fluid dynamics [7,10,11], tests employing pressure probes [12,13], or cascade experiments [14]. These approaches are able to give an overall

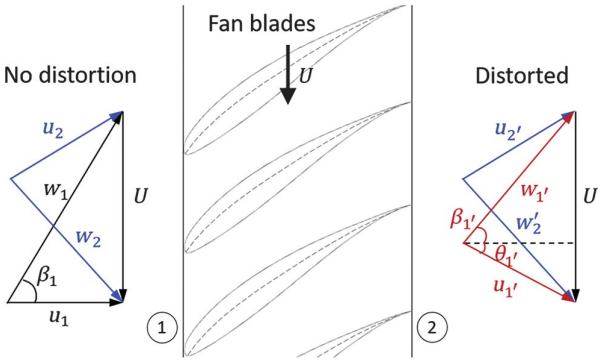

Fig. 1 Velocity triangles for flow approaching the fan of a turbofan engine with a uniform incoming flow (left) and with a distorted incoming flow (right). Station 1 is inlet, station 2 is right downstream of the fan. Swirl angle is θ, w is the relative velocity vector, and relative velocity vector angle is represented by β.

idea of the mean flow but have limitations regarding the turbulence details and the spatial resolution of the measurements in engine environments. Utilizing stereoscopic particle image velocimetry (PIV) in this type of problem, despite being more complicated in its implementation, allows for turbulence and unsteadiness details of the flow to be observed [15,16].

In this present work, a detailed analysis of the flow generated downstream of a distortion device manufactured through the StreamVane™ method [12] and measured by PIV was performed. This is a valuable development in ground testing environments, due to the flexibility of the designs of the StreamVane, allowing for virtually any swirl profile to be generated, and to the advances in instrumentation and measurement capabilities linked to the use of PIV. An analysis of the flow produced by the distortion screen in the engine inlet is presented in the Results section to assess how well the mean swirl profiles compare to the small-scale results, to describe high-order effects to the flow of the StreamVane swirl distortion, and to describe the behavior of the nonuniform flow as it approaches the fan.

II. Methods

A. Swirl Distortion for Engine Ground Testing: StreamVane

In past work [12,13,17–19], the authors have presented a new method for producing swirl distortion for engine ground tests. Depicted in Fig. 2 at the far right, the device uses a multivane architecture to produce spatially varying swirl distributions. The StreamVane method begins with a desired flow distortion pattern that may have been obtained from a computational fluid dynamics (CFD) simulation or from experimental results. Based upon the swirl pattern, an algorithm produces a vane distribution using advanced additive manufacturing techniques, up to full-scale engine test sizes. The resulting device consists of nonuniform vanes with varying turning. The underlying assumption of the aerodynamic design method is that the flow around a vane with dissimilar neighbors will be similar to the flow around a vane where all of its neighbors are alike [12]. In the current tests, the vane profile was composed of the NACA A_4K_6 airfoil with a constant thickness of 0.71 mm (0.028 in.) for simplified manufacturing. Past work has shown [18] that the method is able to reproduce complex swirl profiles in both intensity (swirl angle) and pattern (in-plane/secondary vector field) with a root mean square (RMS) error in swirl angle of less than 4 deg. In the present work, the flow details of swirl field reproduction were considered further. For more details concerning the StreamVane method of generating swirl inlet distortion, see the theses by Hoopes [12] and Nelson [18].

B. Small-Scale PIV Rig

The "hybrid wing body" (HWB) StreamVane design (named for the NASA airframe concept [20], which can produce such an inflow on aft-mounted engines) was tested with a 6-in.-diam distortion screen at a low-speed wind tunnel with a 12×12 in. square outlet, pictured in Fig. 3 [21]. A nozzle was used to connect the square outlet of the tunnel to the 6 in. thermoplastic pipe. The screen was placed and secured by bolts to the measurement test section. This setup did not have a fan to simulate possible effects to the full-scale flow.

A 6 in. inner diameter, 0.125 in. wall thickness acrylic pipe was used for the measurement section, with optical clearness good enough to allow internal measurements of the flow. Axial bulk velocity for this setup was 50 m/s (164 ft/s, Mach 0.14), duct diameter D was 0.15 m (6 in.) and ν at 300 K was 1.57×10^{-5} m^2/s, yielding a duct diameter Reynolds number of 0.5 million. A summary of the flow properties and the characteristics of the equipment used for this work is presented in Tables 1 and 2.

Images were illuminated with a double-pulsed 532 nm neodymium-doped yttrium aluminum garnet laser, rated at 120 mJ/pulse, and a −20 mm cylindrical lens was used to form the laser sheet positioned at $1.375D$ downstream of the trailing edge of the StreamVane vanes. Two LaVision Imager pro X 4M cameras, with charge-coupled device (CCD) size of 2048×2048 pixels (with pixel size of 7.4×7.4 μm^2), and quantum efficiency of 0.55, equipped with 50 mm Nikon lenses and Scheimpflug adapters, were placed on tripods, facing the flow upstream in an angle of approximately 60 deg relative to the flow centerline and 90 deg to the laser sheet plane. A LaVision seeder was used to atomize seed from di-ethylhexyl-sebacate (DEHS) oil, yielding particles of an average diameter of 1 μm. The flow was seeded from upstream of the StreamVane, in the suction side of the wind tunnel. One thousand images were taken at a 2.5 Hz frame rate to record the flow dynamics with this screen in place. The images were acquired and processed with the DaVis 8.3.0 software and further postprocessing was done in MATLAB. One pixel unit was equivalent to 0.0713 mm (0.0028 in.) in actual flowfield distance for this configuration. The spatial resolution of the interrogation window used was 9.09 mm (0.358 in.).

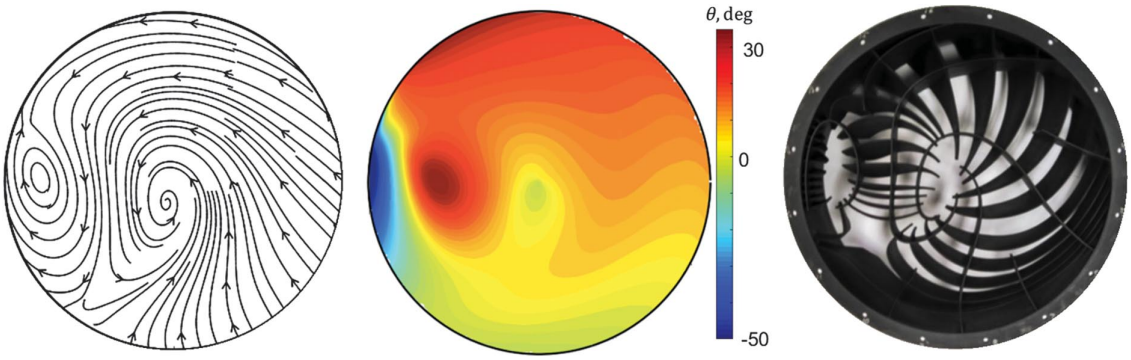

Fig. 2 CFD simulation results for the in-plane/secondary velocities (left), the swirl angle experienced by the flow in a hybrid wing body engine inlet (center), and the StreamVane designed to produce a similar swirl distortion (right). Plots are presented throughout the paper from a forward looking aft (FLA) point of view.

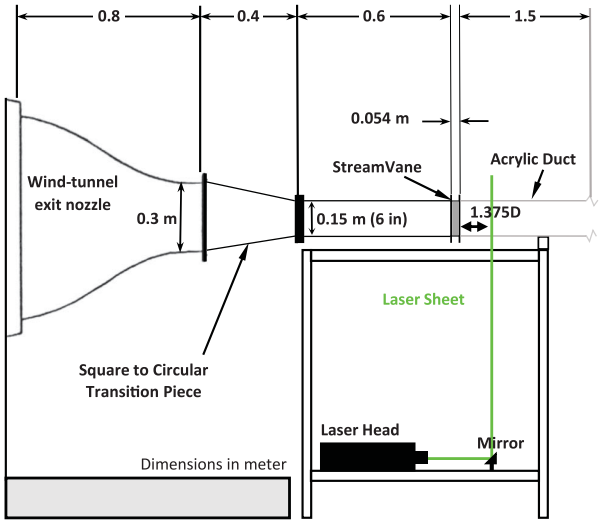

Fig. 3 Small-scale experimental setup for testing and validating StreamVane designs with PIV (adapted from Sanders et al. [21]).

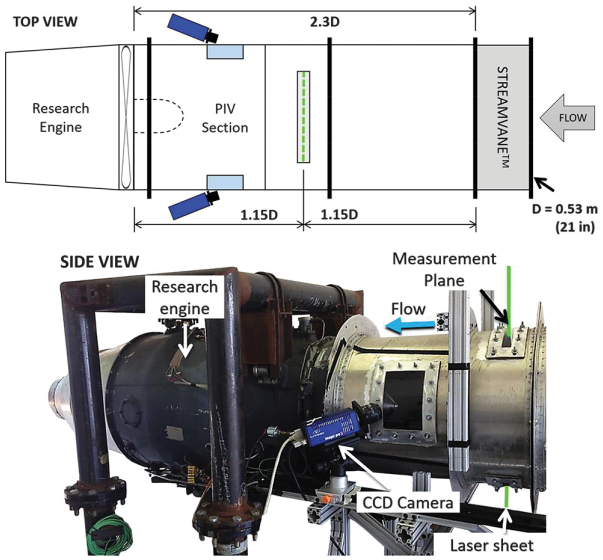

Fig. 4 Stereoscopic PIV schematic from top and side views, and details of the instrumentation used in the engine.

C. Engine Research Rig and Engine PIV

The full-scale engine research rig, located at the Virginia Polytechnic Institute and State University Turbomachinery and Propulsion Research Laboratory, was composed of tunnel sections and a bellmouth for inlet flow conditioning, two particle seeding distribution devices, the StreamVane, a test section with optical access for cameras and the laser sheet, connection tunnel sections, and the Pratt and Whitney Canada JT15D-1 research engine mounted to a test stand, as pictured in Fig. 4. Each tunnel section was one duct diameter long and was constructed using 20 gauge aluminum sheet metal, rolled to a 21 in. inner diameter circle and riveted together with circular flanges for bolting sections together. Axial average bulk velocity for this setup was 65.1 m/s (50% corrected fan speed, 213.6 ft/s, Mach 0.18), yielding a duct Reynolds number $Re_D = uD/\nu$, of 1.9 million, based on a duct diameter of 0.53 m (21 in.) and kinematic viscosity ν at 325 K of 1.80×10^{-5} m^2/s. Detailed properties of the turbofan engine settings are presented in Table 3 [22].

In past work [18,19], the authors have presented details of a new method for PIV measurements in uniform and distorted inflows in the research engine inlet. The methods employed for the results analyzed in this article represent several practical advances in applying PIV in the harsh environment of the engine.

The optical tunnel section for PIV contained four windows: two for camera access and two for laser entry and dump. For the camera windows, optically clear 3-mm-thick cast acrylic with antireflective coating was compressed between layers of sheet metal and bolted in place using nut plates. The laser entered the inlet through an acrylic window by the label "laser sheet" shown in the lower right of Fig. 4. An acrylic window shown at the top right of Fig. 4 by the "measurement plane" label allowed the laser to exit the inlet to minimize reflections that would degrade the PIV image quality. A cavity with a depth of approximately 5 mm (0.2 in.) was present at each window–wall interface, resulting in local secondary flow as the flow recirculates near the edges of the window. The interior of the test rig was spray painted flat black, cameras and windows were covered with a black cloth during testing to reduce glare and laser reflection on the windows and tunnel walls, and testing was performed in the open cell after sunset to minimize light saturation in the second time exposure of image pairs.

The flow entering the bellmouth was seeded by two oil atomizers and two blowers. The atomizer is a pressure vessel that comprises an array of 12 Laskin nozzles, six of which were used for atomizing DEHS oil, yielding particles with 1 μm diameter, in average. A second seeder has four Laskin nozzles that also atomized DEHS oil and covered a separate region of the inlet flow than the first seeder. Several configurations were tested to determine appropriate positions for the seeders and the blowers such that the seeding was relatively uniform. A detailed investigation of the seeding methods in this facility has been presented by Nelson [18].

The PIV equipment was mounted around the test section on an aluminum structure and metal rails. An articulated laser beam delivery arm was used to position the laser sheet at the lower laser window facing up, so that the laser sheet would exit the test section through the top window. The laser sheet was formed using a −20 mm focal length cylindrical lens to expand the width of the sheet and a +500 mm spherical lens to focus the thickness of the sheet to 1–2 mm at the center of the measurement volume. The same cameras as the small-scale test

Table 1 Summary of small-scale and engine experiment laser and lenses properties

	Laser properties			Lens properties	
Experiment	Rated power, mJ/pulse	Thickness of sheet, mm	Width of sheet, m	Focal length, mm	Aperture (f-stop)
Small scale	120	5	0.15	24	4.0
Engine	200	1–2	0.45	50	2.8

Table 2 Summary of small-scale and engine experiment properties

Experiment	Duct diameter, D	Velocity, m/s	Reynolds number	Mach number	Distance to measurement plane
Small scale	0.15 m (6 in.)	50	0.5×10^6	0.14	1.375D
Engine	0.53 m (21 in.)	65.1	1.9×10^6	0.18	1.15D

Table 3 Turbofan engine settings for full-scale engine experiment [22]

Turbofan engine settings	
Corrected fan speed (% maximum of 16,000 rpm)	65% maximum (≈10,400 rpm)
Fan blade tip speed	290 m/s (≈0.85 Mach)
Corrected inlet mass flow rate	20.5 kg/s (nominal)
Fan pressure ratio	1.27 (nominal)

were used, this time equipped with 24 mm Nikon lenses, facing upstream at oblique angles of approximately 37 deg relative to the test rig centerline and 95 deg to the laser sheet plane. Scheimpflug lens adapters were used for correcting the focus of the cameras at the measurement plane.

Because the measurement plane determined by the laser sheet was not wide enough to cover the entire diameter of the engine inlet, a measurement volume was determined and data were acquired in a 45 deg sector, as shown in Fig. 5. In postprocessing, these slices of flow measurements were stitched together to obtain the velocity statistics of the entire flow cross section. The StreamVane distortion device was rotated counterclockwise by 22.5 deg increments to obtain the full cross-sectional profile with a 50% spatial overlap between successive data sets. Five hundred images were taken with 9 μs delays in the laser double-pulse for each measurement position. Given the overlap, 1000 flow measurements were available in each flow position for velocity statistics.

The PIV images were processed using stereo cross-correlation in DaVis 8 with no background subtraction or image preprocessing. Multipass processing was used. The first pass consisted of a round window of 64×64 pixels with a 50% overlap. Then, a round window of 32×32 pixels with a 50% overlap was used for the two following passes. The vectors with a peak ratio (the ratio of the largest correlation peak to second largest peak in an interrogation window) less than 1.3 were deleted. A built-in median filter analyzed individual vectors and their eight neighboring vectors for spurious vectors and, after excluding invalid data, calculated the average and standard deviation of the neighbors for reference. Vectors that did not fall within an interval of the average ± 2 times the standard deviation were removed. For this optical configuration, one pixel unit in image space was equivalent to 0.15 mm (0.00591 in.) in flow space. For the final pass of the multipass processing, the spatial resolution of each interrogation window was 4.8 mm (0.19 in.).

D. Flow Statistical Postprocessing

The raw results obtained using PIV were analyzed statistically. The single-point mean velocities $\bar{u}_r, \bar{u}_\theta, \bar{u}_z$ were used to obtain turbulent velocity fluctuations

$$u_i' = u_i - \bar{u}_i \qquad i = r, \theta, z \tag{1}$$

and the six-component Reynolds stress tensor was computed from the covariance of the velocity fluctuations $\overline{u_i' u_j'}$. The method for aggregating single-point results from the overlapped sets of PIV data is described further as follows.

The stitching algorithm used for combining all the data sets and obtaining the complete flow profiles was fashioned after "binning" methods, such as the slot correlation method used for time-domain processing of irregularly sampled laser Doppler velocimetry data [23]. A 120 bin duct plane radial grid (shown in red in Fig. 6) was specified to best mesh with the cylindrical geometry of the engine inlet duct. The black mesh (Fig. 6b) represents the locus of raw PIV results. The methods used to bin the oversampled PIV data into the grid for duct planar statistics is described next.

In the algorithm, each valid velocity vector measurement obtained from every image of the PIV results was compared in position to the positions of the grid points (Fig. 6b, bottom). Once the nearest radial grid point (depicted in red) was identified, the velocity sample was added to the bin, and bin ensembles were compiled by looping through all measurements. The highlighted area in the bottom right frame in Fig. 6 shows an example of a bin (red) and the raw PIV data points (black) around it that would be added to it. The method has benefits and some important effects on the measurements. The quality of the statistics gained from this method could be dramatically improved due to simple standard error of the mean considerations of averaging more data for each point [24]. Further, by binning velocity results that were obtained at multiple locations from multiple planes, systematic uncertainties are reduced due to the independence of these measurements with one another. During postprocessing, the histograms for these points were probed as a check for differences between the overlapping sets. The consistency of the results from multiple measurements provided another validation of the results. Finally, the approach represents a logical method for using overlapping data sets, which maximizes the amount of measurement information used to obtain statistics.

The mean velocity, gradients, and Reynolds stress statistics presented in the Results section were filtered on the binned radial grid using a 3×3 median filter. This filter was expected to remove spurious noise in the statistics fields, while minimizing the spatial smoothing effect that low-pass linear filters cause [25].

E. Experimental Uncertainty

PIV uncertainty is affected by shear, displacement, seeding density, particle diameter, system calibration, timing errors, and the optical setup, as well as other systematic and random sources [26]. Uncertainties estimated from a repeatability study and from propagation of errors analyses are described further. Uncertainty values for velocity and swirl angle measurements are shown in Table 4.

Measurement repeatability over multiple engine runs was assessed as a representative in situ estimate for uncertainty. The obtained uncertainty was calculated at 95% confidence by applying a Student's t distribution to three data sets acquired in the aerodynamic interface plane measurement configuration. As previously described for this configuration, the measurements were taken in 45 deg sections, and the screen was manually rotated, requiring engine shutdown and therefore yielding independent data sets. The repeatability was calculated by finding the standard deviation σ for the three data sets at each point in the measurement plane, multiplying this value by the appropriate Student's t distribution value 4.303 (two degrees of freedom, 95% confidence), and then normalizing on the average profile velocity. As shown by Nelson [18], the regions of high-quality data exhibit uncertainty values of 5% of the mean velocity magnitude or less. At the edges of the measurement plane where laser intensity and seeding concentrations are both reduced, uncertainties are greater.

To estimate an uncertainty in the velocity that would not necessarily be detected by the repeatability study, the fundamental PIV calculation of velocity was considered

$$V_p = \frac{\Delta x_p}{\Delta t}, \qquad \text{where } \delta(V_p) = \frac{\partial(\Delta x_p)}{\Delta t} \tag{2}$$

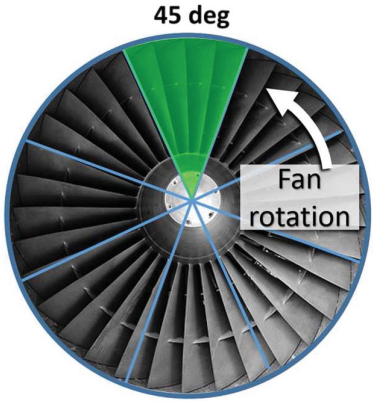

Fig. 5 Highlighted measurement slice and fan rotation direction. Data are presented in the FLA orientation, where positive azimuthal velocity is corotating with the fan, and positive radial velocity is outward.

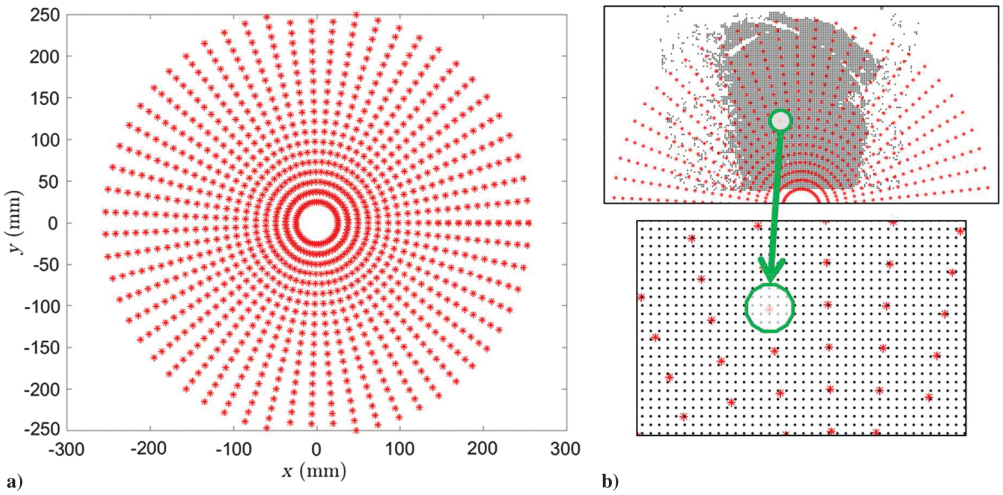

Fig. 6 Representation of a) 120 bin ring-style grid used for binned statistics and b) zoomed region of one bin.

where Δx_p is the displacement of particles and Δt is the time delay between double-pulsed PIV images. Typical correlation peak interpolation can achieve resolution of 0.1 pixels for a majority of real data under ideal conditions [26,27].

Based on the scale factor calculated by the software calibration, the displacement uncertainty was determined to be 0.016 mm. Assuming no uncertainty in the time delay, the velocity uncertainty was calculated to be 1.68 m/s, or ±2.41% of the average profile velocity magnitude for these data, of the same order as the repeatability uncertainty. The swirl angle uncertainty can be derived from its definition $\theta = \tan^{-1}(u_\theta/u_z)$, resulting in an uncertainty of $\sqrt{2}$ times the velocity uncertainty for small angles, or ±3.4%.

III. Results and Discussion

The PIV results obtained were analyzed to assess two main questions: the scaling of the StreamVane swirl results from small-scale tests to the full-scale engine inlet, and the higher-order effects of the StreamVane to the flow, including signatures of vane wakes and introduced turbulent stresses. A brief analysis of the effects of the distorted flow on the research engine fan blades was also performed. A small-scale StreamVane was tested in the wind tunnel described previously, followed by a full-scale StreamVane test in the research engine rig to generate the flow to be studied using particle image velocimetry. The outer ring of the contour plots in this section represents the diameter of the inlet duct, and the gap between the ring and the plot, both in small and full scale, is the region where data could not be collected due to laser glare.

The results obtained with this multiscale experiment allow for scaling comparisons between the swirl profiles, as well as insights into the impact that vane-generated turbulence has on the flow distortion in the duct. Because this swirl distortion methodology is to be used for assessing fan aerodynamics impacts, the details of the flowfield produced are critical for properly interpreting the aerodynamics data. A normality test was performed on the full-scale engine data. The results presented in Fig. 7 and Table 5 show that the axial and radial velocity components are both negatively skewed but approximately normal over 90% of the probability range, whereas the azimuthal velocity component, the one that is directly related to the swirl angle, is normal within uncertainties, exhibiting skewness of 0.16 and kurtosis of 3.20 (the normal distribution values are 0 and 3 for skewness and kurtosis, respectively).

Table 4 Estimate of uncertainties of statistics derived from PIV measurements [18]

Quantity	Uncertainty from repeatability study, %	Uncertainty in calculated results, %
Velocity	~5	±2.4
Swirl angle	~7	±3.4

The primary dynamic scaling parameters governing this device are the Reynolds and Mach numbers of the approach flow in the inlet duct. As will be discussed further, direct geometric scaling applies to the secondary flow due to the dominance of vortex dynamics in the flow physics. A factor of 4 variation in the Reynolds number was achieved across the small- and full-scale experiments. However, the Mach number for both experiments are quite similar: 0.14 at the small scale and 0.18 at the full scale. In this way, the experiment has been optimized to test Reynolds number scaling in the incompressible regime, independent of Mach number. More care needs to be taken when analyzing the flow over the vanes of the StreamVane, because the interaction of vanes will decrease the critical Mach number, as previously observed for cascades of vanes. For instance, the experimental results from Perdichizzi [28] indicate that flow properties in cascades are particularly influenced once the critical Mach number has been reached, but much less so prior. Indeed, Sanders et al. [21] have previously shown empirical evidence of Mach number independence of StreamVane performance in the compressible subsonic regime, whereas analysis may be used to further explain these observations.

Consider the classical wavy-wall problem [29] as a basic analog for the behavior of the streamlines downstream of the StreamVane. A streamline is specified to follow a sinusoidal path with amplitude h and wavelength l with $h \ll 1$, and the velocity field is computed along the streamline using small perturbation assumptions and invoking irrotational flow such that a velocity potential exists. For this analysis, z will be considered the axial direction, whereas y (and therefore u_y) will be the secondary direction. Flow angle α for this problem is defined as $\alpha = \tan^{-1}[u'_y/(V_\infty + u'_z)]$, where u'_y are the velocity fluctuations in the flow. Using the small perturbation and irrotational assumptions, a perturbation velocity potential may be obtained from which the secondary velocity perturbation is determined throughout the sinusoidal path of the streamline:

$$\phi(x,y) = \frac{V_\infty h}{\sqrt{1-M_\infty^2}} \exp\left(-\frac{2\pi\sqrt{1-M_\infty^2}\,y}{l}\right) \sin\left(\frac{2\pi x}{l}\right) \tag{3}$$

$$u'_y = \frac{\partial\phi}{\partial y} = -\frac{2\pi V_\infty h}{l} \exp\left(-\frac{2\pi\sqrt{1-M_\infty^2}\,y}{l}\right) \sin\left(\frac{2\pi x}{l}\right) \tag{4}$$

To evaluate the flow angles, we take into account a small angle approximation, $\tan\alpha = \alpha$, and so the flow angles are simply $\alpha = u'_y/(V_\infty + u'_z)$. We also know that $V_\infty \gg u'_z$, so that is

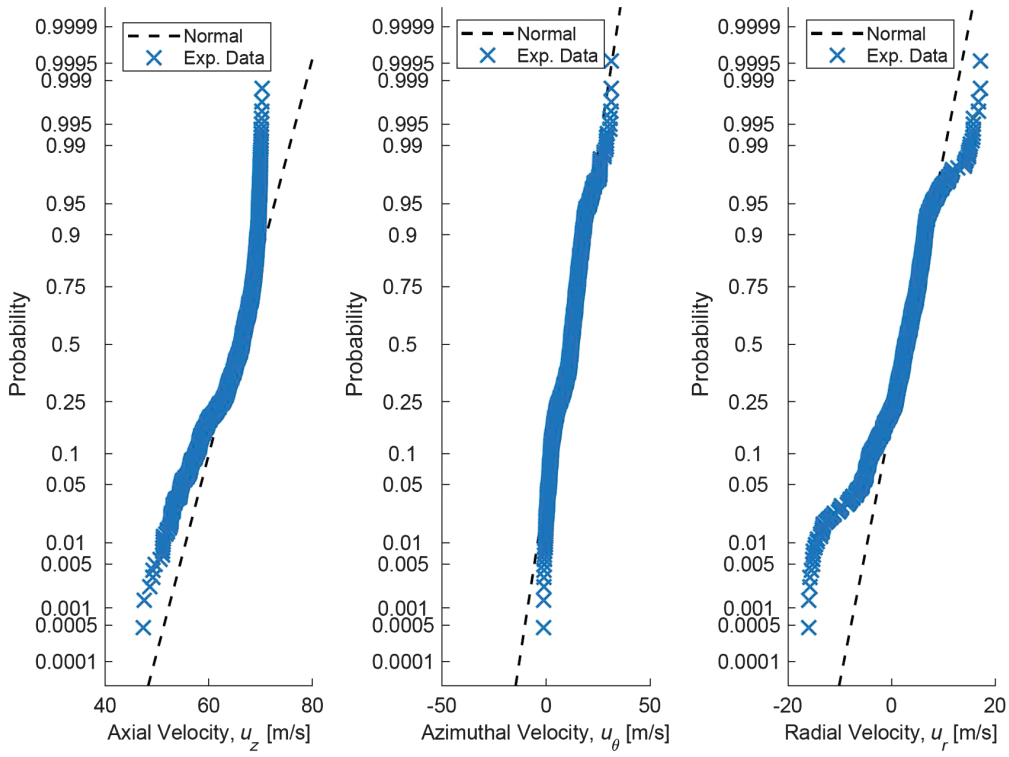

Fig. 7 Probability distribution of full-scale experiment velocity components. Dashed line represents a normal distribution.

simplified even further, to $\alpha = u_y'/V_\infty$. With that and considering only the greatest value of the flow angle where $\sin(2\pi r \cos\theta/l) = 1$ and on the streamline of interest at $y = 0$,

$$\alpha = \frac{u_y'}{V_\infty} = \frac{2\pi h}{l} \tag{5}$$

Equation (5) indicates that flow angle in the wavy-wall example is Mach number independent, a finding that serves as a first-order approximation to the secondary flow behavior for the streamlines downstream of the StreamVane. It is appropriate to comment briefly upon the assumptions of this analysis to assess the applicability to the current problem. The most restrictive is perhaps that of irrotationality. In the reference plane containing the streamwise approach velocity vector and the vane chord, the only regions of intense rotational mean flow are the vane wakes and the cores of vortices. In all but the cores of tightly wound vortices, both the wakes and the streamwise vorticity due to azimuthal variations in the vane angles are higher-order effects. In the limits of slowly varying velocity components in the out-of-plane direction and high Reynolds number wakes, the analysis is thought to capture the dominant effects of pressure-driven flows due to the vanes. The other assumption is that of small perturbation linearization around the approach Mach number M_∞. As is well known for transonic flow, this approximation is robust for subsonic Mach numbers up until some region of the flow is locally supersonic (i.e., up to the critical Mach number). In the limit of subsonic flow over the vanes, the linearized flow assumption will produce only small truncation errors due to nonlinear potential flow effects. This analysis corroborates previous findings that the swirl angle generated by the StreamVane is insensitive to Mach number [3,21].

Table 5 Statistical properties of the velocity data presented[a]

	Skewness	Kurtosis
Normal distribution	0	3
u_z	−1.13	3.56
u_θ	0.16	3.20
u_r	−0.81	5.79

[a]For a normal distribution, skewness is zero and kurtosis is three [20].

For the small-scale experiment, Re_D was 0.5 million, and for the full-scale experiment, it was 1.9 million (i.e., the engine duct Reynolds number was four times greater than the small-scale one). Physically, it was thought that this difference would be most affected by the blade boundary-layer displacement thickness scaling as a ratio of blade spacing, because this ratio would decrease with increasing scale. As such, the low Reynolds number would have a slightly higher effective solidity (ratio of the blade chords to the vane-to-vane spacing) and higher effective blockage, and thus higher losses, assuming turbulent flow over the vanes. At very low Reynolds numbers where laminar flow may exist over much of the vane chords, such scaling arguments may break down due to boundary-layer separations on the vanes. Owing to the presumed dominance of inviscid vortex dynamics on secondary flow generation, it was also hypothesized that the secondary flow away from the duct wall would have little impact from scaling (i.e., secondary flow angles would be consistent across Reynolds numbers).

From the small- and full-scale experiment plots presented in Fig. 8 [30], it is possible to see that the main characteristics of the flow agreed well in both experiments: The counterclockwise (corotating, in the same direction as the fan) bulk swirl is centered in the middle of the flow and there is a clockwise (counter-rotating, in the opposite direction of the fan) tightly wound vortex on the left half of the plot. The center regions of the in-plane velocity plots show different velocity profiles between the small-scale experiment, where flow was almost entirely azimuthal, to the full-scale plot, which also showed radial velocity. However, the velocity magnitudes in this region, represented by the colored contour plot in the background, were extremely small, between zero and 0.05 times the normalized velocity for each case, making this difference negligible.

For quantitative comparison of the generated swirl in both experiments, plots of the swirl angle of the flow at constant radii are presented in Fig. 9. The experimental results agree between the small

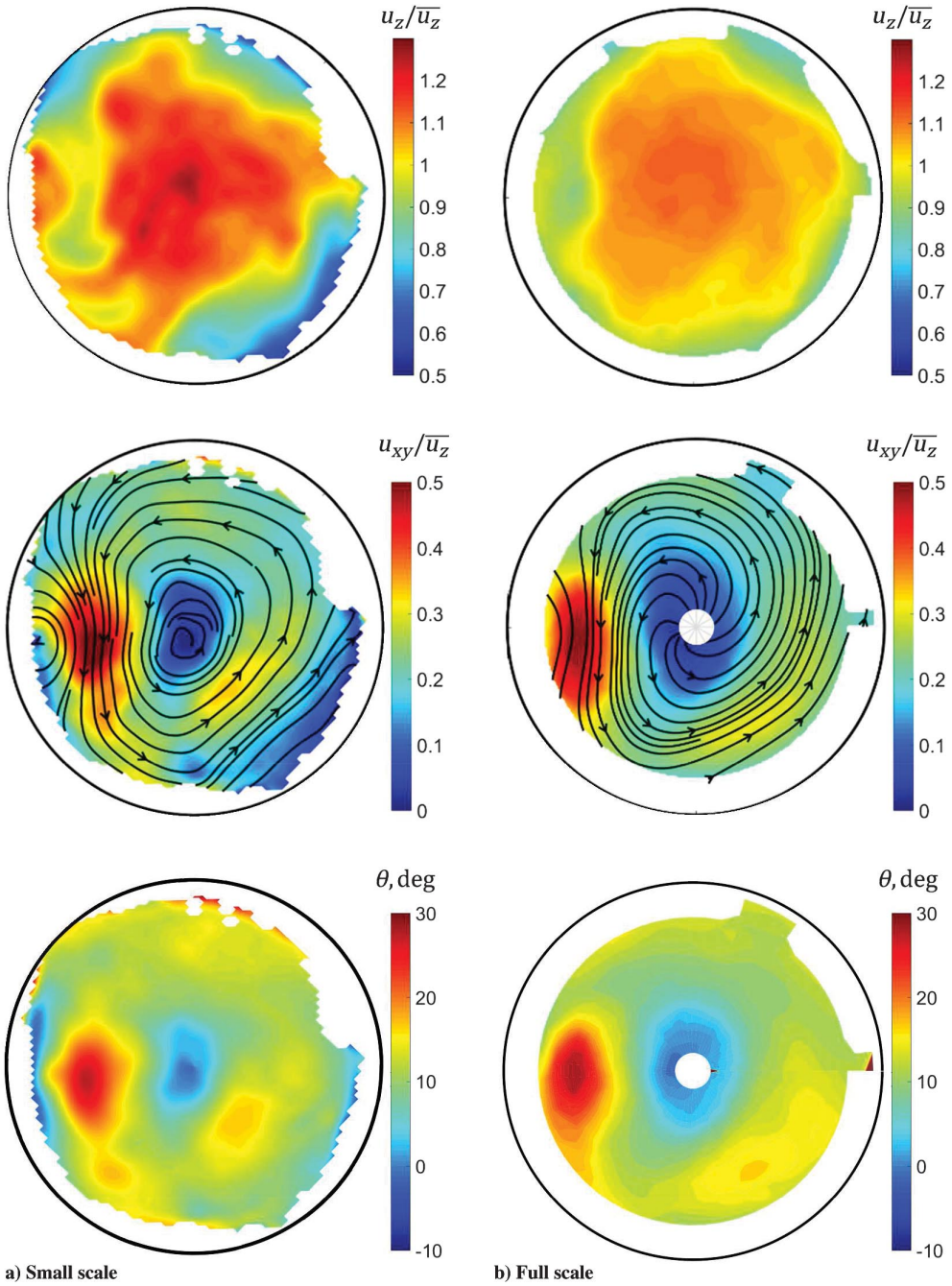

a) Small scale **b) Full scale**

Fig. 8 Side-by-side comparison of the normalized mean velocity components for a) small-scale and b) full-scale engine experiments [30].

and full scale over a large portion of the profile, indicating success in scaling the profile. The rms difference in swirl angle between cases is listed in Table 6. All constant-radii profiles for small and full scale exhibited an rms difference of less than 3 deg.

A key question for the current work was, in what ways does the StreamVane method affect the diffusive properties of the profile that is generated? Specifically, it must be the case that both mean flow and turbulence length scales would contain memory of the vanes with characteristic length scales of the chord lengths and vane-to-vane spacing. Although it is not immediately evident from the full-scale result plots in Fig. 8 that such features were present, a set of deeper analyses were performed to determine the characteristics of this StreamVane. For this, the full-scale experiment velocity gradients are presented alongside gradients of the CFD simulated flow used as the guide for the design and creation of the HWB StreamVane, where no vanes were present. Note that, although this analysis was done for a specific StreamVane geometry, which was very complex, combining a bulk swirl and a tightly wound vortex, this has also been applied to a simpler profile consisting of only a tightly wound vortex distortion, and the results have shown good agreement between design and experiments, proving that this technology is extremely important in the analysis of distorted inflows [31,32].

To better illustrate the details of the mean flowfield, particularly as it pertains to flow memory of the turning vanes, the velocity gradient fields computed in the radial and azimuthal directions were analyzed for the streamwise (Fig. 10), radial (Fig. 11), and azimuthal (Fig. 12) components of the mean velocity. It is evident from the patterns in the gradients that the vane wakes, and especially the wakes from the

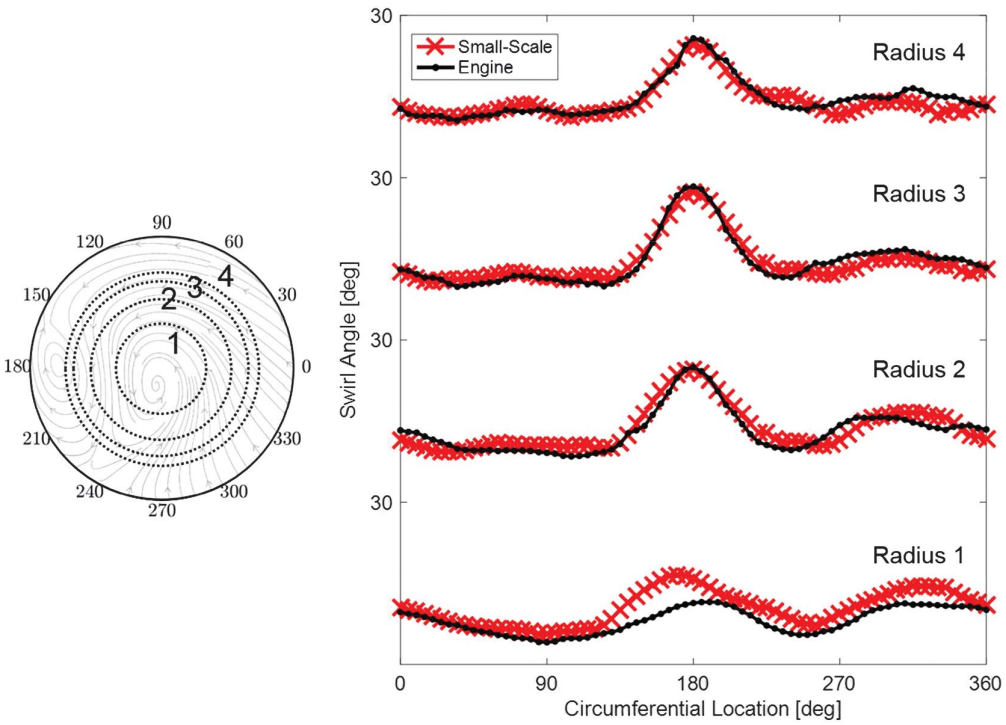

Fig. 9 Comparison of small-scale and full-scale engine experimental results at 1) $r/R = 0.36$, 2) 0.55, 3) 0.67, and 4) 0.73.

structural support vanes, had a significant influence in this flow (see Fig. 10). The gradients in the streamwise velocity may be readily interpreted in terms of shear flow mechanics. These wakes generated turbulent shear stresses that would promote diffusion in the direction normal to the gradients. Classical scaling arguments [33] indicate that turbulence length scales for these features could be expected to be on the order of the feature width, as will be shown later in the results. As these small-scale features were not present in the desired input flow, these details are unique to the StreamVane-generated flowfield.

The velocity gradients of the radial and azimuthal velocities presented in Figs. 11 and 12 contain the same general, large-scale features of the gradients of the CFD design profile. Several features at smaller scales, however, were introduced by the discrete vanes. Despite these small-scale features, the streamwise vorticity presented in Fig. 13 indicates that the magnitude of the rotation of the overall flow was dominated by the large-scale attributes of the desired swirl profile, rather than the details of the vane distribution of the swirl device. The small-scale artifacts, then, could be expected to produce increased turbulence and turbulent diffusion around these areas, promoting mixing of the vane wakes.

The turbulence produced by the StreamVane device has several implications for its application as a flowfield simulator. The flowfields that produce distortion in situ are likely accompanied by turbulence length scales and intensities that scale with the features that led to the distortion. As an example, the hybrid wing body flow considered here has distortions due to leading-edge vortex roll up in an extreme flight condition. In such a case, the turbulence field should be associated with the free shear turbulence of the vortex [34]. Ground vortex applications are thought to be similar, although the suction-induced stretching in this case may limit turbulence in the ground vortex [35,36]. In the case of the StreamVane, we can hypothesize that turbulence behavior could develop, which scales on the large-scale flow distortion features due to free shear flow instabilities. However, the development of these features would take time and distance downstream of the StreamVane, and also, the turbulence immediately produced by the vanes due to their turbulent wakes would be of much smaller scales (in length and time) than the large-scale feature turbulence. Thus, it is reasonable to predict that the flowfield development histories of the installed engine versus the StreamVane research rig could produce different integral scale turbulence characteristics. The net leading-order effect of these phenomena is thought to be a difference in the large-scale turbulent diffusion rates of the flows.

Table 6 Root mean square difference in swirl angle between small-scale and engine experimental results

r/R	rms difference engine and small-scale, deg
0.36	1.5
0.55	2.8
0.67	1.3
0.73	1.3

The Reynolds normal stresses, contributors to turbulent kinetic energy, are plotted in Fig. 14. The unsteady flow that contributes to these correlations was made up of a variety of motions, which included long wavelength meandering of the mean flow, relatively inactive in the effects on the smaller length-scale chaotic turbulence structure. The region around the tightly wound vortex is where most of the turbulence occurred, and inspection of the instantaneous flowfields revealed that a large amount of this statistical contribution was due to the meandering vortex core. As such, this effect is more one of global unsteadiness, rather than local chaotic turbulence, even though some turbulence introduced by the distortion vanes is expected [37]. The near-wall region presented generally elevated turbulence levels, as well. This appeared to be due to interactions between the vane wakes and boundary layer of the tunnel, creating a very thick duct wall boundary layer.

In plane shear flows, such as two-dimensional wakes, jets, and boundary layers, only the shear terms for the axial/transverse shear make significant contributions to momentum transport. Specifically, in free shear flows, the physics of the effect can be conceptualized via the Boussinesq approximation for turbulent viscosity [33], indicating that shear turbulence plays a diffusive role that is directly correlated with the local velocity gradients, as given in Figs. 10–12. The correlation coefficients

$$\rho_{ij} = \overline{u_i' u_j'} / \sqrt{(\overline{u_i' u_i'})(\overline{u_j' u_j'})}, \qquad i \neq j$$

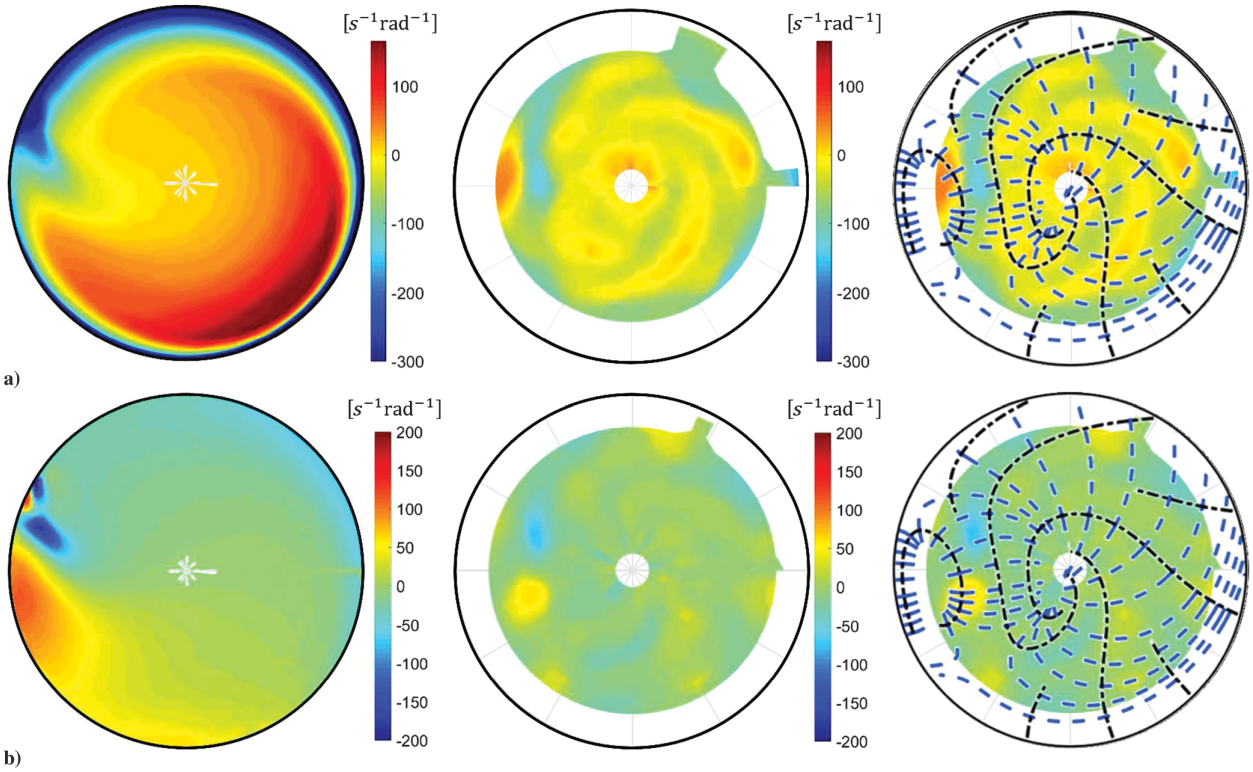

Fig. 10 Velocity gradients of streamwise velocity in a) radial and b) azimuthal directions for the (left) design profile and (center) engine data, superimposed by (right) the leading edge of the StreamVane vanes profile.

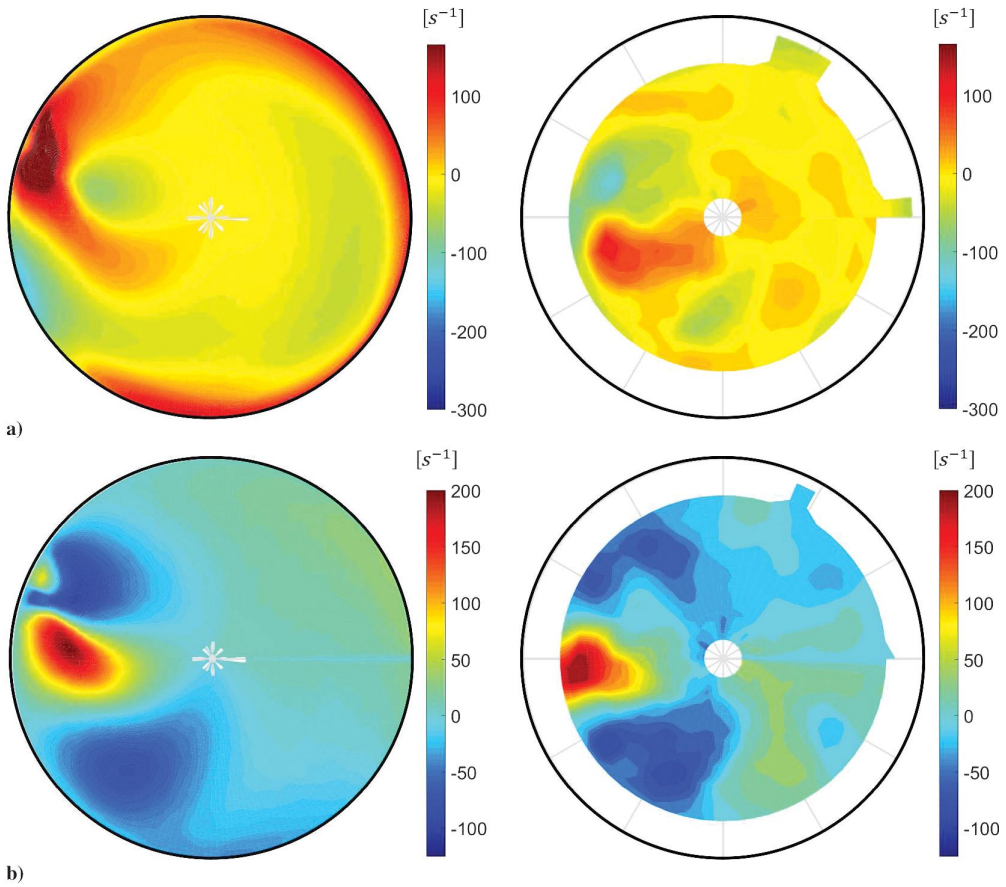

Fig. 11 Velocity gradients of radial velocity in radial and azimuthal directions for the (left) design profile and (right) engine inlet flow data: a) $\mathrm{d}u_r/\mathrm{d}r$, b) $(1/r)(\mathrm{d}u_r/\mathrm{d}\theta)$.

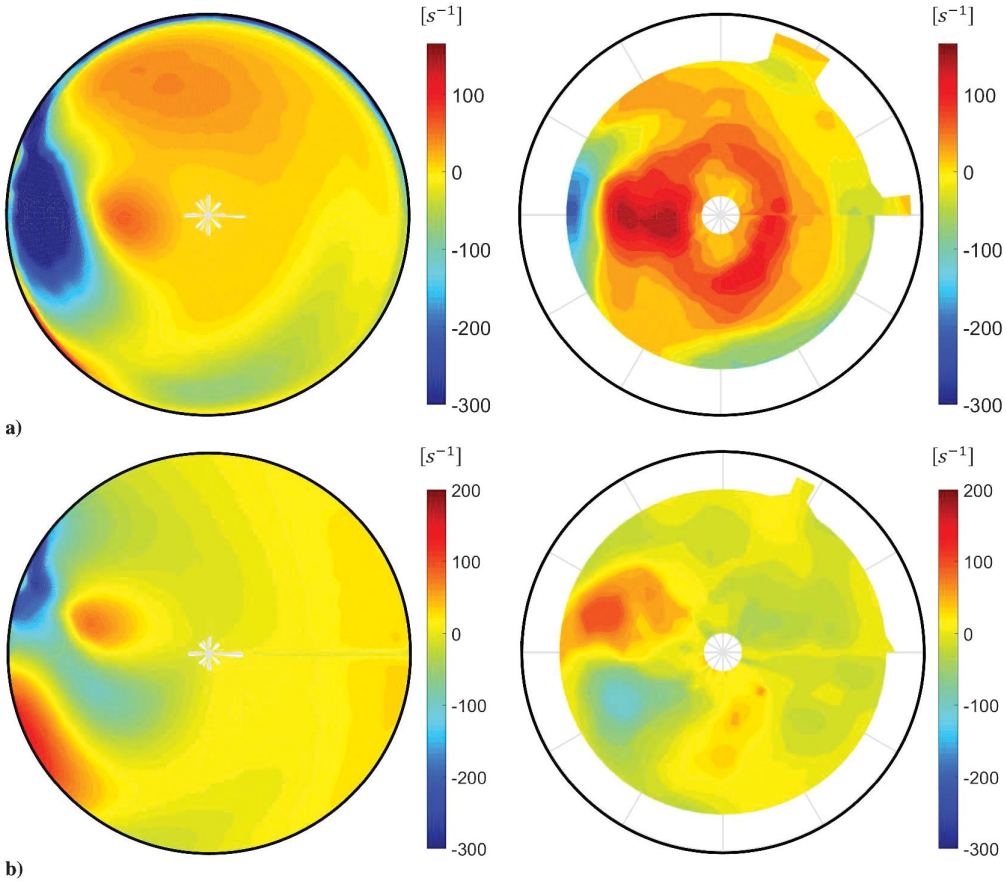

Fig. 12 Velocity gradients of azimuthal velocity in radial and azimuthal directions for the (left) design profile and (right) engine inlet flow data : a) $\mathrm{d}u_\theta/\mathrm{d}r$, b) $(1/r)(\mathrm{d}u_\theta/\mathrm{d}\theta)$.

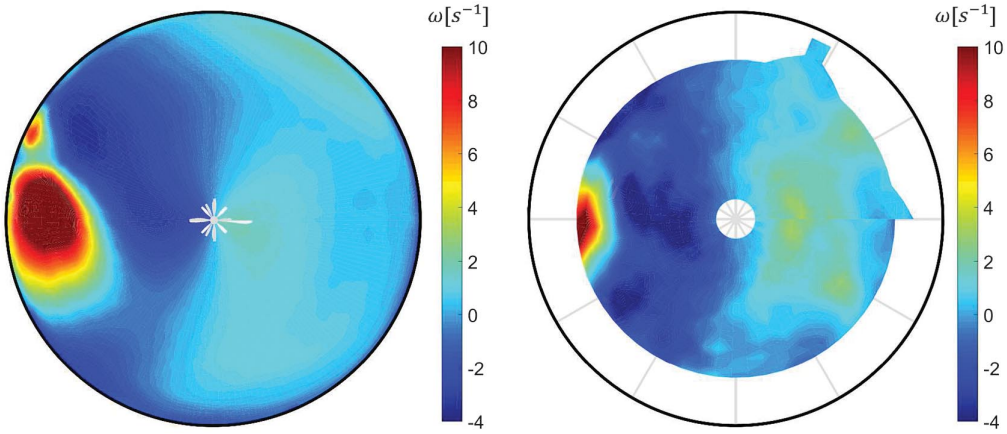

Fig. 13 Streamwise vorticity of the (left) design profile and (right) engine results.

(the tensor summing convention is not used), presented in Fig. 15, exhibit clear relationships with the structure of the gradients in the axial velocity (Fig. 10). In particular, $\rho_{\theta z}$ and ρ_{rz} exhibit the spiral nature of the gradients of axial velocity in the inner regions of the flow. Note, however, that these stress values are low in comparison to the stresses near the wall, because the normal stress turbulence values are quite low there (Fig. 14). In contrast, the ρ_{rz} behavior near the wall indicates high correlation and high normal stresses from this thick boundary-layer region. Further examination of the StreamVane method is required for minimizing the impact of wall/vane interactions and, further, in quantifying the impact of this wall flow turbulence on fan performance.

The simplified turbulent stress interpretation is not necessarily valid in the region of the tightly wound vortex. It is apparent that significant correlation coefficient values occur in both the $\rho_{r\theta}$ and ρ_{rz} components, accompanied with elevated values of each of the three Reynolds normal stresses in this region. The shear stresses in this region can be interpreted to indicate that an increased diffusion of this vortex will result, compared with a better-stabilized or less-turbulent vortex.

For further insight into the behavior of the turbulent eddies of the distorted flow, a two-point correlation analysis [38] was performed on the region of full-scale data highlighted in Fig. 16. The results are presented in Cartesian coordinates for ease of analysis, but it can be

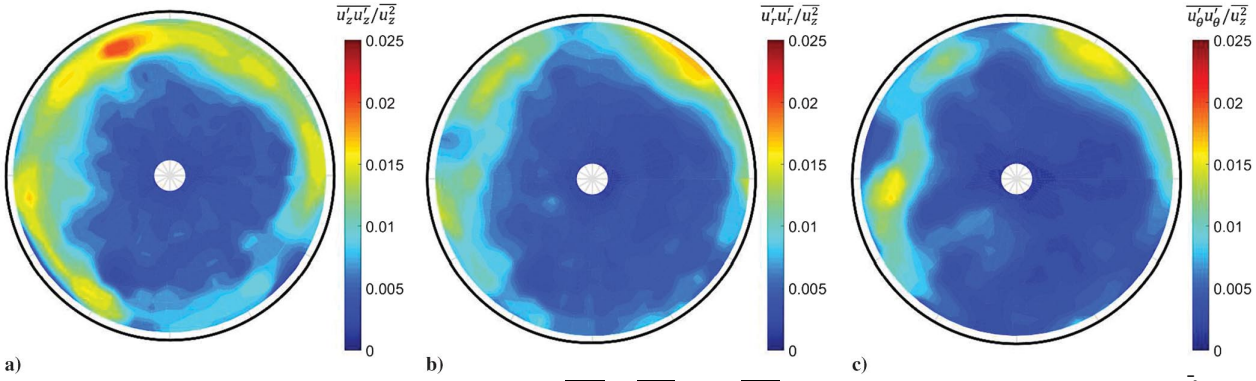

Fig. 14 Normal components of the Reynolds stress tensor a) $\overline{u_z'u_z'}$, b) $\overline{u_r'u_r'}$, and c) $\overline{u_\theta'u_\theta'}$, normalized by the axial average bulk velocity, $\bar{u}_z^2$.

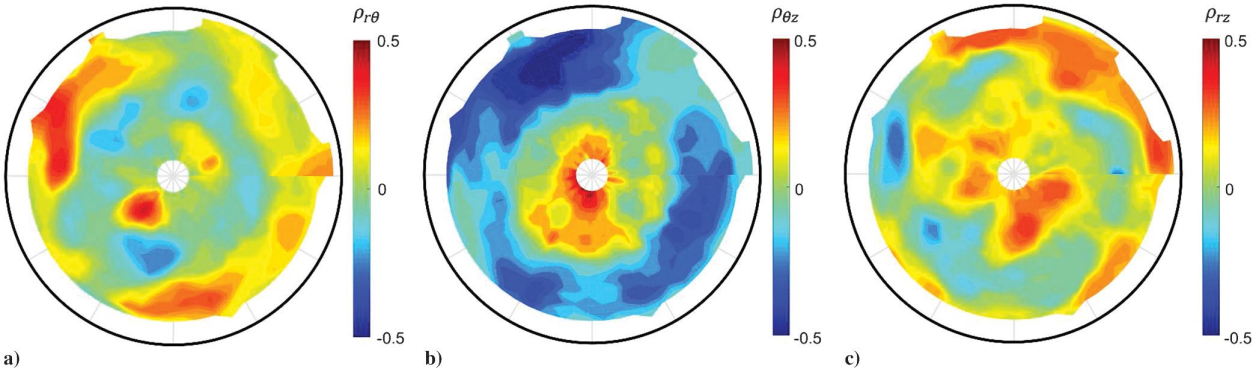

Fig. 15 Reynolds shear stress correlation coefficient between a) radial and azimuthal velocity $\rho_{r\theta}$, b) azimuthal and axial velocity $\rho_{\theta z}$, and c) radial and axial velocity ρ_{rz}.

considered that the horizontal scales are approximately the same as the azimuthal scales ($u_x \sim u_\theta$), and that the vertical scales are approximately as the radial scales ($u_y \sim u_r$). With the correlation map, it is possible to find the integral length scales of the flow, defined as

$$L_{\text{horizontal}} = \int_0^\infty f(r)\,\mathrm{d}r \quad \text{and } L_{\text{vertical}} = \int_0^\infty g(r)\,\mathrm{d}r$$

The turbulent length scales in the horizontal and vertical directions for each velocity component are presented in Table 7. As expected, due to presumed large-scale coherent motions of the vortex, the length scales around the region of the tightly wound vortex are larger than the region considered further away from the vortex. The single-vane wake region presents smaller length scales, representing smaller eddies, which are present due to the turbulent shear flow of the wake. It is noteworthy, in particular, that the length scales of the axial and radial velocity components are 3–5 times greater in the region of the vortex, indicating correlation of motions arising from flow features of greater extent than individual vane wake contributions. Indeed, the instantaneous velocity measurements indicated a meandering of the vortex core consistent with large-scale coherent motion of this feature. These results indicate that turbulence generation should be considered from both vane wakes and large-scale instability of the mean flow. In the former case, turbulent length scales are small (1/100 of the duct diameter), whereas length scales of the large-scale instability regions are most likely independent of the StreamVane design details and more indicative of the target flow replicated by the vanes.

The results presented beg further consideration of the implications present for the impact that StreamVane flows, and distorted inflows more generally, have on rotor performance and operability. From the mean flow produced alone, a number of past works guide a basic assessment of the effects on rotor aerodynamics. Fredrick and Davis observed changes in the fan pressure ratio and stall margin when subject to swirling flows in computational analyses [2]. For coswirling bulk flows, as presented in this work, an increase in the swirl angle caused a decrease in the fan pressure ratio and in the blade loading, ultimately resulting in an increase in fan stall margin (see [2] Fig. 14). The opposite was observed for counter-rotating swirl, decreasing the fan stall margin. As for the counter-rotating tightly wound vortex that was part of the profile studied in this work, the local loading of the blades will be increased in the region of the distortions and, despite being weakened, the vortex has been observed to pass the fan and remain intact as a discrete mean flow feature, as shown by Frohnapfel et al. [22]. As such, the aerodynamics of exit guide vanes and the fan duct are immediately affected by such inlet distortions.

Given the production of turbulence, it is necessary to consider how the presence and characteristics of the turbulence may locally affect the aerodynamics of the fan blades. Depending upon the turbulent intensity and length scales, the inlet turbulence may cause bypass transition of the blade boundary layer, as discussed specifically for turbomachinery by Walker [39]. Two possibilities exist for the turbulent field approaching the rotor: a distributed turbulence that is seen continuously by the rotor, and spatially compact wake turbulence in an otherwise nonturbulent field. The characteristics of the axial normal Reynolds stress in Fig. 14 indicate that the turbulence on the outer 25% of the annulus is significant in intensity around the entire duct circumference. In contrast, the regions closer to the center of the duct, where vane turning is less severe, exhibit lower turbulence levels, with patches indicative of vane wakes. It is likely that the particular mean flow profile chosen for replication has resulted in significant shear flow turbulence in the outer radial regions and could be presumed to affect the rotor by inducing early bypass transition. As described by Dong and Cumpsty [40], the turbulence due to individual vane wakes

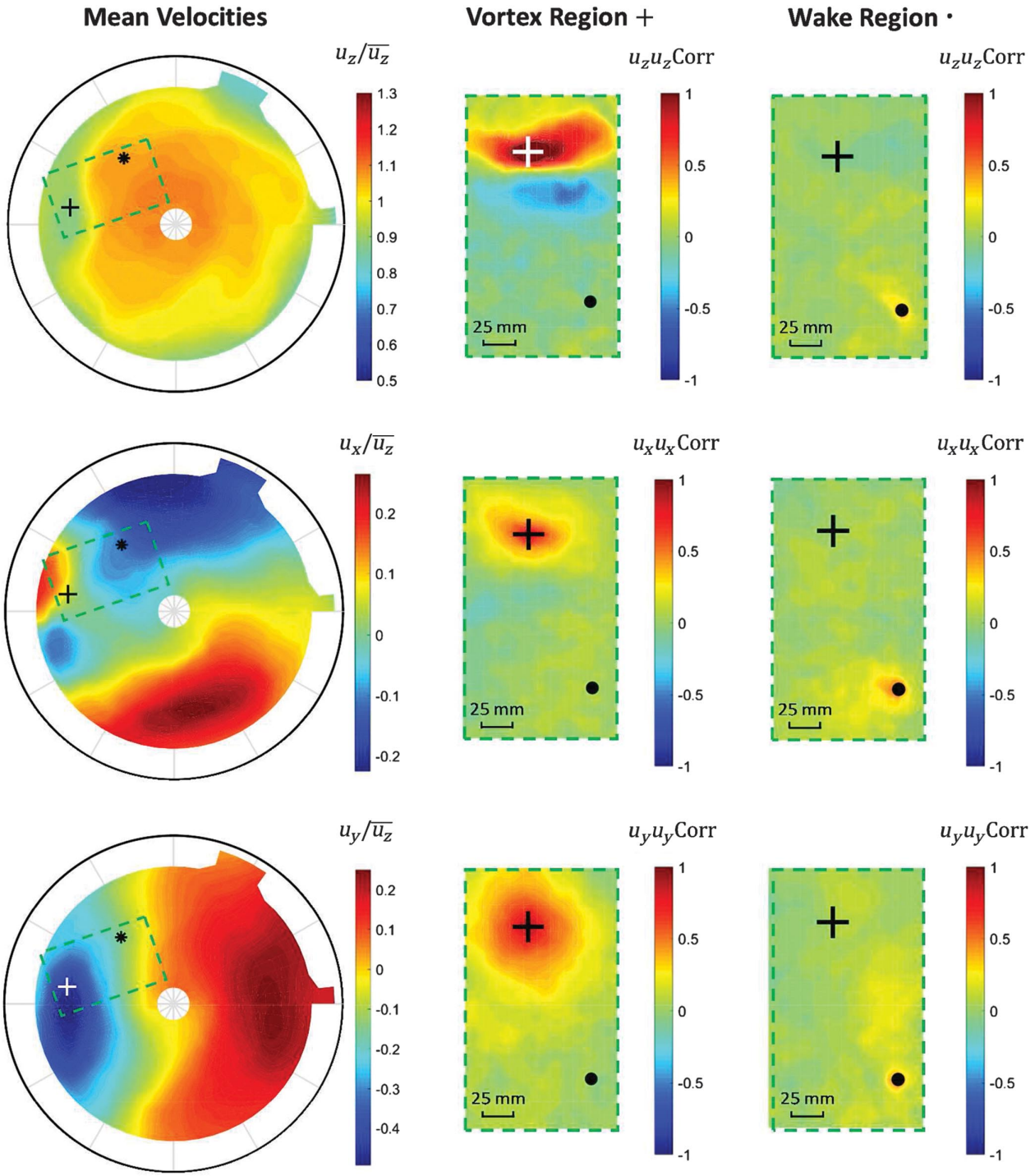

Fig. 16 Two-point correlation results for the region of data highlighted in the mean velocity component plots. The vortex region is indicated as the black/white plus sign, and the wake region is indicated as a black asterisk in the mean plots and as a black dot in the correlation plots for visualization purposes. Markers are shown in both correlation plots for reference.

can exhibit complex boundary-layer response, which may prolong the transition process due to the combined effects of the wake total pressure profile (which alters susceptibility to instability growth), and turbulent flow fluctuations, which perturb the profiles as the rotor passes between vane wakes. In many profiles generated by the StreamVane method, it is expected that this effect will dominate. Beyond the effects on blade boundary layers, chord-scale fluctuations must be considered, given the length scale of the turbulence in the vortex feature analyzed. In this region, the first-order effect is most likely a highly fluctuating loading (cycle-to-cycle loading fluctuations that are in addition to once-per-revolution fluctuations from mean flow distortion) that will correlate over several blade passages (e.g., Alexander et al. [41,42]). Depending upon the azimuthal velocity sense of the turbulent fluctuation, the intensity, and the scale of the eddy with respect to the rotor chord, these fluctuations could result in local separation.

Table 7 Integral length scales for the region around the vortex and a region away from the vortex, named wake region

Length scale	Vortex region		Wake region	
	Horizontal, mm	Vertical, mm	Horizontal, mm	Vertical, mm
u_z	28.0	19.3	4.7	6.3
$u_x(\sim u_\theta)$	14.7	9.8	13.2	7.6
$u_y(\sim u_r)$	22.5	29.9	5.8	9.7

IV. Conclusions

The StreamVane method was demonstrated for a complex swirl distortion profile consisting of a counter-rotating bulk swirl and a corotating tightly wound vortex, as that predicted for the inlet of a mounted engine on a hybrid wing body aircraft. A comparison of results for a small-scale experiment and for a full-scale device tested in a research turbofan engine validated the scaling between experiments. An analysis of Mach number independence for the flows indicate that, given small perturbations and irrotationality assumptions, the flow angle scaling downstream of the StreamVane is Mach number independent. These assumptions may produce small truncation errors due to nonlinear potential flow, whenever approaching the limit of subsonic flow over the vanes, and so one needs to take that into account for higher Mach number subsonic flows.

The particle image velocimetry measurements in the full-scale engine inlet provided the information needed for study of the details of the mean flow and turbulence produced by the StreamVane. The secondary mean flow has been shown to scale with duct size and approach flow velocity (thought to be independent of Reynolds number for sufficiently large Reynolds numbers) as expected, due to the presumed dominance of vortex dynamics in the secondary flow development. As may be expected, the presence of the vane wakes were most evident in the streamwise velocity gradients due to the edges of the wakes. In contrast, the streamwise vorticity was dominated by the desired secondary flow profile, with little apparent influence from the individual vane wakes.

The turbulent field seen by the rotor blades was also considered. The turbulent length scales of the flow in the vane wakes are on the order of 1/100 of the duct diameter, which is small when compared with length scales of the large-scale instability regions, where the vortex meandered around its mean core location. In the case of the present StreamVane profile, the turbulent field is more dependent on the distortion profile than the turbulent effects artificially added to the flow by the StreamVane. Given the turbulence characteristics, it was determined that the distortion profile analyzed, rather than the vane wakes, created significant shear flow turbulence in the outer radial regions of the flow. These features, which are thought to be similar to the features in the field being replicated, could be presumed to affect the rotor by introducing bypass transition. Further, the large-scale turbulent fluctuations detected for a tightly wound vortex feature in the profile will produce significant cycle-to-cycle variation in loading for individual rotor blades.

As work continues on this technology, exploration of flowfield details in different planes along the engine inlet will bring additional insight on distorted flow development. This will allow for conclusions to be taken on how the flow evolves and interacts with the duct, mainly exploring the role of turbulent diffusion and the stabilization of the vortex in the vicinity of the fan.

Acknowledgments

The authors would like to acknowledge National Institute of Aerospace (NIA) and NASA Langley Research Center for funding this work in association with NASA's Environmentally Responsible Aviation Project (NIA cooperative agreement RD-2917), project managers Fay Collier, Hamilton Fernandez, and Greg Gatlin from NASA Langley, and Bo Walkley (NIA). Additional thanks are extended to The Boeing Company (John Bonet and Ron Kawai), Pratt and Whitney (Wes Lord) for the industry perspective on swirl distortion, Mike Nelson for support, and Coordenação de Aperfeiçoamento de Pessoal de Nível Superior for financial support to Tamara Guimarães.

References

[1] Davis, M., Hale, A., and Beale, D., "An Argument for Enhancement of the Current Inlet Distortion Ground Test Practice for Aircraft Gas Turbine Engines," *Journal of Turbomachinery*, Vol. 124, No. 2, 2002, pp. 235–241. doi:10.1115/1.1451087

[2] Fredrick, N., and Davis, M., "Investigation of the Effects of Inlet Swirl on Compressor Performance and Operability Using a Modified Parallel Compressor Model," *Proceedings of ASME Turbo Expo 2011: Turbine Technical Conference and Exposition*, American Soc. of Mechanical Engineers Paper GT2011-45553, New York, 2011. doi:10.1115/GT2011-45553

[3] Pazur, W., and Fottner, L., "The Influence of Inlet Swirl Distortions on the Performance of a Jet Propulsion Two-Stage Axial Compressor," *Journal of Turbomachinery*, Vol. 113, No. 2, 1991, pp. 233–240. doi:10.1115/1.2929091

[4] Mitchell, G., "Effect of Inlet Ingestion of a Wing Tip Vortex on Compressor Face Flow and Turbojet Stall Margin," NASA TM X-3246, 1975.

[5] Nelson, S. L., "Performance of a 1.57-Pressure-Ratio Transonic Fan Stage with a Screen-Induced 90° Circumferential Inlet Flow Distortion," NASA TN D-8163, 1976.

[6] "A Methodology for Assessing Inlet Swirl Distortion," Soc. of Automotive Engineers Aerospace Information Rept. 5686, Warrendale, PA, 2010.

[7] Sheoran, Y., Bouldin, B., and Krishnan, P. M., "Advancements in the Design of an Adaptable Swirl Distortion Generator for Testing Gas Turbine Engines," *Proceedings of ASME Turbo Expo 2009: Power for Land, Sea and Air*, American Soc. of Mechanical Engineers Paper GT2009-59146, New York, 2009. doi:10.1115/GT2009-59416

[8] Genssler, H. P., Meyer, W., and Fottner, L., "Development of Intake Swirl Generators for Turbo Jet Engine Testing," *AGARD Propulsion and Energetics 68th (A) Specialists' Meeting*, AGARD CP-400, Munich, 1986.

[9] Fredrick, N., "Investigation of the Effects of Inlet Swirl on Compressor Performance and Operability Using a Modified Parallel Compressor Model," M.S. Thesis, Univ. of Tennessee, Knoxville, TN, 2010.

[10] Sheoran, Y., Bouldin, B., and Krishnan, P. M., "Compressor Performance and Operability in Swirl Distortion," *Journal of Turbomachinery*, Vol. 134, No. 4, July 2012, Paper 041008. doi:10.1115/1.4003657

[11] Anderson, B. H., and Gibbt, J., "Study on Vortex Generator Flow Control for the Management of Inlet Distortion," *Journal of Propulsion and Power*, Vol. 9, No. 3, 1993, pp. 422–430.

[12] Hoopes, K. M., "A New Method for Generating Swirl Inlet Distortion for Jet Engine Research," M.S. Thesis, Virginia Polytechnic Inst. and State Univ., Blacksburg, VA, 2013.

[13] Frohnapfel, D. J., O'Brien, W. F., and Lowe, K. T., "Fan Response to Inlet Swirl Distortions Produced by Boundary Layer Ingesting Aircraft Configurations," AIAA Paper 2015-3804, 2015. doi:10.2514/6.2015-3804

[14] Hobson, G. V., and Shreevet, R. P., "Inlet Turbulence Distortion and Viscous Flow Development in a Controlled-Diffusion Compressor Cascade at Very High Incidence," *Journal of Propulsion and Power*, Vol. 9, No. 3, 1993, pp. 397–404.

[15] Murphy, J. P., MacManus, D. G., and Sheaf, C. T., "Experimental Investigation of Intake Ground Vortices During Takeoff," *AIAA Journal*, Vol. 48, No. 3, 2010, pp. 688–701. doi:10.2514/1.45896

[16] Schröder, A., Geisler, R., Schanz, D., Agocs, J., Pallek, D., Scholl, M., Klinner, J., Beversdorff, M., Voges, M., and Willert, C., "Application of Image Based Measurement Techniques for the Investigation of Aeroengine Performance on a Commercial Aircraft in Ground Operation," *17th International Symposium on Applications of Laser Techniques to Fluid Mechanics*, Paper 242, 2014, pp. 7–10, http://ltces.dem.ist.utl.pt/lxlaser/lxlaser2014/finalworks2014/papers/02.4_3_242paper.pdf.

[17] Nelson, M. A., Lowe, K. T., O'Brien, W. F., Kirk, C., and Hoopes, K. M., "Stereoscopic PIV Measurements of Swirl Distortion on a Full-Scale Turbofan Engine Inlet," AIAA Paper 2014-0533, 2014. doi:10.2514/6.2014-0533

[18] Nelson, M. A., "Stereoscopic Particle Image Velocimetry Measurements of Swirl Distortion on a Full-Scale Turbofan Engine Inlet," M.S. Thesis, Virginia Polytechnic Inst. and State Univ., Blacksburg, VA, 2014.

[19] Guimarães, T. B., Lowe, K. T., Nelson, M., O'Brien, W. F., and Kirk, C., "Stereoscopic PIV Measurements in a Turbofan Engine Inlet with Tailored Swirl Distortion," AIAA Paper 2015-2866, 2015. doi:10.2514/6.2015-2866

[20] Gatlin, G., Vicroy, D., and Carter, M., "Experimental Investigation of the Low-Speed Aerodynamic Characteristics of a 5.8-Percent Scale Hybrid Wing Body Configuration," AIAA Paper 2012-2669, 2012. doi:10.2514/6.2012-2669

[21] Sanders, D. D., Nessler, C. A., Copenhaver, W. W., List, M. G., and Janczewski, T. J., "Computational and Experimental Evaluation of a Complex Inlet Swirl Pattern Generation System," AIAA Paper 2016-5008, 2016. doi:10.2514/6.2016-5008

[22] Frohnapfel, D. J., O'Brien, W. F., and Lowe, K. T., "Fan Rotor Flow Measurements in a Turbofan Engine Operating with Inlet Swirl Distortion," AIAA Paper 2017-1623, 2017. doi:10.2514/6.2017-1623

[23] Benedict, L. H., Nobach, H., and Tropea, C., "Estimation of Turbulent Velocity Spectra from Laser Doppler Data," *Measurement Science and Technology*, Vol. 11, No. 8, 2000, pp. 1089–1104. doi:10.1088/0957-0233/11/8/301

[24] Bendat, J. S., and Piersol, A. G., *Random Data: Analysis and Measurement Procedures*, Vol. 1, 1st ed., Wiley, Hoboken, NJ, 2011.

[25] Schrijer, F. F. J., and Scarano, F., "Effect of Predictor–Corrector Filtering on the Stability and Spatial Resolution of Iterative PIV Interrogation," *Experiments in Fluids*, Vol. 45, No. 5, 2008, pp. 927–941. doi:10.1007/s00348-008-0511-7

[26] Raffel, M., Willert, C., Wereley, S., and Kompenhans, J., "Physical and Technical Background," *Particle Image Velocimetry: A Practical Guide*, Vol. 1, 2nd ed., Springer–Verlag, Berlin, 2007.

[27] Nobach, H., and Bodenschatz, E., "Limitations of Accuracy in PIV Due to Individual Variations of Particle Image Intensities," *Experiments in Fluids*, Vol. 47, No. 1, 2009, pp. 27–38. doi:10.1007/s00348-009-0627-4

[28] Perdichizzi, A., "Mach Number Effects on Secondary Flow Development Downstream of a Turbine Cascade," *Journal of Turbomachinery*, Vol. 112, No. 4, 1990, pp. 262–268. doi:10.1115/1.2927705

[29] Anderson, J. D., *Modern Compressible Flow: With Historical Perspective*, 2nd ed., McGraw-Hill Education, Boston, 1990.

[30] Guimarães, T. B., Lowe, K. T., and O'Brien, W. F., "An Overview of Recent Results Using the StreamVane Method for Generating Tailored Swirl Distortion in Jet Engine Research," AIAA Paper 2016-0534, 2016. doi:10.2514/6.2016-0534

[31] Guimarães, T. B., Copenhaver, W. W., Schneck, W. C., Lowe, K. T., and O'Brien, W. F., "Swirling Flow Evolution Part 1: Design and Stereo PIV Measurements at Select Planes," AIAA Paper 2017-1620, 2017. doi:10.2514/6.2017-1620

[32] Schneck, W. C., Guimarães, T. B., Frohnapfel, D. J., Lowe, K. T., O'Brien, W. F., and Copenhaver, W. W., "Swirling Flow Evolution Part 2: StreamFlow 2D+t Model Validated with Stereo PIV Measurements," AIAA Paper 2017-1622, 2017. doi:10.2514/6.2017-1622

[33] Pope, S. B., "Mean-Flow Equations," *Turbulent Flows*, Vol. 1, 1st ed., Cambridge Univ. Press, Cambridge, England, U.K., 2000, pp. 93–95.

[34] Devenport, W. J., Rife, M. C., Liapis, S. I., and Follin, G. J., "The Structure and Development of a Wing-Tip Vortex," *Journal of Fluid Mechanics*, Vol. 312, April 1996, pp. 67–106. doi:10.1017/S0022112096001929

[35] Nolan, D. S., "The Stabilizing Effects of Axial Stretching on Turbulent Vortex Dynamics," *Physics of Fluids*, Vol. 13, No. 6, 2001, pp. 1724–1738. doi:10.1063/1.1370390

[36] Delbende, I., Rossi, M., and Le Dizès, S., "Stretching Effects on the Three-dimensional Stability of Vortices with Axial Flow," *Journal of Fluid Mechanics*, Vol. 454, March 2002, pp. 419–442. doi:10.1017/S0022112001007261

[37] Moore, J., Shaffer, D. M., and Moore, J. G., "Reynolds Stresses and Dissipation Mechanisms Downstream of a Turbine Cascade," *Journal of Turbomachinery*, Vol. 109, No. 2, 1987, pp. 258–267. doi:10.1115/1.3262096

[38] Pope, S. B., "The Scales of Turbulent Motion," *Turbulent Flows*, Vol. 1, 1st ed., Cambridge Univ. Press, Cambridge, England, U.K., 2000, pp. 195–197.

[39] Walker, G. J., "Transitional Flow on Axial Turbomachine Blading," *AIAA Journal*, Vol. 27, No. 5, 1989, pp. 595–602. doi:10.2514/3.10150

[40] Dong, Y., and Cumpsty, N. A., "Compressor Blade Boundary Layers: Part 2—Measurements with Incident Wakes," *Journal of Turbomachinery*, Vol. 112, No. 2, 1990, pp. 231–240. doi:10.1115/1.2927637

[41] Alexander, W. N., Devenport, W. J., Morton, M., and Glegg, S., "Noise from a Rotor Ingesting a Planar Turbulent Boundary Layer," AIAA Paper 2013-2285, 2013. doi:10.2514/6.2013-2285

[42] Alexander, W. N., Devenport, W. J., Wisda, D., Morton, M. A., and Glegg, S. A., "Sound Radiated from a Rotor and its Relation to Rotating Frame Measurements of Ingested Turbulence," AIAA Paper 2014-2746, 2014. doi:10.2514/6.2014-2746

J. P. Bons
Associate Editor

4. Experimental Investigation of Fundamental Vortical Flow Development across Scales

The contents of this chapter will be submitted for publication in Experiments in Fluids.

Significant portions were previously presented as "Tamara Guimarães, William W. Copenhaver, William C. Schneck, K. Todd Lowe, and Walter F. O'Brien. Swirling Flow Evolution Part 1: Design and Stereo PIV Measurements at Select Planes. In *55th AIAA Aerospace Sciences Meeting 2017*, number AIAA 2017-1620, 2017. doi: 10.2514/6.2017-1620".

Experimental Investigation of Fundamental Vortical Flow Development across Scales

Tamara Guimarães[*], K. Todd Lowe[&], Walter F. O'Brien[$]

[*]*Corresponding author*, tgbucalo@vt.edu, (540)808-3293. Graduate Research Assistant, Mechanical Engineering, 624 McBryde Hall. ORCID: 0000-0002-0189-0792.

[&]Associate Professor, Crofton Dept. of Aerospace and Ocean Engineering, 215 Randolph Hall.

[$]J. Bernard Jones Endowed Professor, Mechanical Engineering, 109 Randolph Hall.

Turbofan engine performance depends highly on the characteristics and conditions of the inlet flow. Swirl distortions, caused by non-uniformities in flows arising from boundary layer or ground/fuselage vortex ingestion are of concern and need to be fully understood to guarantee efficiency and safety of propulsion systems. To investigate a fundamental single-vortex distortion development in a duct at different Reynolds numbers, a StreamVane distortion generating device was designed and experimentally analyzed in a small-scale low-speed wind tunnel (Re 0.47×10^6) and in a full-scale engine testing rig (Re 2.9×10^6). Stereoscopic particle image velocimetry (PIV) was used to measure the three-component velocity fields at discrete measurement planes downstream of the distortion device. Results show that the flow is generated and develops very similarly in both scales, and is mostly driven by two-dimensional (2D) vortex dynamics. Induced velocities arising from the proximity of the vortex to the duct wall causes the vortex center to convect circumferentially around the duct, in the same sense as the vortex rotation, as it travels downstream. Small-scale turbulence results show small scale instabilities related to the development of the vortex. This work shows that the development of this vane-generated, vortex-dominated flow is largely Reynolds number independent, so that details of similar flows can be analyzed in depth in small-scale experiments.

List of Symbols

a_0/D	=	normalized vortex core radius
i	=	unit imaginary number
$image$	=	image vortex
D	=	duct diameter, m
M	=	Mach number
N	=	real shaft speed, rpm
$real$	=	real vortex
Re_D	=	duct-based Reynolds number

SI_i = swirl intensity, deg

SS_i^+, SS_i^- = positive/negative sector swirl, deg

T = referred temperature

u_k = mean velocity component in the k direction, where k = radial (r), horizontal (x), vertical (y), tangential (θ), axial (z), in-plane ($r\theta$), or total ($r\theta z$), m/s

u_k' = fluctuations in the k velocity velocity component, m/s

$\overline{u_k' u_k'}$ = normal component of the Reynolds stress tensor in the k direction

W = complex velocity

W_c = induced velocity

Γ/D^2 = spatially normalized circulation, s^{-1}

α = radial flow angle, deg

β = tangential flow angle, deg

θ^+, θ^- = positive/negative sector

ν = kinematic viscosity, m^2/s

σ_k^2 = variance in the k velocity component

ω = streamwise vorticity

1. Introduction

Vortex-dominated flows are encountered in a number of applications across physical scales, and hold fundamental interest for a number of reasons. For instance, vortices generated from airplane wing tips, by bird wings, and by the movement of fish and other animals in the ocean, all influence how the fluids around those bodies behave locally. In a larger scale, vortices in the atmosphere are responsible for driving phenomena such as hurricanes and tornados. The work of Rockwell (1998) has confirmed the usefulness of Helmholtz's vortex theorems in practical flows such as the formation of leading-edge vortices on delta-wings and on the interaction of vortices with strain and surfaces. To note in Rockwell's and many others' work is the scale independence of vortex-dominated flows—the results from very low Reynolds number experiments have been shown to match the aerodynamics encountered for full-scale vehicles since the phenomena can be scaled purely on geometry and circulation of the vortex. In the present work, these same principles are applied to vortices confined inside aircraft engine inlet ducts in order to provide insight on leading-order flow scaling and effects of vortical flow ingestion by turbine engines.

The performance of turbofan engines depends on the characteristics of the flow entering the engine. While the effects of total pressure and total temperature distortions in engine inlets have been studied and well characterized for decades ((SAE) 1983; (SAE) 1978; Schneck et al. 2013; Seddon and Goldsmith 1999), swirl distortions are still not

fully understood by the engine community. Swirl distortions are angular non-uniformities in the flow, which can be caused by several phenomena, such as boundary layer ingestion, ingestion of ground/fuselage vortices, the presence of cross wind, and adverse pressure gradients ((SAE) 2017).

Swirl distortions may affect the performance of the engine by modifying the incidence angle of the flow in the blades of various stages of the engine (Fredrick and Davis 2011), and generating a temperature distortion behind the compressor due to work variations (Genssler et al. 1987; Pazur and Fottner 1991; Sheoran et al. 2009). Several investigations of the effects of swirl distortion have been performed, both computationally (Anderson and Gibbt 1993; Sheoran et al. 2012; Sheoran et al. 2009), and experimentally. The experimental efforts have employed pressure probes in ducts (Frohnapfel et al. 2015; Hoopes and O'Brien 2013) or cascades (Hobson and Shreevet 1993), and, more recently, particle image velocimetry (MacManus et al. 2017; Murphy et al. 2010; Murphy and MacManus 2011; Zachos et al. 2016).

Single vortex distortions, in the form of tightly wound vortices, may arise in static conditions, due to the ingestion of a ground or a fuselage vortex, or due to cross winds (Siervi et al. 1982). This can cause debris to be ingested into the engine, increase blade erosion due to dirt ingestion (Younghans and Paul 1978), and, since the core of the vortex is a region of total pressure deficit, this may cause engine surge (Motycka 1976). Most of the investigations of vortex ingestion have focused on the mechanisms of formation of inlet vortices, or the generation of vortices inside the turbomachinery system (see AGARD 1990; Sonoda 1987). Previous work on ground vortex ingestion by Brix et al. (2000), and Murphy and MacManus (2011) have provided important insight and conclusions about the generation of inlet vortices, and the relationship between ground clearance and relative speed for inlet vortex formation. However, no work has been done on the development of those vortices after their formation. To characterize the role of inlet vortex ingestions, it is necessary to understand the physics that drive the development of a fundamental vortical structure before it approaches the turbomachine components.

In this work, a single vortex distortion was generated in two different scales to assess the dependence of the vortical flow characteristics and development on Reynolds number, and to describe the physics that drive the development of the flow. Stereoscopic particle image velocimetry (PIV) was used to measure the three-component velocity fields at discrete planes downstream of the distortion in small-scale low speed wind tunnel, and in the inlet

of a full-scale research engine, far enough upstream of the engine to avoid fan effects. The experimental methods used in this work are presented in the following section, and a detailed analysis of the generated flow is presented in the Results section to show that the single-vortex distortion development is driven by two-dimensional (2D) vortex dynamics, and that the mean characteristics of the flow are Reynolds number independent.

2. Experimental Methods

2.1 The LOvort StreamVane Distortion Generator

A single vortex distortion was generated using a StreamVane™ distortion generating device (e.g., Guimarães et al. 2016; Hoopes and O'Brien 2013), with the design inputs shown in Fig. 1. The design flow is to be generated exactly downstream of the StreamVane, at 0 diameters downstream of its trailing edge.

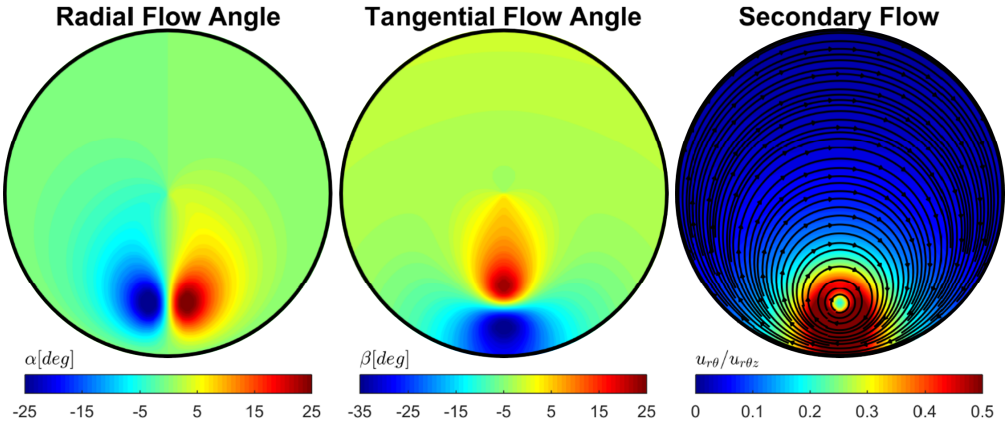

Fig. 1 Design flow angles and secondary flow at the exit plane (trailing edge) of the LOvort StreamVane.

The strength of the vortex was chosen based upon simulation results of a highly distorted flow containing a tightly-wound vortex ingested by an engine on a hybrid-wing body aircraft concept (Gatlin et al. 2012), as described by Guimarães et al. 2017a, and the vortex was modeled as a Lamb-Oseen vortex (LOvort), with the complex velocity described in Eq. 1:

$$W(x+iy) = u_x - iu_y = \frac{\Gamma}{2i\pi}\frac{1}{x+iy}\left[1 - exp\left(-\frac{|x+iy|^2}{a_0^2}\right)\right] \quad \text{(Eq. 1)}$$

where $\Gamma/D^2 = -55.5\ s^{-1}$ and $a_0/D = 0.05$. The location of the center of the vortex was chosen as 70% of the blade tip radius, since Brix et al. (2000) determined that a vortex closer to the wall would be distorted by wall interactions.

The wall boundary conditions were simulated by modeling a complementary imaginary vortex, and the throughflow velocity was designed as constant. All plots will be presented from a forward looking aft (FLA) point of view, with the tangential velocity component being positive in the counterclockwise direction, and the radial velocity component being positive radially outward. Radial flow angles ranged from -25 to 25 degrees, and tangential flow angles from -35 to 25 degrees. The resulting small-scale StreamVane distortion device is shown in Fig. 2 (left). Its diameter was 0.15 m (6 inches), maximum chord length was 0.082 m (3.25 inches) and it was built in Acrylonitrile Butadiene Styrene (ABS) through additive manufacturing.

Fig. 2 Small-scale StreamVane (left), and full-scale StreamVane (right) presented to scale.

Once the results from the small-scale experiment were verified and satisfactory, the StreamVane was scaled up for experiments in the full-scale rig, and built using additive manufacturing in black ULTEM 9085. The full-scale StreamVane is also shown in Fig. 2 (right). The diameter of the full-scale StreamVane was 0.534 m (21 inches), and its maximum chord length was set to 0.18 m (7.2 inches). The overall design was scaled directly from the small-scale, yielding vanes longer than 0.18 m, which were manually cropped in the CAD design before manufacturing, since the longer vanes generated little turning and generate thicker wakes. The thickness of the vanes was set to 3.175 mm (1/8 inch) to minimize the effects of the wakes generated by the vanes in the flow.

2.2 Small-Scale Wind Tunnel

The small-scale experiment was performed in the Virginia Tech Turbomachinery and Propulsion Research Laboratory wind tunnel, which is equipped with a square-to-round outlet designed to fit a 0.15 m diameter pipe. The schematics of the experimental setup, including the tunnel outlet, are shown in Fig. 3. The upstream bulk velocity for

this tunnel was 49.3 ± 0.7 m/s, Mach 0.14, and duct Reynolds number of around 470,000, where $Re_D = u_\infty D/\nu$, and ν for 300 K is 1.57×10^{-5} m^2/s.

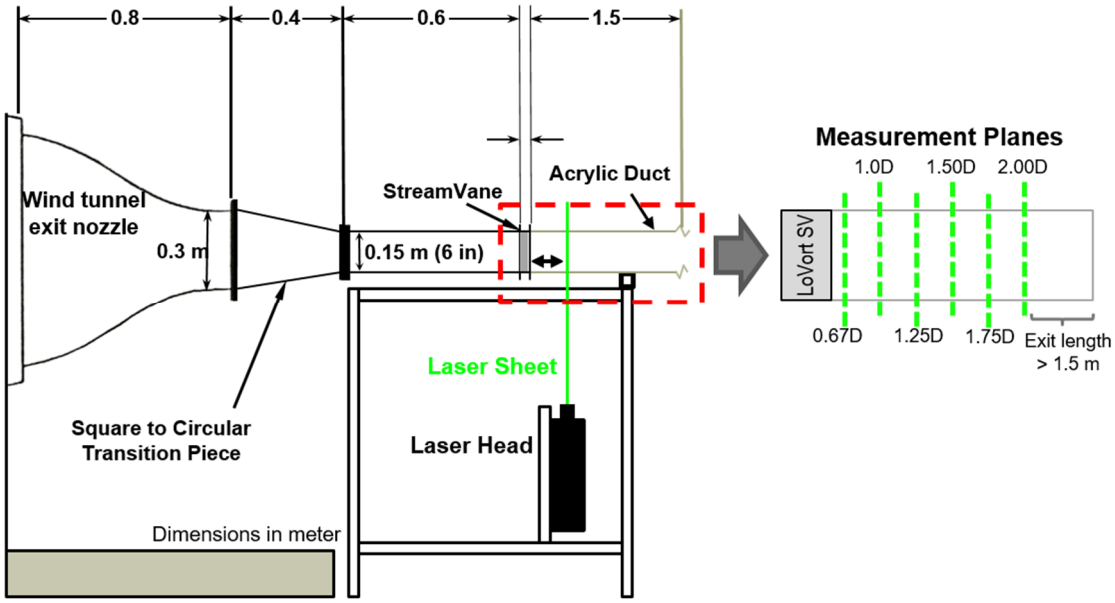

Fig. 3 Small-scale wind tunnel setup and measurement planes.

Stereoscopic particle image velocimetry was used to measure the three-component velocity fields at six discrete measurement planes downstream of the StreamVane: 0.67, 1.00, 1.25, 1.50, 1.75, and 2.00 diameters downstream of the leading edge (StreamVane thickness was 0.54D). Two LaVision Imager Pro X 4M cameras were placed in a stereo configuration for imaging the flow. They were equipped with 50 mm Nikon lenses and Scheimpflug adapters, yielding a viewing image size of approximately 0.16 m to ensure the entire inside of the duct was captured. A thousand images were acquired in each plane at 4 Hz, with a time delay of 18 µs between the first and second frame of the image. The laser used to illuminate the particles was a Quantel Evergreen 200 double-pulsed Nd:YAG laser, rated 200 mJ/pulse, emitting at 532 nm. A LaVision collimator and a -10 mm cylindrical lens were placed at the exit of the laser to treat the laser beam into a 3 mm (0.12 in) thick laser sheet for the measurements. The flow was seeded from upstream of the wind tunnel blower with 0.2-0.3 µm diameter particles of fluid A (glycerol + water) using a Concept Engineering Ltd Colt 4 Seeder. The PIV measurement section of the wind tunnel consisted of a 0.15 m in diameter, 1.52 m long optically clear cast acrylic pipe, shown in Fig. 4.

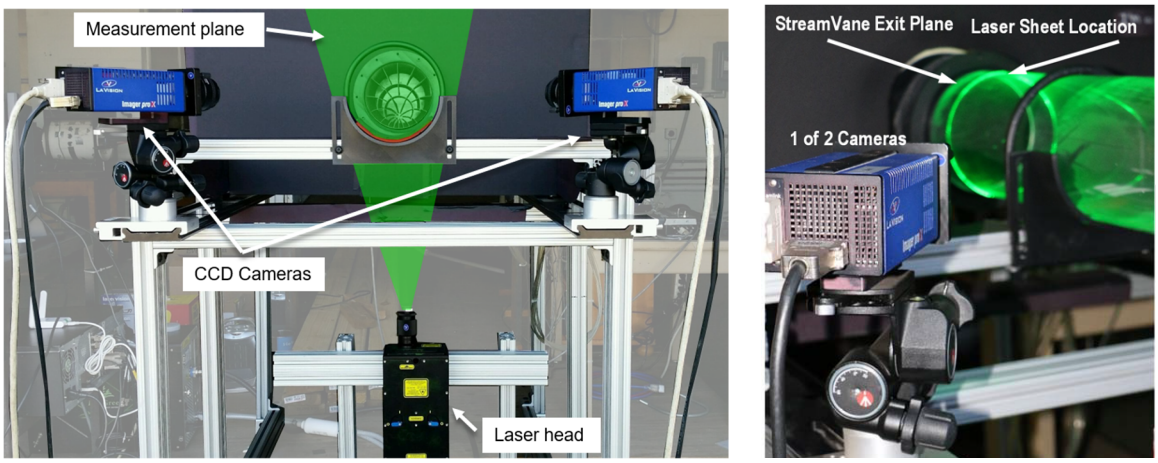

Fig. 4 PIV experimental setup (left), and details of the laser sheet intersecting with the acrylic pipe (right, (Sanders et al. 2016)).

2.3 Full-Scale Testing Rig

The full-scale testing rig was comprised of tunnel sections and a bellmouth for inlet flow conditioning, one particle seeding distribution device, the StreamVane installed in a custom-built rotator, a customized test section with optical access for the cameras and the laser sheet, connection tunnel sections and the Pratt and Whitney Canada JT15D-1 research engine mounted to a test stand. Measurement planes were defined far enough upstream of the fan, so that fan effects were avoided. Axial average bulk velocity for this setup was 87 m/s (70% corrected fan speed ($N/\sqrt{T}$), Mach 0.25), yielding a duct Reynolds number of 2.9 million, based on a duct diameter of 0.53 m (21 inches).

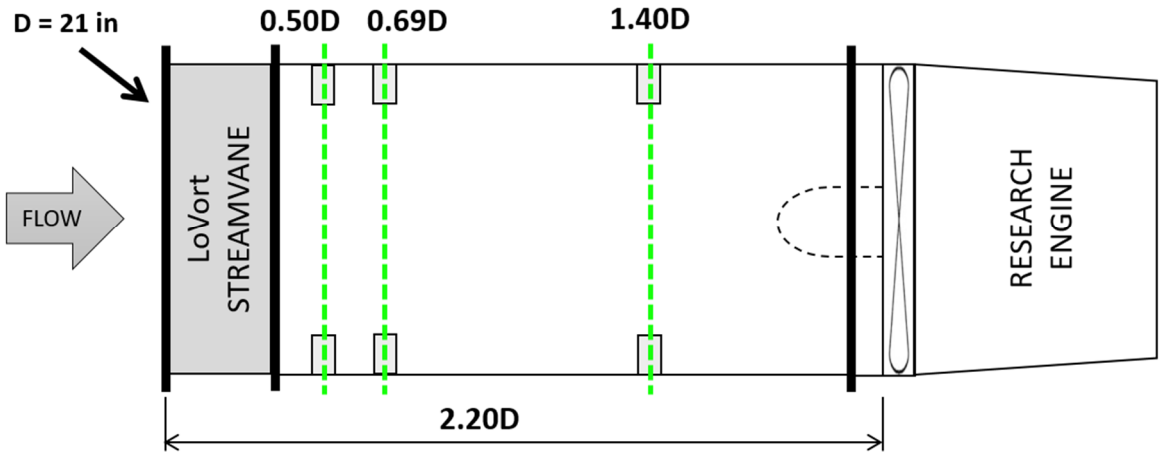

Fig. 5 Full-scale measurement planes relative to the leading edge of the StreamVane.

Two LaVision Imager Pro X 4M CCD cameras were mounted in a stereoscopic configuration, equipped with 24 mm Nikon lenses with aperture set to 5.6, and Scheimpflug adapters. Data were taken in three discrete measurement planes downstream of the StreamVane: 0.50, 0.70, and 1.40 diameters relative to the StreamVane leading edge (StreamVane thickness was 0.34D). The position of the StreamVane relative to the fan face was maintained constant at 2.20 diameters. For the 0.50 and 0.70D measurement planes, the cameras were facing upstream of the flow, and for the 1.40D they were facing downstream. Due to the limited optical access available in the full-scale environment, data were taken in slices. The field of view for each slice was maximized to ensure enough overlap, and the StreamVane was rotated by 30 degrees between each measurement. The same laser system was used as the small-scale experiment. A thousand images were acquired in each measurement slice at 4 Hz, with a time delay of 5 μs between the first and second frame of the image. Further details of the setup were previously presented in Guimarães et al. (2017c).

Table 1 summarizes the main properties of the small-scale and the full-scale experiments.

Table 1 Summary of Small- and Full-Scale Experiment properties

Experiment	Duct Diameter	Average Bulk Axial Velocity	Reynolds Number	Mach Number	Measurement Planes
Small-Scale	0.15 m (6 in)	50 m/s	0.47 M	0.14	0.67, 1.00, 1.25, 1.50, 1.75, 2.00D
Full-Scale	0.53 m (21 in)	87 m/s	2.90 M	0.25	0.50, 0.69, 1.40D

3. Analysis

3.1 Small-Scale PIV Processing

Images were first processed in the LaVision DaVis software using stereo cross-correlation. A sliding background was subtracted, and particle intensity normalization was performed, at a 2-pixel scale. Then, multi-pass processing was used, where the first pass consisted of a 128x128 square window with 75% overlap, and the following 2 passes consisted of a 64x64 square window with 75% overlap. A built-in median filter was used to remove and replace spurious vectors based upon the neighboring vectors. Vectors that did not fall within an interval of the average ±2 times the standard deviation were removed, and vectors with a peak ratio (the ratio of the largest correlation peak to the second largest correlation peak in an interrogation window) of less than 1.3 were deleted. One pixel was equivalent to 76 μm for this configuration, yielding a spatial resolution of 4.9 mm for the smaller interrogation window.

Since the laser sheet was entering and exiting the acrylic pipe, laser glare was an issue. The data was then further processed to ensure that spurious and biased vectors were deleted. A statistical analysis of the flow was performed, and it was found that the most relevant parameters for data filtering in this experiment were data count, axial velocity variance (σ_z^2), horizontal velocity variance (σ_x^2), axial velocity magnitude (u_z), and horizontal velocity magnitude (u_x). Based on the cameras being placed along the horizontal axis of the experiment, it was expected that the u_x and u_z components of velocity would present more uncertainty and spurious data, since the slightest misalignment between calibration plane and laser sheet position would cause erroneous correlations. Horizontal velocity components greater than 27 m/s were filtered, as were axial velocity components smaller than 25 m/s. The velocity variations were limited to $\pm$ 40 m/s in the most turbulent case and $\pm$ 14 m/s in the case with less turbulence.

3.2 Full-Scale PIV Processing

One of the main challenges with this experimental setup is seeding, as presented previously by Nelson (2014). For this particular distortion case, it was a challenge to seed the core of the generated vortex consistently. With that, it was not possible to obtain turbulence information about the flow with sufficient confidence to draw any conclusions, however the amount of data collected was enough to observe the mean characteristics of the flow.

LaVision Davis was used to process the images using stereo cross-correlation. Background images were taken in between the measurement slices, averaged, and then subtracted from the PIV images. Then, multi-pass processing was used, where the first pass consisted of a 128x128 square window with 50% overlap, and the following 2 passes consisted of a 64x64 round window with 75% overlap. A built-in median filter was used to remove and replace spurious vectors based upon the neighboring vectors. Vectors that did not fall within an interval of the average ±2 times the standard deviation were removed, and vectors with a peak ratio of less than 1.3 were deleted. Vectors in which the in-plane velocities (u_x and u_y) did not fall within $\pm$ 30 m/s, or the axial velocity (u_z) was smaller than 25 m/s or greater than 125 m/s, were deleted. One pixel was equivalent to 150 μm for this configuration, yielding a spatial resolution of 9.5 mm for the smaller interrogation window.

To obtain full velocity profiles in each measurement plane, the slices of data were stitched together in MATLAB through the polar binning method described by Guimarães et al. (2017b).

3.3 Uncertainties

Quantifying PIV uncertainty is always a challenge, due to the amount of variables that may contribute to increasing the experimental uncertainty of the setup, which are complex and not easily taken into consideration. According to Raffel et al. (2007), PIV data under ideal conditions can have a resolution of up to about 0.1 pixels, limited by the typical correlation peak interpolation. With that, an uncertainty analysis based on the uncertainty of the measurement in the particle displacement can be performed. Based on the scale factors calculated by the software, the displacement uncertainty is 0.00761 mm for the small-scale experiment, and 0.015 for the full-scale. Assuming no uncertainty in the time measurements, the uncertainty in velocity would be 0.42 m/s, 0.86% of the small-scale bulk velocity, and 3.0 m/s for full-scale, 3.45% of the bulk velocity. For flow angle calculations, the uncertainty can be obtained from their definitions ($\alpha = tan^{-1}\, u_r/u_z$ and $\beta = tan^{-1}\, u_\theta/u_z$), resulting in an uncertainty $\sqrt{2}$ times higher than the velocities, therefore $\pm$1.22% for the small-scale, and $\pm$4.88% for full-scale, using a small angle approximation. These results are consistent with the uncertainty values calculated by the LaVision software (Wieneke 2015), which were mostly lower than 0.5 m/s for the small-scale, and 3 m/s for the full-scale experiment.

4. Results and Discussion

The LOvort StreamVane consists of a single vortex distortion, centered at about 70% of the radius, and located at the bottom dead center of the duct, similar to what might be found in the inlet of a turbofan engine ingesting a ground vortex, or subjected to cross winds in embedded configurations. Two distinct experiments were performed to analyze the behavior of the generated vortex: a small-scale low speed wind tunnel experiment, and a full-scale test. The results to be presented indicate that the mean flow development is Reynolds number independent, and that secondary flow development is driven by 2D vortex dynamics.

In the mean-flow results discussed to follow, the design targets at the StreamVane exit for secondary velocities and flow angles are presented along with small-scale and full-scale experimental results. Small-scale experimental results are presented at planes z = 0.67D and 1.50D, while full-scale results are presented at the closest planes for comparison, z =0.50D, 0.69D, and 1.40D. Flow measurements at 0.50D in full-scale are different from the design, since the flow has already started to develop. The black outer ring in the figures represents the duct inner diameters

that contain the flow, and blank regions inside the ring are where data was filtered due to lack of quality caused by laser glare in the duct/windows.

The mean normalized secondary flow velocity profiles shown in Fig. 6 were obtained by averaging the in-plane components of the velocity field ($u_{r\theta} \equiv \sqrt{u_r^2 + u_\theta^2}$), and dividing them by the mean local total velocity ($u_{r\theta z} \equiv \sqrt{u_r^2 + u_\theta^2 + u_z^2}$). The StreamVane is manufactured to generate the design profile at the exit of the device, which would be 0D downstream of the trailing edge. Due to limitations in the experiment, it was not possible to take measurements at that location, so the first measured plane downstream was at 0.50 diameters downstream of the leading edge in the full-scale experiment. At that plane, it is possible to see that the flow has started convecting due to the interactions with the wall, and the vortex has migrated in the same direction as the vortex rotation by less than 5 degrees. It is also observed that there are three spots of higher in-plane velocity, around the vortex, suggesting that the core of the vortex at that plane comprises three smaller vortices. This will be explained later in this section, when the axial velocity profiles are discussed.

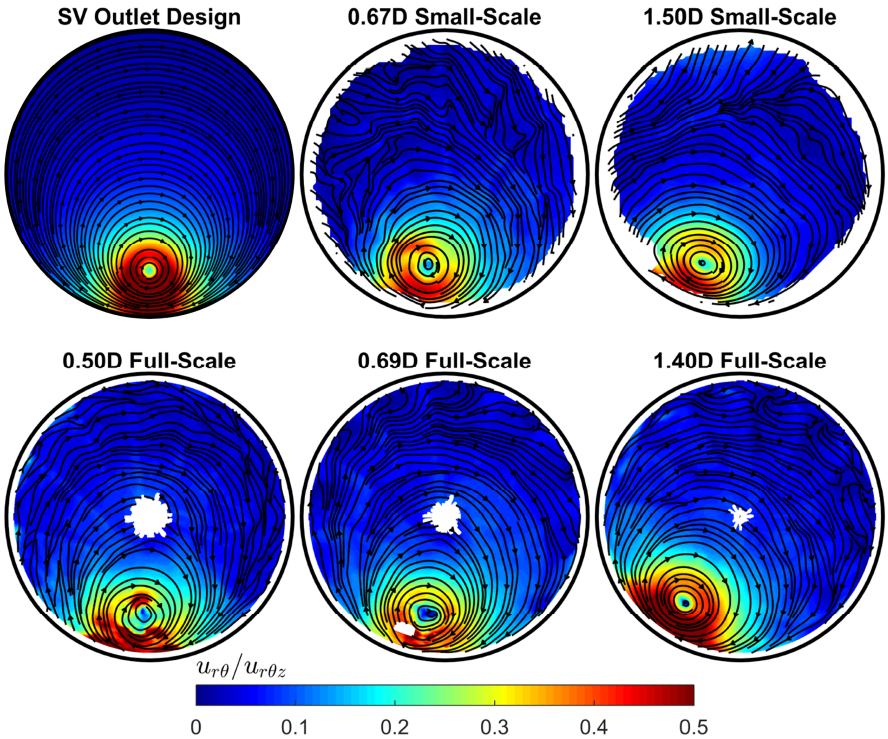

Fig. 6 Secondary velocity profiles. Lines represent the mean direction of the flow and the color plot shows the velocity intensities, normalized by the average bulk axial velocity.

When focusing on the secondary velocity profiles, it seems that the vortex has maintained its overall strength and shape throughout the development, although the magnitude of the velocity around the vortex is not as uniform as design, with significantly higher values between the core and the wall. This indicates that the vortex development is highly governed by two-dimensional vortex dynamics, which state that for an incompressible flow, the fluid velocity can be determined by the vorticity of the flow, up to an irrotational far field component through the Biot-Savart law (Saffman 1992). It is also possible to observe some secondary flow motion from the vortex sheets being shed from the vanes of the StreamVane in the low turning regions of the 0.50D and 0.67D planes. This seems to mix quite quickly, and is almost unobservable at the 1.50D plane. The small-scale data have been successfully compared to an inviscid and incompressible low order flow development model, in which the in-plane velocity set as the initial condition was determined from the same goal profiles used to design the experimental distortion screen, and the axial development of the flow was treated as the time evolution of the profile (Schneck et al. 2017). The similarities of the small-scale flow with the full-scale experiment indicate that there are no further physics that need to be described for the higher Reynolds number flow that is far enough upstream of the engine fan face and outside of the duct inner-diameter boundary layer. This has been previously observed by Sanders et al. (2016) for a more complex StreamVane pattern, and also compared to computational fluid dynamics results.

To further test this hypothesis, a simple point vortex convection model was generated to compare to the experimental results. A point vortex was simulated in the same position as the vortex in the design profile, shown in Fig. 7 (top), and the circular boundary of the duct was generated by means of an image vortex placed outside of the duct diameter (not shown in figure) (Bühler 2002; Pozrikidis 2011). The Euler method was used to solve the ordinary differential equation $dx/dt = U(x,t)$ using the initial position of the vortex as the initial condition. As flow develops downstream, the vortex convects along the duct due to the induced velocity imposed to it by the image vortex that has the complex velocity

$$W_c(x+iy) = \frac{-i\Gamma_{image}}{2\pi} \frac{1}{\left[(x+iy)_{real} - (x+iy)_{image}\right]} \qquad \text{(Eq. 2)}$$

The vortex position for each experimental measurement plane was calculated and plotted as vectors on top of the secondary velocity profiles presented previously in Fig. 6, and most small- and full-scale experimental data seem to

agree well with the model. The only plane that is slightly off is the further downstream full-scale plane, 1.40 D, indicating that the flow at that point in full-scale may be already subjected to some influence from the engine.

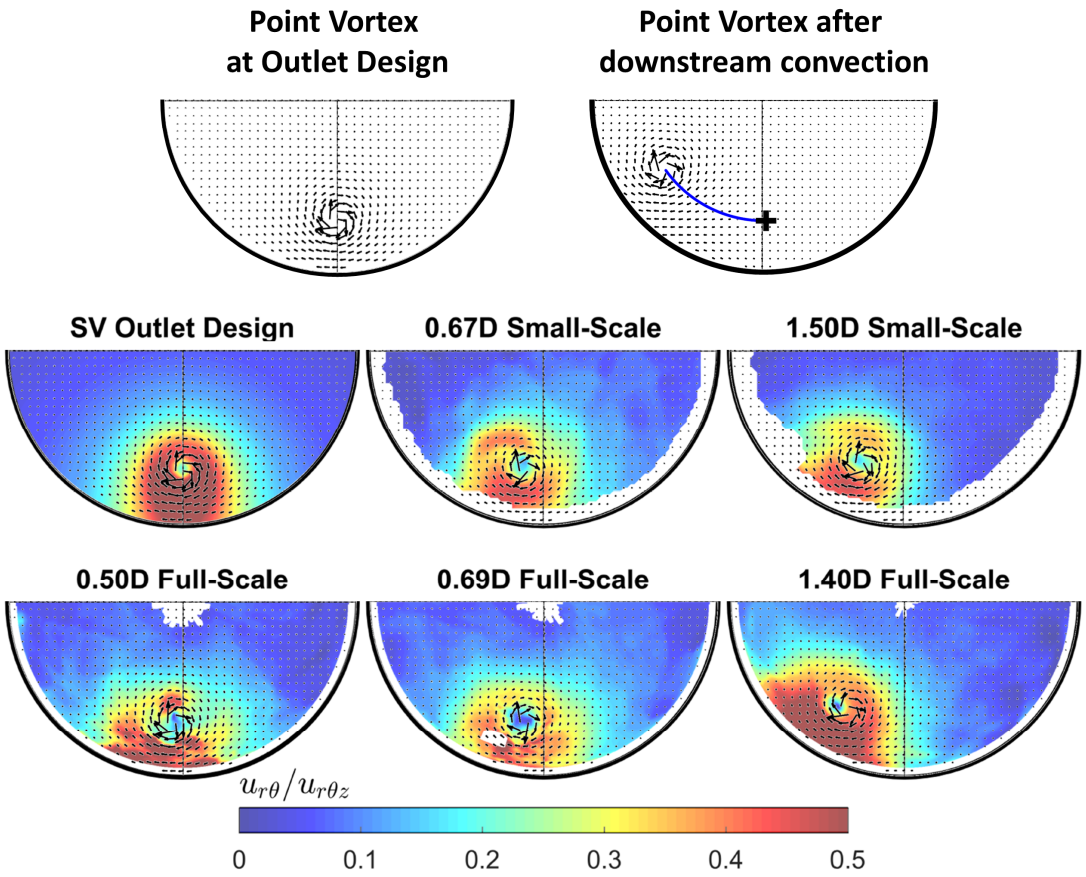

Fig. 7 Point vortex model downstream convection example. Vectors from simplified image vortex model, contours for secondary velocity magnitude from small-scale and full-scale experiments.

The StreamVane is designed to generate swirl, which means that it is optimized to meet tangential flow angle parameters. The resulting tangential and radial flow angles for this experiment are shown in Fig. 8. With these details of the flow, it is possible to observe more of the characteristics of the vortex and its development in the duct. The tangential flow profiles show that the higher absolute values seem to all migrate with the vortex, reinforcing the fact that the overall shape of the vortex is preserved. The maximum and minimum flow angle values do not vary drastically, indicating little changes in the characteristics of the in-plane flow. The radial flow angles present a little more of the influence of the vanes in the generation of the vortical structure of the flow. These results reinforce the dominance of mean-flow vortex-dominated convection, with little influence from viscous or turbulence effects.

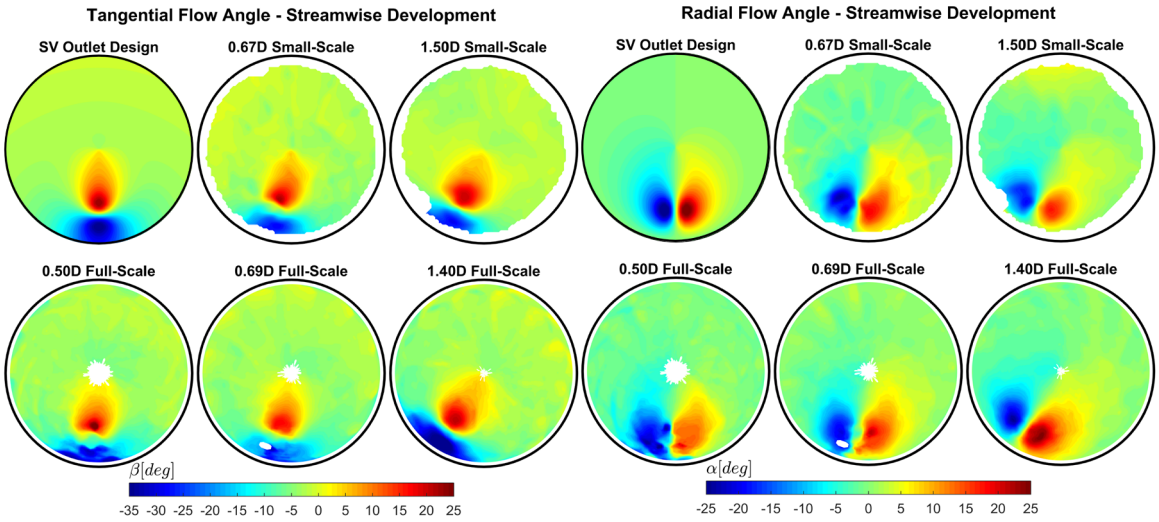

Fig. 8 Tangential (left), and radial (right) flow angle profiles.

Figure 9 presents a comparison between the maximum absolute tangential and radial flow angles across the radius of all the measurement planes presented in Fig. 8. The full-scale StreamVane seem to overshoot the higher angles, relative to the small-scale flow angles, but since the near-wall data was filtered for the small-scale experiment, this cannot be verified. The overall shape of the distortion distribution is maintained across scales, as shown previously for more complex geometries by Guimarães et al. (2017c) and Sanders et al. (2016). Most of the other regions of the radius seem to agree well across scales, mainly when taking into account the uncertainty of the measurements (plots for the same values with error bars are presented in the Appendix). It appears that the distortion is closer to the wall in the full-scale measurements, which may be responsible for part of the differences presented between the scales, mainly in the radial flow angle comparisons.

Swirl intensity is one of the swirl descriptors defined by the SAE S-16 Committee to quantify inlet swirl distortions. It is defined as $SI_i = \frac{SS_i^+ \times \theta_i^+ + |SS_i^-| \times \theta_i^-}{360}$, where SS_i^+ is the integrated swirl angle over the θ_i^+ extent, and it is used to capture the predominant swirl angle in degrees at the measurement plane ((SAE) 2017). Calculated swirl intensities for the same measurement planes are shown in Fig. 10. As with the maximum flow angles, for the majority of the radius of the measurement planes, the swirl intensity angles of the full-scale measurement planes are higher than the small-scale. We observe a general trend to overshoot the magnitude of the higher angles in full-scale, which is a feature mainly of the differences between the different StreamVane devices, and have no connection to the

development of the flow. The main conclusion to be drawn from these flow angle measurements is that a comparable secondary flow profile is being generated in two different scales, and analyzing the development of the small-scale flow is enough to gain insight on how the flow will develop in the full-scale environment, before it interacts with the features of the turbofan engine, decreasing the costs of the experimental work involved.

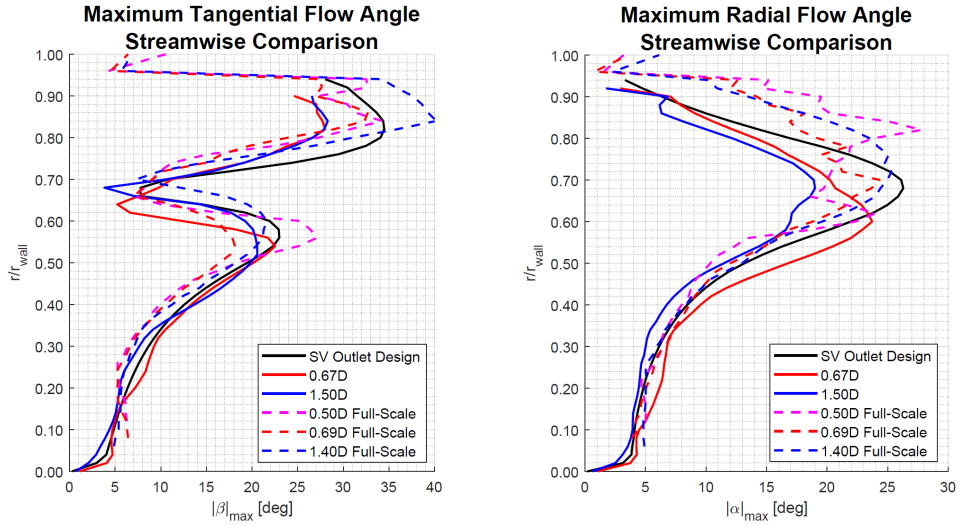

Fig. 9 Maximum absolute tangential and radial flow angle comparison between small and full-scale experiments.

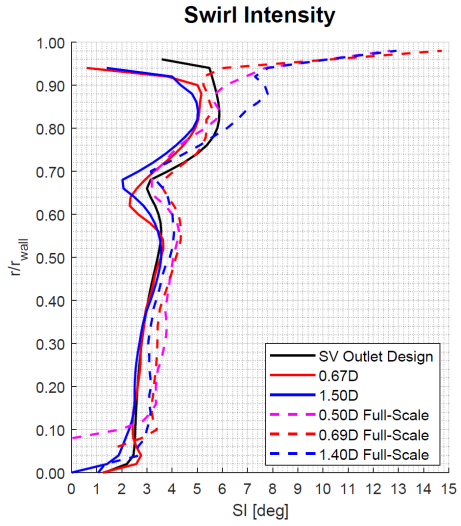

Fig. 10 Swirl intensity comparison between small and full-scale experiments.

This StreamVane was designed with a constant axial velocity component. However, adding a distortion device comprised of vanes to generate turning will have an influence in the velocity in the axial direction, mainly due to

blockage. To better observe the effects of the vanes to the flow, and also to the distortion, the mean axial velocity profiles, normalized by the average bulk axial velocity, are presented in Fig. 11, alongside with the CAD model of the full-scale StreamVane. The full-scale measurements for the axial velocity component were not as satisfactory as the in-plane components, and there is some spurious data left from the effects of glare and the stitching process, but the main overall features of the flow are maintained and can be observed, especially when taking the small-scale results as a reference. The 0.50D plane presents a high axial velocity deficit in the bottom dead center, caused by the high blockage introduced to the flow by the array of vanes that generate the bottom of the vortex. The wakes of the vanes are very well delimited in the 0.50D full-scale and the 0.67D small-scale measurement planes, and they start to mix as the flow develops downstream, which is expected for low Mach number flows. More interestingly, it is possible to observe the axial development of the vortex. This is not as clear when looking at the full-scale measurements, but at the 1.40D plane it is possible to observe some of that, while also observing a region of high axial velocity in the center of the vortex. This may be a result of the higher Reynolds number, presenting less effective blockage as the flow passes through the center of the vortex-generating ring in the StreamVane, and taking longer to mix, being a result of the distortion device, not of the flow development.

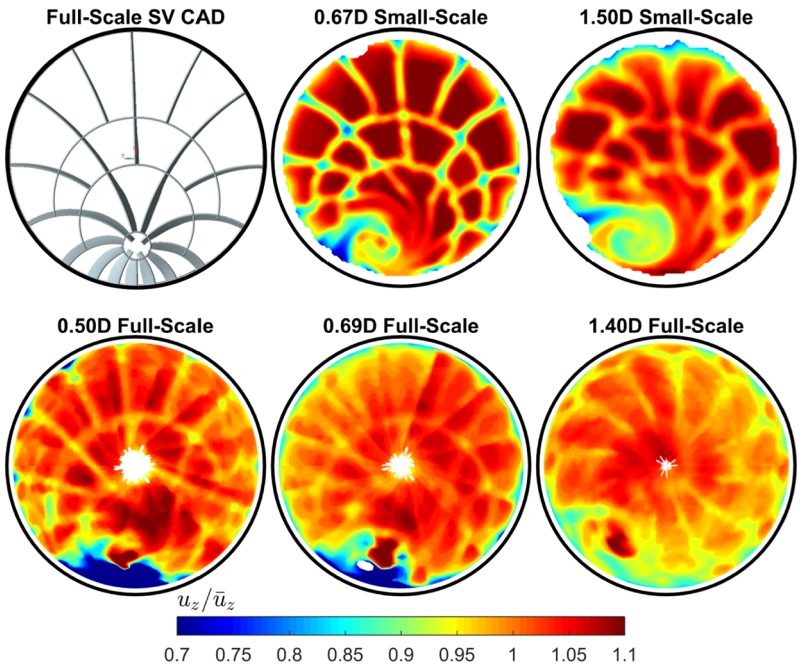

Fig. 11 Full-scale StreamVane model, small-, and full-scale axial velocity profiles normalized by the average bulk axial velocity.

Though the behavior of the single-vortex distorted flow is very similar across scales, there are details that are observed in the mean flow results of the full-scale engine test that were not immediately clear from the small-scale results, most likely due to the resolution of the PIV measurement system. As mentioned when analyzing the secondary flow results, at the 0.50D full-scale measurement plane, it is possible to observe indications of three distinct vortices formed from the StreamVane, which later combine into one stronger vortex. This is even more obvious when looking at visualizations present in the particle images; one such example is presented in Fig. 12. These tip vortices are generated by the overall shape of the vortex-generating feature in the StreamVane device shown previously in Fig. 2, which consists of a ring that connects the tips of four longer turning vanes. Given that the regions outside of the inner core of the vortex are well generated, it is suggested that those tip tabs are shortened for future SV designs to prevent the generation of tip vortices.

Even though the discrete vortex structure was not obvious in the mean flow for small-scale, an analysis of the streamwise vorticity profiles of the small-scale experiment confirm that this also happens in that scale, as shown in Fig. 13. At the 0.67D plane, it is possible to see three relatively distinct regions of higher vorticity, indicating those tip vortices before combining into one single stronger vortex. There is also a region of increasing vorticity following the vortex development, similar to that observed by Murphy and MacManus (2011), which is believed to originate from vorticity tilting from the boundary layer in the inside of the duct into axial vorticity, as described by Klemp (1987), providing a continuous convection of vorticity into the vortex core.

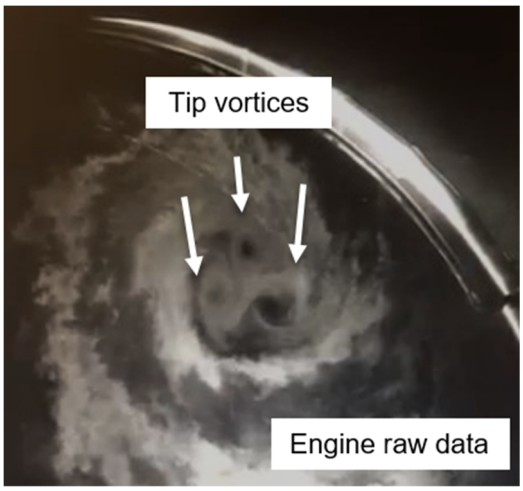

Fig. 12 Raw image showing three tip vortices generated by the StreamVane at the 0.50D full-scale measurement plane.

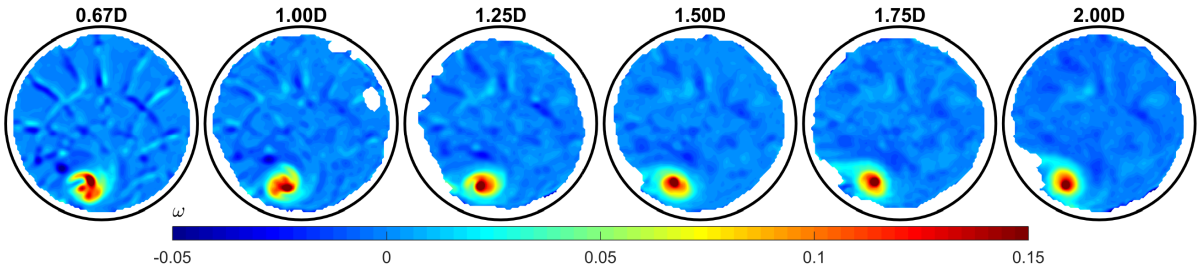

Fig. 13 Mean streamwise vorticity of the small-scale results.

To analyze the turbulent characteristics of the development of the vortex, it is necessary to first assess the instabilities related to its generation, as suggested by Devenport et al. (1996), and Murphy and MacManus (2011). A qualitative observation of the instantaneous snapshots (not shown) of the small-scale data at several planes, and the full-scale data at the 1.40D plane show that the vortex is stable as it is generated, suggesting that instabilities presented downstream of the generation are related to the turbulence intrinsic to the vortex development. To illustrate this, the normal components of the Reynolds stress tensor are presented in Fig. 14. The regions of growing small-scale instabilities indicate the development of the vortex and growing turbulence associated with its transition to turbulence. Interestingly, as flow approaches the fan in a full-scale engine, the acceleration generated by the fan and core suction induce axial stretching of the vortex, increasing its stability and reducing its turbulent characteristics, as shown experimentally by Guimarães et al. (2018b), confirming the numerical observations of Delbende et al. (2002) and Nolan (2001).

One last point to make is regarding the appearance of local instabilities and turbulences due to the presence of vanes, even in regions further away from the vortex. The turbulence is higher at the plane immediately downstream of the StreamVane due to the intense local shear from the vane wakes, but these features rapidly mix and attenuates as flow develops downstream. Figure 15 shows the sector averaged stresses for each streamwise measurement position. The full lines represent the top half of the plots presented in Fig. 14, where the vane wakes are more pronounced, and the dashed lines are the bottom half of the plots, being representative of the vortex turbulence. Overall, there is a decrease in the average Reynolds stress level of the top half, and an increase in the level of the bottom half, supporting the claims presented before. For more details on the effects of small-scale StreamVane turbulence, refer to Guimarães et al. (2017b), and for full-scale StreamVane turbulence refer to Guimarães et al. (2018a) (Chapter 3). As concluded in these two aforementioned references, the turbulent length scales introduced to

the flow by the StreamVane vanes are much smaller than the length scales of the vortical features generated by the StreamVane, thus providing additional representative realism to the secondary flow features generated.

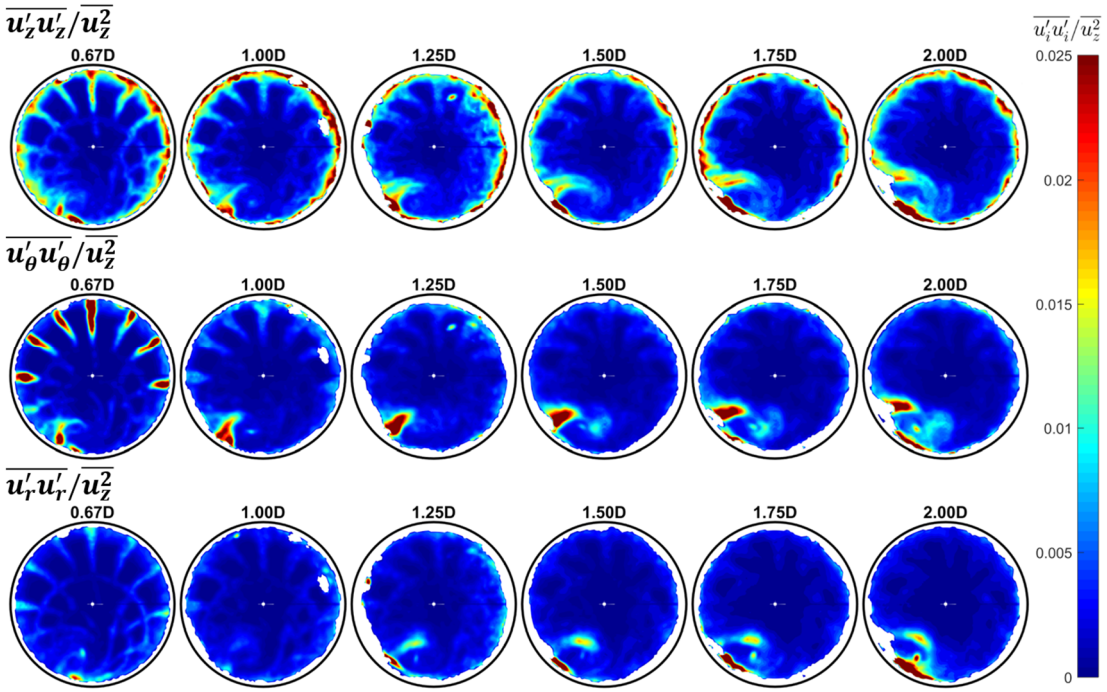

Fig. 14 Normal components of the Reynolds stress tensor in the axial ($\overline{u_z'u_z'}$) tangential ($\overline{u_\theta'u_\theta'}$) and radial ($\overline{u_r'u_r'}$) directions for the small-scale experiment, normalized by the average bulk axial velocity, $\overline{u_z^2}$

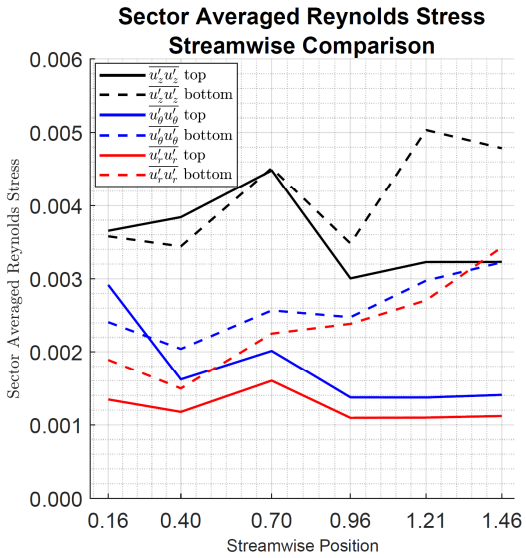

Fig. 15 Sector averaged Reynolds stress components. Results show averaged values for top and bottom halves of plots presented in Fig. 14.

5. Conclusions

A single-vortex distortion was generated through the StreamVane method in two different scales: a small-scale low speed wind tunnel, and in the inlet of a full-scale engine testing rig. Three-component velocity data was taken with stereoscopic image velocimetry at pre-defined positions downstream of the generation of the distortion to analyze how the flow develops along a duct.

Mean flow results of velocities and flow angles indicate that the generation and development of the vortex is similar across scales, not depending on the Reynolds number of the flow, and being governed mostly by two-dimensional vortex dynamics. Details of the StreamVane are responsible for an overshoot in the generation of the full-scale tangential angles, and swirl intensity in the flow, but the overall characteristics of the flow are generated well in both scales.

A deeper analysis of the development of the vortex was done in relation to turbulence and vorticity in the small-scale results. Three tip vortices are generated right downstream of the StreamVane, and later combine into one single vortex core. With the development of the vortex, the instabilities in the flow around it increase, as expected for a vortex in an axial flow. Instabilities introduced to the flow by the StreamVane vanes are evident right downstream of the screen, but decrease as flow develops.

The results of this work indicate that investigations of complex inflow distortions can be performed in small-scale wind tunnel environments, decreasing costs associated with full-scale engine tests. To improve these capabilities, it is recommended that small-scale wind tunnels are equipped with features simulating those of full-scale engines, such as spinners, rotors, and fans.

Acknowledgments The authors would like to acknowledge NIA and NASA Langley Research Center for funding this work in association with NASA's Environmentally Responsible Aviation Project (NIA cooperative agreement RD-2917), project managers Fay Collier (LaRC), Hamilton Fernandez (LaRC), Greg Gatlin (LaRC), and Bo Walkley (NIA). An additional thanks to CAPES for financial support to Tamara Guimarães.

Appendix: Errors in flow angle comparisons

This appendix presents the maximum flow angle comparisons between small and full-scale experiments when the error bars are added to the previously presented plots. The error is calculated from the uncertainty values presented previously (±1.22% for small-scale, ±4.88% for full-scale).

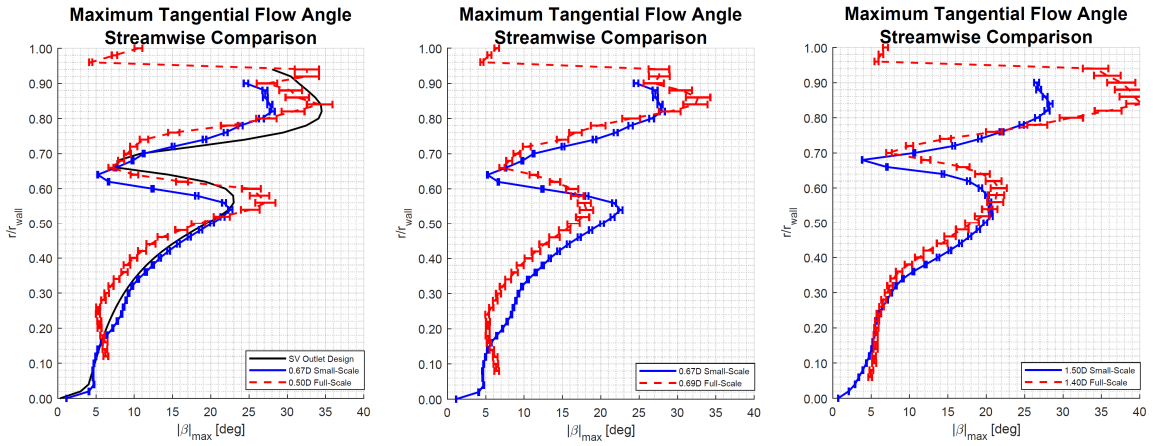

Fig. 16 Maximum tangential flow angle comparison between small and full-scale experiments at each plane with error bars.

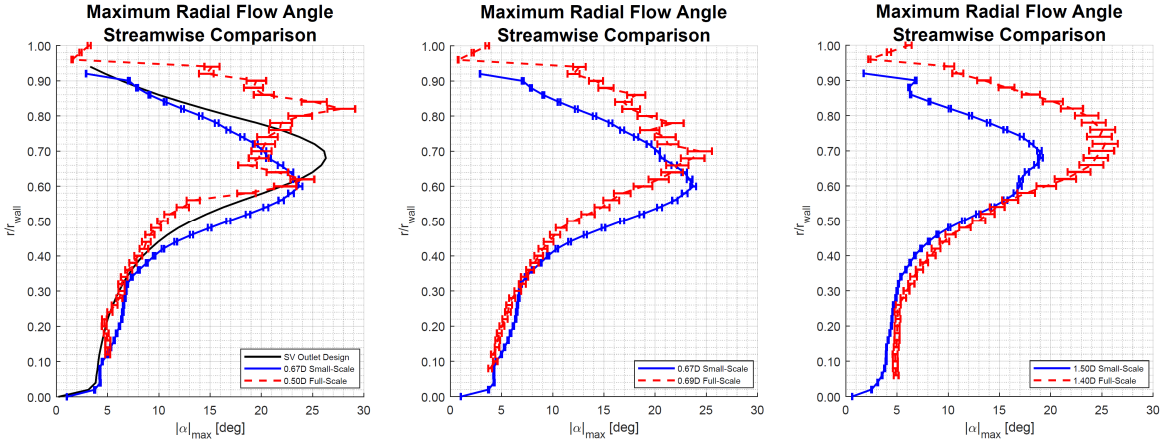

Fig. 17 Maximum radial flow angle comparison between small and full-scale experiments at each plane with error bars

References

Advisory Group for Aerospace Research and Development (AGARD) (1990) Secondary Flows in Turbomachines. AGARD Conference Proceedings, No. 469.

Anderson BH, Gibb, J (1993) Study on vortex generator flow control for the management of inlet distortion. J Propul Power, 9(3):422-430

Brix S, Neuwerth G, Jacob D (2000) The inlet-vortex system of jet engines operating near the ground. AIAA Paper 2000-3998

Bühler O (2002) Statistical mechanics of strong and weak point vortices in a cylinder. Phys of Fluids, 14(7):2139-2149

Delbende I, Rossi M, Le Dizès S (2002) Stretching effects on the three-dimensional stability of vortices with axial flow. J Fluid Mech, 454:419-442

Devenport WJ, Rife MC, Liapis SI, Follin GJ (1996) The structure and development of a wing-tip vortex. J Fluid Mech, 312:67-106

Fredrick N, Davis M (2011) Investigation of the effects of inlet swirl on compressor performance and operability using a modified parallel compressor model. ASME Paper GT2011-45553

Frohnapfel DJ, O'Brien WF, Lowe KT (2015) Fan Response to Inlet Swirl Distortions Produced by Boundary Layer Ingesting Aircraft Configurations. AIAA Paper 2015-3804

Gatlin G, Vicroy D, Carter M (2012) Experimental Investigation of the Low-Speed Aerodynamic Characteristics of a 5.8-Percent Scale Hybrid Wing Body Configuration. AIAA Paper 2012-2669

Genssler HP, Meyer W, Fottner L (1987) Development of intake swirl generators for turbo jet engine testing. AGARD Propulsion and Energetics 68th (A) Specialists' Meeting. Paper AGARD-CP-400

Guimarães T, Copenhaver WW, Schneck WC, Lowe KT, O'Brien WF (2017a) Swirling flow evolution part 1: design and stereo PIV measurements at select planes. AIAA Paper 2017-1620

Guimarães T, Frohnapfel DJ, Lowe KT, O'Brien WF (2017b) Streamwise development and turbulence characterization of a twin-vortex inlet distortion for turbofan applications. AIAA Paper 2017-4992

Guimarães T, Lowe KT, O'Brien WF (2016) An overview of recent results using the StreamVane method for generating tailored swirl distortion in jet engine research. AIAA Paper 2016-0534

Guimarães T, Lowe KT, O'Brien WF (2018a) StreamVane turbofan inlet swirl distortion generator: mean flow and turbulence structure. J Propul Power, 34(2):340-353

Guimarães T, Lowe KT, O'Brien WF (2018b) Complex Flow Generation and Development in a Full-Scale Turbofan Inlet. J Eng Gas Turbines Power. https://doi.org/10.1115/1.4039179

Hobson GV, Shreeve RP (1993) Inlet turbulence distortion and viscous flow development in a controlled-diffusion compressor cascade at very high incidence. J Propul Power, 9(3):397-404

Hoopes KM (2013) The StreamVane method: a new way to generate swirl distortion for jet engine research. MS Thesis. Virginia Tech

Klemp JB (1987) Dynamics of tornadic thunderstorms. Annu Rev Fluid Mech, 19:369-402

MacManus DG, Chiereghin N, Gil Prieto D, Zachos PK (2017) Complex aeroengine intake ducts and dynamic distortion. AIAA J, 55(7):2395-2409

Motycka, DL (1976) Ground Vortex-Limit to Engine/Reverser Operation. J Eng Power, 98(2):258-263

Murphy JP, MacManus DG (2011) Ground vortex aerodynamics under crosswind conditions. Exp Fluids, 50:109-124

Murphy JP, MacManus DG, Sheaf CT (2010) Experimental investigation of intake ground vortices during takeoff. AIAA J, 48(3):688-701

Nelson M (2014) Stereoscopic PIV Measurements of Swirl Distortion on a Full-Scale Turbofan Engine Inlet. MS Thesis. Virginia Tech

Nolan D (2001) The stabilizing effects of axial stretching on turbulent vortex dynamics. Phys Fluids, 13(6):1724-1738

Pazur W, Fottner L (1991) The influence of inlet swirl distortions on the performance of a jet propulsion two-stage axial compressor. J Turbomach, 113(2):233-240

Pozrikidis C (2011) Introduction to Theoretical and Computational Fluid Dynamics. Oxford University Press, Oxford

Raffel M, Willert C, Wereley S, Kompenhans J (2007) Particle Image Velocimetry. Springer, Berlin, Heidelberg

Rockwell D (1998) Vortex-Body Interations. Annu Rev Fluid Mech, 30:199-229

Saffman, PG (1992) Vortex Dynamics. Cambridge University Press, Cambridge.

Sanders DD, Nessler CA, Copenhaver WW, List MG, Janczewski TJ (2016) Computational and Experimental Evaluation of a Complex Inlet Swirl Pattern Generation System. AIAA Paper 2016-5008

Schneck WC, Ferrar AM, Bailey JM, Hoopes KM, O'Brien WF (2013) Improved prediction method for the design of high-resolution total pressure distortion screens. AIAA Paper 2013-1133

Schneck WC, Guimarães T, Frohnapfel DJ, Lowe KT, O'Brien WF, Copenhaver WW (2017) Swirling Flow Evolution Part 2: StreamFlow 2D+t Model Validated with Stereo PIV Measurements. AIAA Paper 2017-1622

Seddon J, Goldsmith E (1999) Intake aerodynamics. American Institute of Aeronautics and Astronautics, Washington DC

Sheoran Y, Bouldin B, Krishnan PM (2009) Advancements in the design of an adaptable swirl distortion generator for testing gas turbine engines. ASME Paper GT2009-59146

Sheoran Y, Bouldin B, Krishnan PM (2012) Compressor performance and operability in swirl distortion. J Turbomach, 134(4):041008

Society of Automotive Engineers (SAE) (1978) Gas turbine engine inlet flow distortion guidelines. ARP1420

Society of Automotive Engineers (SAE) (1983) Inlet total-pressure-distortion considerations for gas-turbine engines. AIR1419

Society of Automotive Engineers (SAE) (2017) A methodology for assessing inlet swirl distortion. AIR5686

De Siervi F, Viguier HC, Greitzer EM, Tan CS (1982) Mechanisms of inlet-vortex formation. J. Fluid Mech, 124:173-207

Sonoda T (1987) Experimental Investigation on Spatial Development of Streamwise Vortices in a Turbine Inlet Guide Vane Cascade. ASME Paper 85-GT-20

Wieneke B (2015) PIV uncertainty quantification from correlation statistics. Meas. Sci. Technol. 26(7):074002

Younghans JL, Paul DL (1978) Considerations in inlet engine integration. In: Oates GC (ed) The Aerothermodynamics of Aircraft Gas Turbine Engines, AFAPL-TR-78-52, Air Force Aero Propulsion Laboratory

Zachos PK, MacManus DG, Gil Prieto D, Chiereghin N (2016) Flow distortion measurements in convoluted aeroengine intakes. AIAA J, 54(9):2819-2832

5. Complex Flow Generation and Development in a Full-Scale Turbofan Inlet

The contents of this chapter were published in *ASME Journal of Engineering for Gas Turbines and Power* (Tamara Guimarães, K. Todd Lowe, and Walter F. O'Brien. "Complex Flow Generation and Development in a Full-Scale Turbofan Inlet", *J Eng Gas Turb and Power*. doi: 10.1115/1.4039179).

Significant portions were previously presented as "Tamara Guimarães, K. Todd Lowe, and Walter F. O'Brien. Complex Flow Generation and Development in a Full-Scale Turbofan Inlet. In *ASME IGTI Turbo Expo 2017*, number ASME GT2017-64756, 2017. doi: 10.1115/GT2017-64756".

Paper GTP-17-1545

COMPLEX FLOW GENERATION AND DEVELOPMENT IN A FULL-SCALE TURBOFAN INLET

Tamara Guimarães, K. Todd Lowe and Walter F. O'Brien
Turbomachinery and Propulsion Laboratory, Virginia Tech
Blacksburg, Virginia, USA

ABSTRACT

The future of aviation relies on the integration of airframe and propulsion systems to improve aerodynamic performance and efficiency of aircraft, bringing design challenges, such as the ingestion of non-uniform flows by turbofan engines. In this work, we describe the behavior of a complex distorted inflow in a full-scale engine rig. The distortion, as in engines on a hybrid wing body type of aircraft, is generated by a 21-inch diameter StreamVane, an array of vanes that produce prescribed secondary flow distributions. Data is acquired using stereoscopic particle image velocimetry at three measurement planes along the inlet of the research engine (Reynolds number of 2.6 million). A vortex dynamics-based model, named StreamFlow, is used to predict the mean secondary flow development based on the experimental data. The mean velocity profiles show that, as flow develops axially, the vortex present in the profile migrates clockwise, opposite to the rotation of the fan, and towards the spinner of the engine. The turbulent stresses indicate that the center of the vortex meanders around a preferred location, which tightens as flow gets closer to the fan, yielding a smaller radius mean vortex near the fan. Signature features of the distortion device are observed in the velocity gradients, showing the wakes generated by the distortion screen vanes in the flow. The results obtained shed light onto the aerodynamics of swirling flows representative of distorted turbofan inlets, while further advancing the understanding of the complex vane technology presented herein for advanced ground testing.

NOMENCLATURE

Alphanumeric Symbols

u_z	axial velocity, m/s
u_r	radial velocity, m/s
u_θ	azimuthal velocity, m/s
$\overline{u_i' u_i'}$	normal component of Reynolds stress tensor
$\overline{u_i' u_j'}$	shear component of Reynolds stress tensor
D	duct diameter, m
p_0/p	total-to-static pressure ratio
Q	peak ratio
R	universal gas constant
Re	Reynolds number
T	static temperature, K
γ	specific heat ratio
θ	swirl angle, degrees
ν	kinematic viscosity, m^2/s
ω	normalized vorticity

Abbreviations

BLI	Boundary layer ingestion
CCD	Charge-Coupled Device
CFD	Computational Fluid Dynamics
CFS	Corrected fan speed
DEHS	Di-Ethyl-Hexyl-Sebacate
HWB	Hybrid Wing Body
PIV	Particle Image Velocimetry

INTRODUCTION

A new trend in the pursuit for increasing efficiency and minimizing fuel consumption, emissions and noise in modern aviation is the design and development of new configurations of aircraft that promote integration of airframe and propulsion systems. These aircraft concepts often rely on novel embedded engine configurations that involve fuselage boundary layer ingestion as a means of increasing efficiency. [1-5]

Studies show that boundary layer ingestion (BLI) can reduce aircraft noise, fuel consumption and emissions. The reduction in noise comes from airframe shielding and lower jet velocities [1]. The gains in efficiency come from less propulsion power due to the reduction in drag [2], wake recovery [3] and less kinetic energy wasted [4]. These factors lead to lower fuel burn, reducing fuel consumption as much as 10% [5].

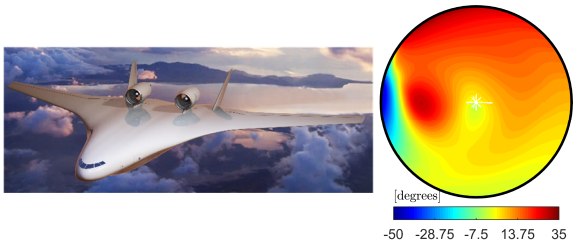

Figure 1 Left: NASA's HWB aircraft concept (Image courtesy of NASA Langley). Right: swirl angle distortion profile resulting of a CFD simulation of the flow in the inlet of an engine in a similar configuration as one on a HWB aircraft.

These novel configurations introduce potential problems in critical regimes of operation, as the ingestion of distorted flows, especially during take-off and landing, can result in adverse conditions for the fan rotor [6]. It is imperative that these distortions are known and their impact fully understood in the initial steps of the aircraft design to ensure satisfactory operability. Total pressure and temperature distortions have been long analyzed [6-10], while swirl distortions, as relevant as they are, have only recently been successfully simulated and analyzed at laboratory and ground testing scales [11-13].

Figure 1 shows a rendering of NASA's Hybrid Wing Body (HWB) aircraft concept, developed as part of the Environmentally Responsible Aviation program, with the main objective of reducing noise and fuel consumption. Experimental results report that this configuration can potentially reduce fuel consumption by more than 50% and improve noise conditions [14]. The swirl angle profile in the inlet of a similar engine configuration as the HWB is also shown in Fig. 1. The profile was obtained from a computational fluid dynamics simulation and shows flow angle distortions ranging from -50 to 30 degrees. The dangers of neglecting such deviations in flow angle include fan stall, performance alteration, and aeromechanical excitation [6,15,16], reinforcing the need to perform an analysis of the behavior of the inlet flow and the response of the engine to strong distortions.

The HWB distortion profile—indicative of airframe vortex ingestion—is the object of the swirl distortion study in this present work. Here, the StreamVane™ technology [13,17] is used to generate a distortion profile inspired by the base distortion features of an extreme flight condition for an experimental design of a HWB engine inlet. Prior findings on StreamVane aerodynamics indicate that the dominant secondary flow dynamics are Reynolds number independent [17,18], and that the generation of the distortions is Mach number independent until vanes choke [19]. For low-speed small-scale wind tunnel experiments of single vortex distortions, secondary flow development is well predicted by inviscid dynamics of axial vorticity [20]. This makes the StreamVane an effective tool in generating distortions. However, there is still a need to describe the behavior of complex distorted flows in full-scale engine applications, especially near the fan.

For this work, stereoscopic particle image velocimetry (PIV) is used to measure three-component velocity fields of the generated flow at three different planes along the inlet of a full-scale research engine. The StreamFlow model is used to predict the secondary flow development based on the experimental data, in order to isolate spinner and fan effects. An analysis of the mean flow and turbulence produced by the distortion screen is presented in the results section to describe leading- and higher-order effects to the flow due to the StreamVane swirl distortion approach and how this flow develops as it approaches the engine fan.

EXPERIMENTAL METHODS

The StreamVane™ method [13,17] is used to generate a pre-defined distortion in the inlet of a Pratt & Whitney Canada JT15D-1 research engine installed at the Virginia Tech Turbomachinery and Propulsion Research Laboratory. Particle image velocimetry is used to acquire three-component velocity fields at three different planes along the inlet of the engine for describing the development of the distorted flow as it approaches the fan in the turbofan engine. Details of the setup will be described in this section.

Computational fluid dynamics results of a simulated flow in the inlet of the engine of a HWB type of aircraft

are used as the starting point for the design of the distortion screen. The secondary velocity profile at the inlet of the engine, presented in Fig. 2 and the swirl angle profile shown in Fig. 1, are used for determining the target profile to be generated by the StreamVane. This profile consists of a clockwise tightly wound vortex at approximately 180 degrees and a bulk counterclockwise swirl. A CAD model of a small-scale version of the screen is generated and printed using additive manufacturing. The small-scale 6-inch version of the StreamVane is tested in a low-speed wind tunnel to ensure that the design is generating the desired profile. Then, after validation of the profile, it is scaled up to the full-scale inlet diameter, 21 inches, and printed to be analyzed in the inlet of the research engine, resulting in the distortion screen shown in Fig. 2. A detailed description of the StreamVane method is presented by Hoopes in [13] and Guimarães in [17].

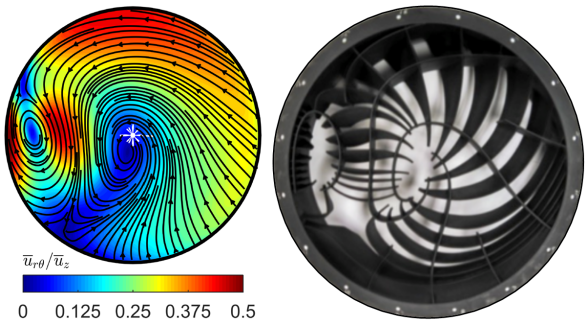

Figure 2 Left: CFD profile of the secondary velocities in the inlet of a HWB turbofan engine. Right: the HWB StreamVane distortion generator based on this profile. [13]

The full-scale experimental setup consists of a bellmouth inlet, tunnel sections connected for inlet flow conditioning, a custom-built rotation stage to house and revolve the StreamVane, a special inlet duct section modified to allow optical access for the PIV cameras and laser sheet entry and exit, and the research engine. The flow is seeded from upstream of the bellmouth by two oil atomizers connected to blowers. Di-Ethyl-Hexyl-Sebacate (DEHS) oil is used for seeding, yielding particles of an average diameter of 1 µm. The axial average bulk velocity of this flow is around 80 m/s (65% CFS), yielding a duct Reynolds number, $Re_D = uD/\nu$ of 2.6 million, based on a duct diameter of 0.53 m and kinematic viscosity ν at 325 K of 1.80×10^{-5} m^2/s.

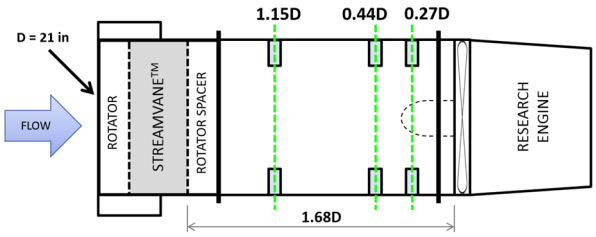

Figure 3 Measurement planes along research engine inlet, located at 1.15, 0.44 and 0.27 diameters upstream of the fan face. The StreamVane is positioned at 1.68 diameters upstream of the fan face.

A double-pulsed 532 nm Nd:YAG laser and two 4-Megapixel LaVision Imager Pro X 4M charge-coupled device (CCD) cameras are used to acquire stereoscopic PIV data at the pre-defined measurement planes, shown in Fig. 3. Details of the camera setup and laser properties are summarized in Tables 1 and 2. The CCD cameras are placed on an aluminum frame attached to brackets on a foundation isolated from the engine mount, and built to minimize vibrations due to the operation of the engine, as can be seen in Fig. 4. The laser head is attached to the same frame, guaranteeing that the cameras and the laser will be subject to the same vibrations. A cylindrical lens connected to the exit of the laser head is used to expand the laser beam into a laser sheet. The laser sheet enters the PIV test section through an acrylic window located at the bottom of the test section and exits through another acrylic window at the top of the section, where measurement plane is labelled in Fig. 4. The PIV test section is also equipped with two 3-mm thick acrylic windows with antireflective coating to allow for optical access for the cameras, which are equipped with Nikon lenses and Scheimpflug adapters to correct the focus of the cameras at the measurement planes. The interior of the test section is painted flat black, and cameras and windows are covered with a black cloth during testing to reduce glare and laser reflection on the windows and tunnel walls. Testing is performed in the open cell after sunset to minimize light saturation on the second time exposure of image pairs.

The instrumentation is stationary and, due to limitations in the field of view of the windows, it is necessary to rotate the StreamVane to obtain a full sweep of the flow inside the 21-inch diameter duct. The measurement volumes are represented by a diagram in Fig. 5. A thousand images are acquired with a 7 μs delay at 4 Hz for each position of the StreamVane, which is rotated 30 degrees counterclockwise between measurements to allow for some overlap in order to improve statistics. The measurements are obtained and processed in LaVision DaVis 8.3.3 and the slices of data

are further processed and stitched together through polar binning [21] in MATLAB.

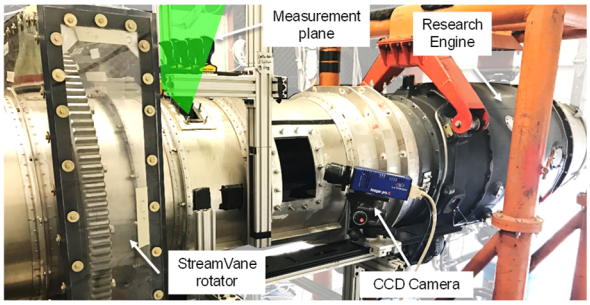

Figure 4 Experimental setup for measurements of the flow on the research engine.

The images are processed using stereo cross-correlation with background subtraction and time filter subtraction based on a Gaussian average of 9 images. Multi-pass processing is used, with the first pass consisting of a square window of 64x64 pixels with a 50% overlap. Then, a square window of 32x32 pixels with 75% overlap is used for the following two passes. The vectors with a peak ratio (the ratio of the largest correlation peak to the second largest peak in an interrogation window) lower than 1.3 are deleted. A built-in median filter is used to remove and replace spurious vectors based upon neighboring vectors. Vectors that do not fall within an interval of the average ± 2 times the standard deviation are removed. Vectors that fall out of a range of ± 30 m/s in the secondary flow directions are deleted, and vectors that have an axial velocity of above 125 m/s are also deleted. The relationship between pixel size and flow space is also presented in Table 2. The spatial resolution corresponds to the size in flow space of the interrogation window in the last pass.

Table 1 Camera properties

Model	CCD size in x and y, pixels	Pixel size, μm^2	Quantum efficiency
LaVision Imager Pro X 4M	2048 x 2048	7.4 x 7.4	0.55

Table 2 Optical setup properties

	Camera Focal Length	Cylindrical Focal Length	Aperture (f-stop)	1 pixel in flow space, mm	Spatial Resolution, mm
1.15D	24 mm	-10 mm	5.6	0.25	8.1
0.44D	24 mm	-10 mm	5.6	0.14	4.4
0.27D	35 mm	-30 mm	1.8	0.11	3.5

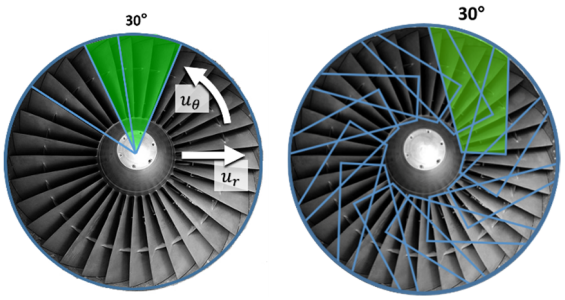

Figure 5 Left: measurement volume for two rotations in the 1.15 and 0.44D planes, and positive orientation of radial and azimuthal velocity components. Right: measurement volume for full rotation in the 0.27D plane

RESULTS AND DISCUSSION

Flow in the inlet of a full-scale research engine is distorted by a 21-inch diameter swirl distortion screen previously designed [13]. The distorted flow, based on the distortion present in the turbofan inlet of a hybrid wing body airframe, is characterized experimentally. The StreamFlow model results are presented to describe the predicted evolution of the secondary flow profile, without engine interactions as core suction, spinner and fan effects. The PIV results obtained are analyzed with two primary objectives in mind: to describe the development of the mean flow along the inlet at full-scale conditions, including interactions with the spinner, and to quantify the higher order effects of the StreamVane to the flow, particularly the axial development of the vane wakes and turbulent stresses introduced into the flow by the distortion device. Near-wall data cannot be collected with PIV due to laser glare and limitations in processing window size, leaving a gap between the outer ring of the plots presented in this section, which represent the duct diameter, and the actual data. To assess the development of the mean flow along the inlet, the mean secondary (in-plane) velocity profiles, normalized by the average bulk axial velocity are presented in Fig. 6. The profile used for designing the StreamVane is also presented for reference, but the 1.15D plane is not to be compared directly to the design for two reasons: the StreamVane method is supposed to generate the design profile right at the exit of the screen, which would be at 1.68D for this experiment, 0.53 diameters upstream of the first measurement plane; and the design profile has inconsistencies in the boundary conditions of some regions that cannot be replicated by the StreamVane, for example, at the lower right region.

The first feature of interest of this flow is the tightly wound vortex, which is very well delimited in all measurement planes. The bulk swirl affects the

generation of the tightly-wound vortex so that, at the 1.15D plane, it is pressed against the tunnel wall and broken into two smaller vortices, around 180 and 210 degrees, as seen in the secondary velocity (Fig. 6) and in the streamwise vorticity profiles (Fig. 7). As the flow develops, the two vortices combine into a single vortex centered around 210 degrees at the 0.44D plane, and then moves clockwise due to its interaction with the wall and the bulk swirl to the 190-degree region in the 0.27D plane. The movement of the vortex can be seen in the constant radii vorticity plots presented in Fig. 8. This behavior is consistent with what is expected due to two-dimensional vortex dynamics, wherein the secondary flow development due to induced velocities from streamwise vorticity may be considered relatively independently from the axial flow, as seen in the StreamFlow model results shown in Fig. 9.

A quantitative examination of the flow velocity magnitudes indicates a loss in the strength of this vortex during the axial development, as well as a reduction in the vortex core diameter, indicating turbulence diffusion in the first case, explained further by the turbulent stresses of the flow. Axial stretching and stabilization from axial acceleration around the spinner explain the increase in streamwise vorticity magnitude for the 0.27D plane. While the 1.15D plane is dominated by the secondary flow, the 0.27D plane is where most of the influence of the spinner and the fan of the engine is observed. The magnitude of the in-plane velocity increases in the 0.27D plane in the region surrounding the spinner due to balancing of mass in the fan/core and the radial velocity increase caused by the spinner. This effect is isolated from the flow development in the delta profiles presented in Fig. 9, where the StreamFlow results (which do not include flow-spinner interactions), are subtracted from the experimental data obtained at each measurement plane downstream of the 1.15D plane. The regions with the highest delta values are the center of the profiles. For the 0.44D plane, that shows the effects of the core suction, and for the 0.27 plane it is clear where the flow observes an increase in radial velocity, near the spinner. As mentioned, differences in the vortex region are due to vortex stretching and meandering.

The mean axial velocity profiles presented in Fig. 10 display a series of features related to structures introduced to the flow by the presence of the StreamVane, since they are not present in the design profile or in clean inlet results presented by Frohnapfel in [22,23]. These features indicate total pressure losses, as previously described by the total-to-static pressure ratios calculated using the following relationship in [17]:

$$\frac{p_0}{p} = \left(1 + \frac{(\gamma - 1)}{2}\frac{(u_z^2 + u_r^2 + u_\theta^2)}{\gamma RT}\right)^{\frac{\gamma}{\gamma-1}}$$

This analysis can be broken down into two main regions of the flow: the near-wall, which is heavily influenced by interactions between the distortion screen and the growing boundary layer from the inlet duct walls, and regions away from the wall. As with the mean in-plane velocity profile, the effects of the distortion screen are more obvious in the 1.15D plane, since it is the first measured plane downstream of the StreamVane (at 0.536 diameters downstream of the device), where regions of axial velocity deficit are present due to the wakes introduced to the flow by the vanes. The 0.44D plot shows an increase of the axial velocity component, since the flow is being accelerated by the fan, and the vane wakes are not distinguishable from the flow anymore due to mixing. At the 0.27D plane, there is a general concentration of momentum toward the core. In contrast to the low momentum diffusive behaviors at 0 – 90°, high momentum regions appear to grow in regions of 240 – 270° and 90 – 150°.

A dynamic analysis of this flow is a next step in understanding the behavior of the tightly-wound vortex. We approach this analysis presuming that the dominant effect of turbulent motions is turbulent diffusion of the secondary flow profile generated immediately downstream of the vanes. A number of factors influence the magnitude of the diffusion, including mixing from wakes of the turning vanes, shear-driven turbulence from velocity gradients in the swirl pattern, and azimuthal stretching due to the bulk swirl induced potential field of the rotor. [21]

The normal components of the Reynolds stress tensor in the axial, $\overline{u_z'u_z'}$, radial, $\overline{u_r'u_r'}$, and azimuthal, $\overline{u_\theta'u_\theta'}$, directions are presented in Figs. 11-13. Overall, the results exhibit turbulence intensities (single-component normalized rms velocities) of up to 15%--the same approximate magnitude as peak values in free shear flows [24]. The axial Reynolds normal stress (Fig. 11) exhibits higher turbulence intensities in the same regions of interest mentioned previously: around the tightly-wound vortex and near the wall. Around the vortex region, the 1.15D plane is subject to higher values of turbulent stresses, as expected, since it is closest to the exit plane of the StreamVane; thus, indicating that the secondary flow is highly unstable there. As the flow develops along the inlet, it is also accelerated, and the vortex is stabilized, leading to reduced turbulence intensities in the 180 – 210° region. The strength of the vortex is also reduced, indicating that the instabilities in the further upstream

planes result in turbulent diffusion of the coherent axial vorticity prior to stabilization. The near wall region shows a growth in turbulent values from the 1.15D to the 0.44D planes due to boundary layer growth, but those values are reduced as the flow accelerates, confining the lowest momentum, highest gradient flow closer to the wall in the 0.27D plane.

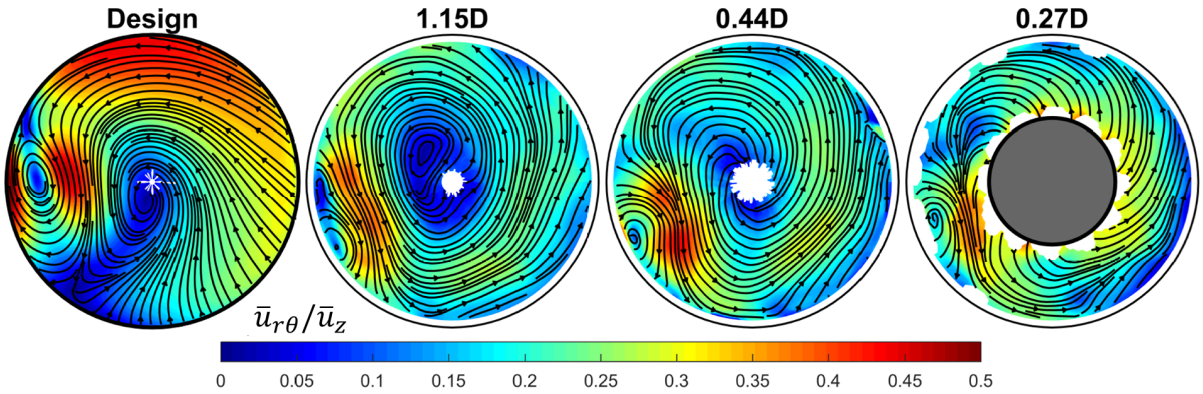

Figure 6 Secondary velocity profile for the design and measurement plane cases. Lines represent the mean direction of the flow and the color plot shows the velocity intensities, normalized by the average bulk axial velocity.

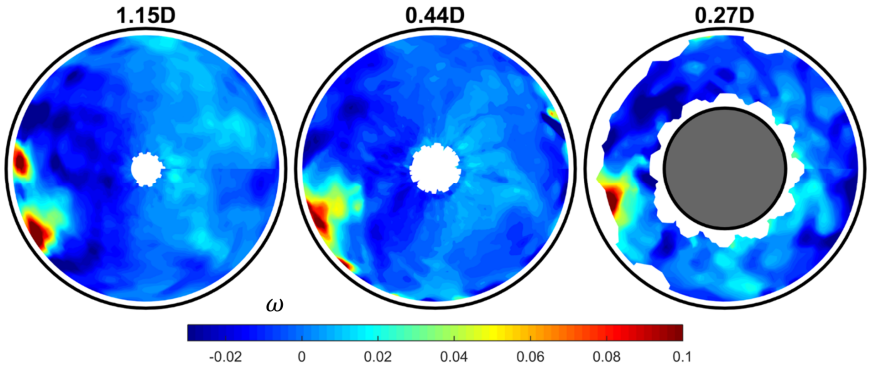

Figure 7 Normalized streamwise vorticity profiles for the measured planes. Vorticity is normalized by duct diameter and average bulk axial velocity.

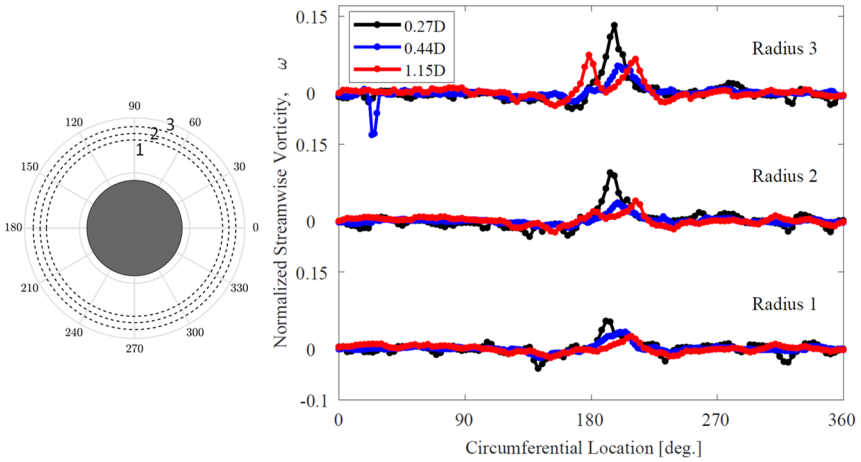

Figure 8 Comparison between the streamwise vorticity at the 0.27D (black), 0.44D (red) and 1.15D (blue) measurement planes at r/R = 0.8 (1), 0.86 (2) and 0.92 (3).

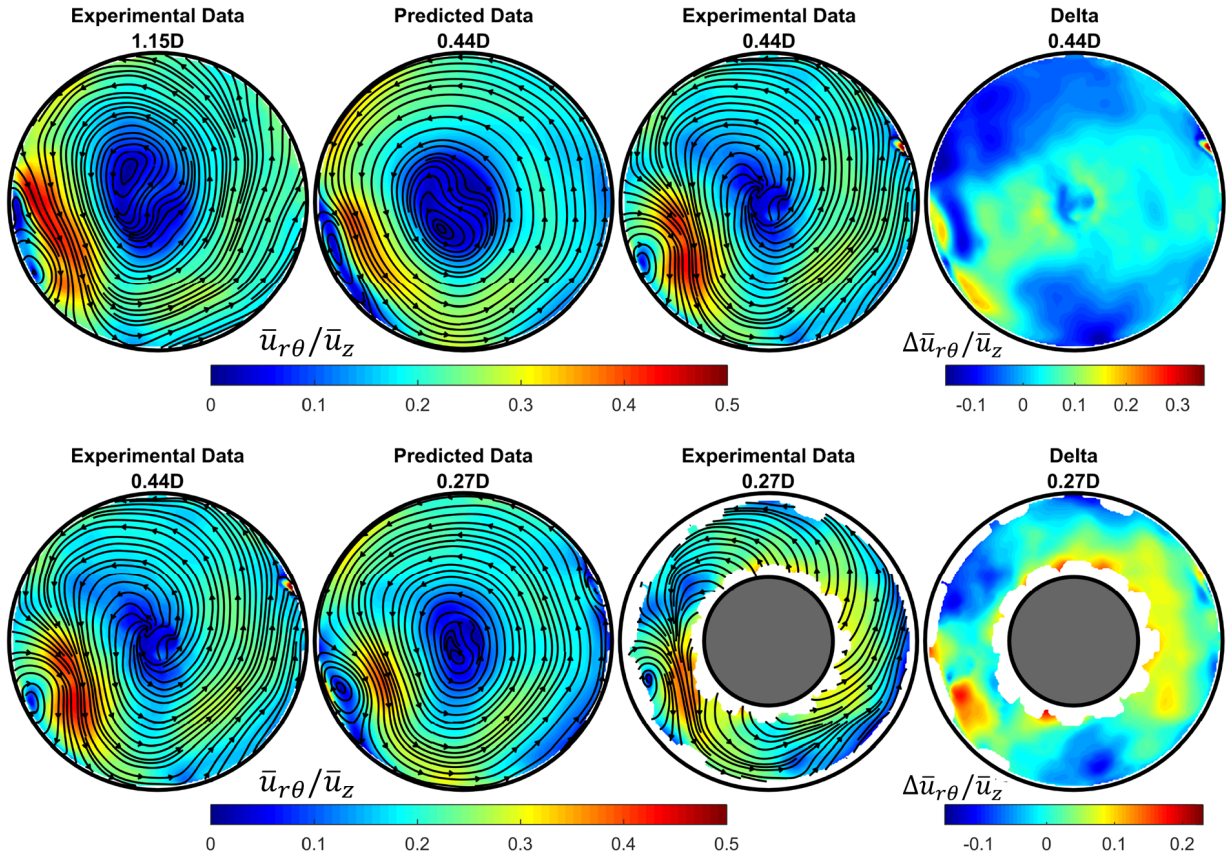

Figure 9 Predicted development of experimental flow at the 1.15D plane (top), and at the 0.44D plane (bottom), using the StreamFlow model [20] compared to the experimental data from the engine.

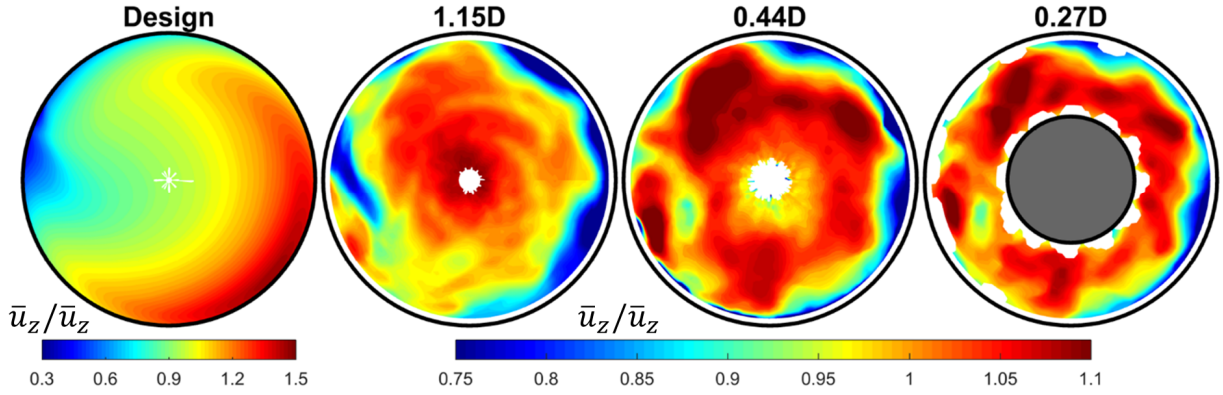

Figure 10 Normalized axial velocity profile. Note different scale between design plot and experimental results, for highlighting present features in both.

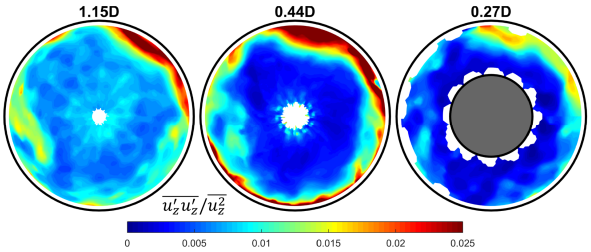

Figure 11 Normal component of the Reynolds stress tensor for the axial velocity $\overline{u_z'u_z'}$, normalized by the axial average bulk velocity, $\overline{u_z^2}$.

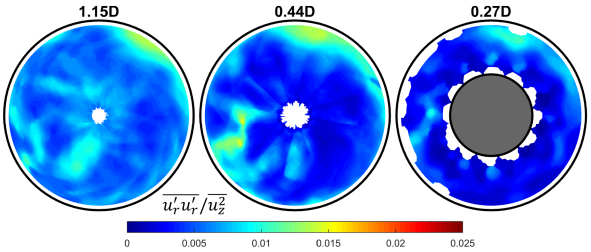

Figure 12 Normal component of the Reynolds stress tensor for the radial velocity $\overline{u_r'u_r'}$, normalized by the axial average bulk velocity, $\overline{u_z^2}$.

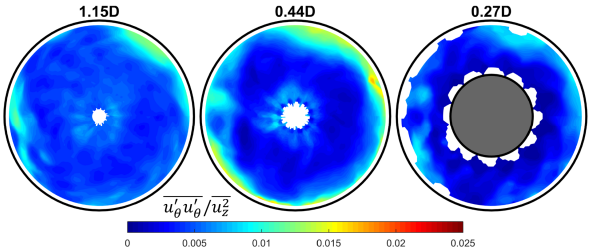

Figure 13 Normal component of the Reynolds stress tensor for the azimuthal velocity $\overline{u_\theta'u_\theta'}$, normalized by the axial average bulk velocity, $\overline{u_z^2}$.

The large scale instabilities of the flow structure are also evident when analyzing the radial and azimuthal components of the Reynolds stress tensor, shown in Figs. 12 and 13. The higher values of the stresses around the vortex region in the 1.15D and 0.44D planes emphasize the fact that the vortex meanders around a preferred core region when influenced by the instabilities of the flow, and that it stabilizes as it approaches the fan face. The near-wall region also presents higher turbulence values, exhibiting inward radial turbulent diffusion of the thick boundary layer and shear layers from the near-wall vanes.

The StreamVane has been shown versatile and effective in generating complex distortion profiles, as the HWB profile presented in this work, single vortex distortions [25], and twin vortex distortions [19,26,27]. It is important, however, to acknowledge that it is a device added to the inlet of the engine, and its influence to the flow needs to be analyzed to ensure that possible adverse effects to the flow are minimized. Vane wake structures present in the 1.15D plane of the axial velocity profile, shown previously in Fig. 10, indicates that the wakes from the StreamVane vanes persist for at least 0.5 diameter downstream of the distortion device. This is also observed in the axial velocity gradients in the radial ($\partial u_z/\partial r$) and azimuthal ($1/r\ \partial u_z/\partial\theta$) directions (Figs. 14 and 15). As with the axial velocity profiles, the vane wakes clearly observed in the 1.15D plane mix and are not discernible anymore at the 0.27D plane. Furthermore, the near wall regions of the axial velocity gradient in the azimuthal direction (Fig. 15) indicate that the distortion screen is responsible for the formation of weak corner vortices, mainly at the 1.15D plane, for instance in the 30° region.

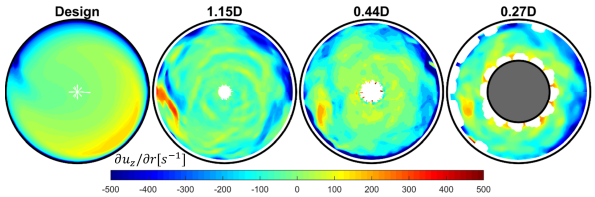

Figure 14 Axial velocity gradient in the radial direction, $\frac{\partial u_z}{\partial r}$.

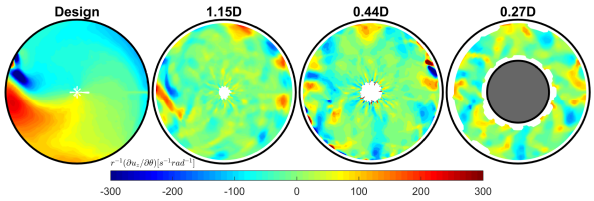

Figure 15 Axial velocity gradient in the azimuthal direction, $\frac{1}{r}\frac{\partial u_z}{\partial\theta}$.

The Reynolds shear stress is examined in regards to understanding how the shear turbulence influences the development of the flow. In plane shear flows, the only terms that contribute to momentum transport are the axial/transverse shear. The physics of the effect can be conceptualized via the Boussinesq approximation for turbulent viscosity [24], indicating that the shear turbulence has a diffusive effect, directly correlated with the local velocity gradients. The Reynolds shear stresses, $\overline{u_i'u_j'}/\overline{u_z^2}$, i ≠ j, presented in Figs. 16-18 exhibit structures that can be related with the ones of the gradients of the axial velocity component presented in Figs. 14 and 15. The 1.15D plane presents lower values for the shear stresses than the other planes, indicating that the turbulence is high in that plane, and that there is not significant coherent motion between the different

velocity components. The shear stresses between the axial and each of the in-plane velocity components in the 0.44D plane (radial-axial, and azimuthal-axial) exhibit the spiral nature of the gradients of axial velocity in the inner regions of the flow, even though these stress values are low when comparing to the near wall region.

The shear stresses in the region of the tightly-wound vortex, combined with the higher values of the normal Reynolds stresses observed in the same region, can be interpreted to indicate an increased diffusion of the vortex in the 1.15D and 0.44D, when compared to a better-stabilized or less-turbulent vortex, and to its behavior at the 0.27D plane.

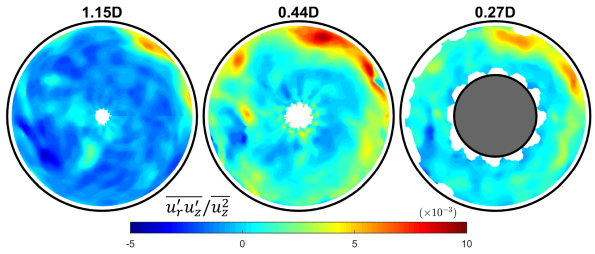

Figure 16 Shear component of the Reynolds stress tensor between the axial and radial velocities $\overline{u_r'u_z'}$, normalized by the axial average bulk velocity, $\overline{u_z^2}$.

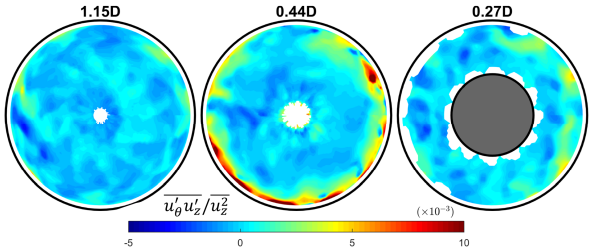

Figure 17 Shear component of the Reynolds stress tensor between the azimuthal and axial velocities $\overline{u_\theta'u_z'}$, normalized by the axial average bulk velocity, $\overline{u_z^2}$.

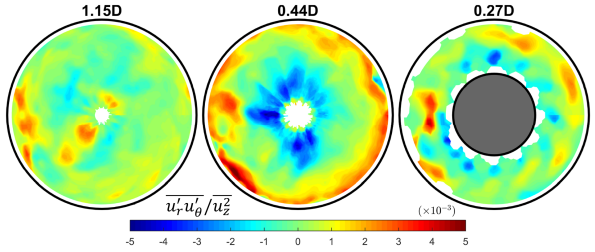

Figure 18 Shear component of the Reynolds stress tensor between the radial and azimuthal velocities $\overline{u_r'u_\theta'}$, normalized by the axial average bulk velocity, $\overline{u_z^2}$.

CONCLUSIONS

A distortion device based on the StreamVane method to generate swirl distortion mimicking the behavior of a hybrid wing body type of aircraft previously designed is analyzed in the inlet of a full-scale P&WC JT15D-1 research engine. Stereoscopic particle image velocimetry measurements are taken at three different planes along the inlet of the engine: 1.15, 0.44 and 0.27 duct diameters upstream of the fan face of the engine. Mean velocity profiles, velocity gradients and turbulent stresses at these locations are analyzed to describe the evolution of the flow along the inlet of the engine and the higher order effects of the distortion screen to the flow.

There are two regions of interest in this flow, which are governed by different fluid dynamics flow components. The first is the tightly-wound vortex, whose behavior can be described based on two-dimensional vortex dynamics, since it is not strongly affected by the axial flow present. As it approaches the engine, the vortex is axially stretched and stabilized by the accelerated flow. The near-wall region is also important and behaves based on boundary layer growth and interactions with the flow governed by the tunnel walls. The 1.15D measurement plane presents high turbulent stress values, indicating that the distortion device introduces large scale instabilities to the flow. As the flow develops and approaches the fan, the effects of the presence of the spinner and the fan are observed, the flow is accelerated and a more coherent motion is achieved.

Understanding the behavior of distorted inflows is crucial to the development of novel aircraft technology and more efficient, distortion-tolerant turbofan engines. Future steps in this work will involve the analysis of more fundamental flows, as single and twin vortices types of distortions, to better describe the physics involved in the distortion device

ACKNOWLEDGMENTS

The authors would like to acknowledge NIA and NASA Langley Research Center for funding this work in association with NASA's Environmentally Responsible Aviation Project (NIA cooperative agreement RD-2917), project managers Fay Collier (LaRC), Hamilton Fernandez (LaRC), Greg Gatlin (LaRC), and Bo Walkley (NIA). An additional thanks to The Boeing Company (POCs: John Bonet and Ron Kawai), Pratt & Whitney (POC: Wes Lord) for the industry perspective on swirl distortion, to Mike Nelson for PIV measurement support, and CAPES for financial support to Tamara Guimarães.

REFERENCES

[1] Gorton, S. A., Owens, L. R., Jenkins, L. N., Allan, B. G., and Schuster, E. P., 2004, "Active flow control on a boundary-layer-ingesting inlet," AIAA Paper No. 2004-1203.

[2] Felder J. L., Kim, H. D., and Brown, G. V., 2009, "Turboelectric distributed propulsion engine cycle analysis for hybrid-wing-body aircraft," AIAA Paper No. 2009-1132.

[3] Smith Jr, L. H., 1993, "Wake ingestion propulsion benefit," J. Prop. and Power, 9(1), pp. 74-82.

[4] Plas, A. P., Sargeant, M. A., Madani, V., Crichton, D., Greitzer, E. M., Hynes, T. P., and Hall, C. A., 2007, "Performance of a boundary layer ingesting (bli) propulsion system," AIAA Paper No. 2007-450.

[5] Owens, L. R., Allan, B. G., and Gorton, S. A., 2006, "Boundary-layer-ingesting inlet flow control," AIAA Paper No. 2006-839.

[6] SAE Aerospace Information Report, 2010, "A methodology for assessing inlet swirl distortion," Society of Automotive Engineers, Warrendale, PA, AIR 5686.

[7] Seddon, J., and Goldsmith, E. L., 1985, Intake aerodynamics, American Institute of Aeronautics and Astronautics; London: Collins Professional and Technical Books, New York.

[8] SAE Aerospace Information Report, 1983, "Inlet Total-Pressure-Distortion Considerations for Gas-Turbine Engines," Society of Automotive Engineers, Warrendale, PA, AIR 1419.

[9] SAE Aerospace Recommended Practice, 1978, "Gas Turbine Engine Inlet Flow Distortion Guidelines", Society of Automotive Engineers, Warrendale, PA, ARP 1420.

[10] Schneck, W., Ferrar, A., Bailey, J., Hoopes, K., and O'Brien, W., 2013, "Improved Prediction Method for the Design of High-Resolution Total Pressure Distortion Screens," AIAA Paper No. 2013-1133.

[11] Genssler, H. P., Meyer, W., and Fottner, L., 1986, "Development of Intake Swirl Generators for Turbo Jet Engine Testing," AGARD Propulsion and Energetics 68th (A) Specialists' Meeting, Munich, Germany, Paper No. AGARD-CP-400.

[12] Sheoran, Y., Bouldin, and B., Krishnan, P.M., 2009, "Advancements in the design of adaptable swirl distortion generator for testing gas turbine engines," ASME Paper No. GT2009-59416.

[13] Hoopes, K.M., "A new method for generating swirl inlet distortion for jet engine research," MS Thesis, Virginia Tech, Blacksburg, Virginia, 2013.

[14] Carter, M.B., Shea, P.R., Flamm, J.D., Schuh, M., James, K.D., Sexton, M.R., Tompkins, D.M., and Beyar, M.D., 2016, "Experimental Evaluation of Inlet Distortion on an Ejector Powered Hybrid Wing Body at Take-off and Landing Conditions," AIAA Paper No. 2016-0010.

[15] Walsh, P.P., and Fletcher, P., Gas Turbine Performance, 2nd ed., Blackwell Science and ASME Press, Fairfield, NJ, 2004.

[16] Sheoran, Y., and Bouldin, B., 2011, "Compressor Performance and Operability in Swirl Distortion," J. Turbomach., 134(4), 041008.

[17] Guimarães, T., Lowe, K.T., and O'Brien, W.F., 2016, "An overview of recent results using the StreamVane method for generating tailored swirl distortion in jet engine research," AIAA Paper No. 2016-0534.

[18] Guimarães, T., Lowe, K.T., Nelson, M., O'Brien, W.F., and Kirk, C., 2015, "Stereoscopic PIV Measurements in a Turbofan Engine Inlet with Tailored Swirl Distortion", AIAA Paper No. 2015-2866.

[19] Sanders, D.D., Nessler, C.A., Copenhaver, W.W., List, M.G., and Janczewski, T.J., 2016, "Computational and Experimental Evaluation of a Complex Inlet Swirl Pattern Generation System," AIAA Paper No. 2016-5008.

[20] Schneck, W.C., Guimarães, T., Frohnapfel, D.J., Lowe, K.T., O'Brien, W.F., and Copenhaver, W.W., 2017, "Swirling Flow Evolution Part 2: StreamFlow 2D+t Model Validated with Stereo PIV Measurements," AIAA Paper No. 2017-1622.

[21] Guimarães, T., Lowe, K.T., Nelson, M., O'Brien, W.F., and Kirk, C., 2015, "Stereoscopic PIV Measurements in a Turbofan Engine Inlet with Tailored Swirl Distortion", AIAA Paper No. 2015-2866.

[22] Frohnapfel, D.J., O'Brien, W.F., Lowe, K.T., 2015, "Fan Response to Inlet Swirl Distortions Produced by Boundary Layer Ingesting Aircraft Configurations," AIAA Paper No. 2015-3804.

[23] Frohnapfel, D.J., Ferrar, A.M., Bailey, J.M., O'Brien, W.F., Lowe, K.T., 2016, "Measurements of Fan Response to Inlet Total Pressure and Swirl Distortions Produced by Boundary Layer Ingesting Aircraft Configurations," AIAA Paper No. 2016-0533.

[24] Pope, S.B., Turbulent Flows, Cambridge: Cambridge Universtiy Press, 2000.

[25] Guimarães, T., Schneck, W.C., Lowe, K.T., O'Brien, W.F., and Copenhaver, W.W., 2017, "Swirling Flow Evolution Part 1: Design and Stereo PIV Measurements at Select Planes," AIAA Paper No. 2017-1620.

[26] Guimarães T., Frohnapfel, D.J., Lowe, K.T., O'Brien, W.F., 2017, "Streamwise Development and Turbulence Characterization of a Twin-Vortex Inlet Distortion for Turbofan Applications," AIAA Paper No. 2017-4992.

[27] Nessler, C. A., Sanders, D. D., List, M. G., Janczewski, T. J., and Copenhaver, W. W., 2017, “Axial Extent of Flowfield Variation from the StreamVane™ Swirl Pattern Generation System,” AIAA Paper No. 2017-1621.

6. Conclusions and Outlook

This present work focused on three different claims regarding the generation and development of inlet swirl distortions making use of a StreamVane™ for turbofan engine applications: the dependence of the swirl on Reynolds and Mach numbers; the driving physics of the development of the vortical flow; and the turbulence characteristics of the studied flows.

6.1 Conclusions

This dissertation comprised three papers that summarize the work developed by the author during her Ph.D. studies. All of the investigations used stereoscopic particle image velocimetry to obtain three-component velocity fields of determined measurement planes in the flow. The first study addressed the mean flow and turbulence characteristics of a complex distorted flow that consisted of a counterclockwise bulk swirl and a clockwise tightly wound vortex. This was experimentally analyzed in two different scales in order to assess the dependence of the generated flow on Reynolds and Mach number. An analysis of the turbulence characteristics of the full-scale flow was performed to describe the influence of the StreamVane distortion generating device to the flow. In the second presented study, a single-vortex distortion was generated with the objective of describing the characteristics of the axial development of a fundamental vortical flow. Velocity field data was taken at discrete measurement planes downstream of the distortion generation in small- and full-scale to describe the dependence of the flow development on Reynolds number, and the physics that drive it. In the final study, the same complex distortion presented in Chapter 3 was evaluated in full-scale. A Pratt & Whitney Canada JT15D-1 turbofan engine was used for the investigation. Data was collected at three discrete measurement planes downstream of the distortion, and upstream of the fan face of the engine. One of the measurement planes was close enough to the fan that its effects on the flow were captured by the measurements. The main objectives of this study were to describe the physics involved in the development of the flow, including its turbulence characteristics.

An analysis of Mach number independence for the flows indicate that, for low Mach number flows, given small perturbations and irrotationality assumptions, the flow angle scaling downstream of the StreamVane is Mach number independent. These assumptions may produce small truncation

errors due to nonlinear potential flow, especially whenever approaching the limit of subsonic flow over the vanes.

Mean flow results of velocity profiles and flow angles indicate that the generation and development of the fundamental vortex and the complex distortion are similar across scales, not depending on the Reynolds number of the flow for the Reynolds number range studied. Details of the StreamVane are responsible for an overshoot in the generation of the full-scale flow angles, and swirl intensity in the flow, but the overall characteristics of the flow are generated with good agreement in both scales.

The axial development of the secondary mean flow is highly driven by two-dimensional vortex dynamics. For both the small- and the full-scale flows far enough upstream of the fan, the vortex convects tangentially in the same direction as its rotation when developing downstream, due to the velocity field induced by the interactions with the duct walls. With the development of the flow, the instabilities around the vortex increase. When approaching the fan, the acceleration of the flow generated by the fan and the core suction affect the behavior of the flow. In this case, the instabilities of the vortex decrease as flow develops due to axial stretching of the vortex lines, which slow down the turbulence development.

Regarding the influence of the StreamVane device to the flow, the flow measured right downstream of the distortion presented regions of high instabilities, mainly due to the wakes generated by the device. These instabilities mixed with the development of the flow and were significantly attenuated at measurement planes over one diameter downstream of the distortion generation. The turbulent length scales of the wakes were on the order of 1/100 of the duct diameter, small when compared to the length scales of the large-scale instability regions of the flow. For the complex distortion, the turbulent field showed to be more dependent on the swirl profile itself than on the turbulent effects added to the flow by the StreamVane. This profile created significant shear flow turbulence in the outer regions of the full-scale flow. When considering the effects of distorted flows to the turbomachinery components, presumed to affect the rotor by introducing bypass transition. Further, the large-scale turbulent fluctuations detected for a tightly wound vortex feature in the profile will produce significant cycle-to cycle variation in loading for individual rotor blades.

The claims that were posed in the beginning of this dissertation have been addressed by the results summarized here. A significant contribution of this work is that investigations of complex inflow distortions can be performed in small-scale wind tunnel environments, decreasing costs associated with full-scale engine tests. To improve these capabilities, it is recommended

that small-scale wind tunnels are equipped with features simulating those of full-scale engines, such as spinners, rotors, and fans. This work has also demonstrated the successful application of PIV to measure distorted flows in the inlet of the VT Turbolab Research engine.

6.2 Outlook

There are several ways to continue developing inlet swirl distortion work based on the findings presented in this work, as follows:

- With the advancements in PIV technology, time-resolved data could be acquired in full-scale engine research facilities, which would contribute even further to the analysis of the turbulent aspects of the distorted flows.
- An investigation of the single-vortex distortion as it approaches and interacts with the fan would aid in further characterizing the axial stretching and stabilization of the vortex, and how that affects the engine performance.
- Investigation of compressible distorted inlet flows and higher Reynolds number flows should be performed to reproduce conditions of real flows in ground-testing facilities and assess the extent of the findings of this work.
- Since it was shown that these swirl distorted flows are Reynolds number independent and the development of the flow is driven by 2D vortex dynamics for the investigated range, small-scale low speed wind tunnels could be adapted to simulate full-scale facilities for more cost-efficient investigations of various distortions.

Appendices

A. Small-Scale Turbulent Analysis for a Twin-Swirl Distortion

The results presented in this section were previously published as "Tamara Guimarães, Dustin J. Frohnapfel, K. Todd Lowe, and Walter F. O'Brien. Streamwise Development and Turbulence Characterization of a Twin-Vortex Inlet Distortion for Turbofan Applications. In *53rd AIAA/SAE/ASEE Joint Propulsion Conference, AIAA Propulsion and Energy Forum*, number AIAA 2017-4992, 2017. doi: 10.2514/6.2017-4992".

A.1 InletA Twin-Swirl StreamVane Experiment

The StreamVane swirl distortion generator used in this investigation was modeled to produce a swirl distortion profile based on NASA's "Inlet-A" ducted turbofan engine concept (Owens et al., 2008; Berrier et al., 2005; Owens et al., 2006; Allan and Owens, 2006; Allan et al., 2006. The secondary flow profile (Figure A.1) consisted of a twin-vortex in the lower hemisphere of the circular outlet plane. Maximum absolute swirl angle in this profile exceeded 12 degrees, radial flow angles in this profile exceeded 20 degrees, and as much as 30% of the local velocity magnitude was directed off the streamwise axis.

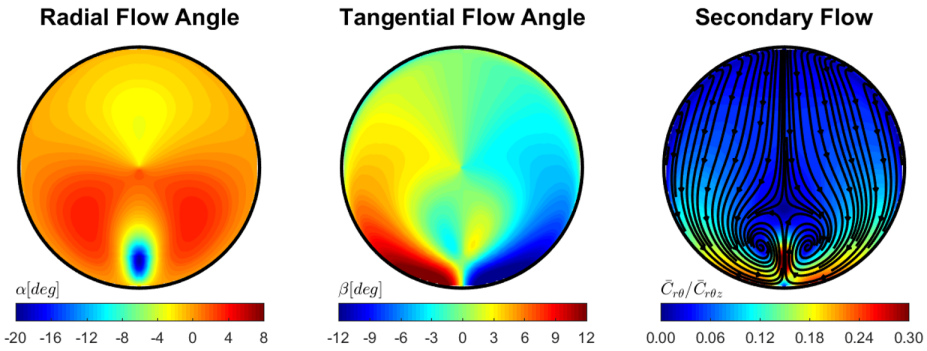

Figure A.1: Target distortion profile produced at the StreamVane trailing edge.

The StreamVane design procedure and the experimental setup were the same as described for small-scale in Chapter 4. Three-component velocity profiles were measured at four discrete measurement planes: 0.25, 0.50, 0.75, and 1.00 diameters downstream of the trailing edge of the StreamVane.

A.2 Experimental Results

The results presented in this section focus on the turbulent aspects of the flow, in order to describe the effects that are generated by the StreamVane. Higher turbulence values were observed in the planes right downstream of the generation of the distortion, but the axial development of the flow promotes mixing, leading to lower values further downstream. This indicates that the effects generated by the StreamVane vanes are negligible to the flow, as long as it is placed enough upstream of the measurement locations. The axial turbulent instensities, turbulent length scales, and the first energy modes of a proper orthogonal decomposition (POD) analysis are presented here to support this claim.

A.2.1 Axial Turbulent Intensity

Data was collected at 4 Hz, which is not as high as is usually preferred for a turbulence analysis, but each plane was sampled 1000 times, guaranteeing enough statistical significance. Axial turbulent intensity was calculated according to the following procedure, and results are presented in Fig. A.2. The root-mean-square of the mean-zero instantaneous axial velocity ($C_z = \widetilde{C}_z - \bar{C}_z$) was computed for the entire data set (Eq. A.1):

$$C_z' = \frac{1}{N}\sum_{i=1}^{N} C_{z_i}^2 \tag{A.1}$$

And then the streamwise turbulence intensity was calculated as the ratio of the RMS fluctuating axial velocity component to the mean axial velocity component (A.2):

$$Tu_z = \frac{C_z'}{\bar{C}_z} \tag{A.2}$$

Overall, the turbulence intensity values ranged from nearly negligible to approximately 7%, while the turbulence intensity decreased in peak magnitude from approximately 6-7% to approximately 4-5% as the flow propagated downstream. This was especially true near the wind-tunnel centerline. Additionally, the coherent wake vortices shed by the turning vanes mixed downstream. This led to the high gradients in turbulence intensity found at the quarter-diameter measurement plane transforming into a nearly uniformly distributed turbulent flow one diameter downstream of

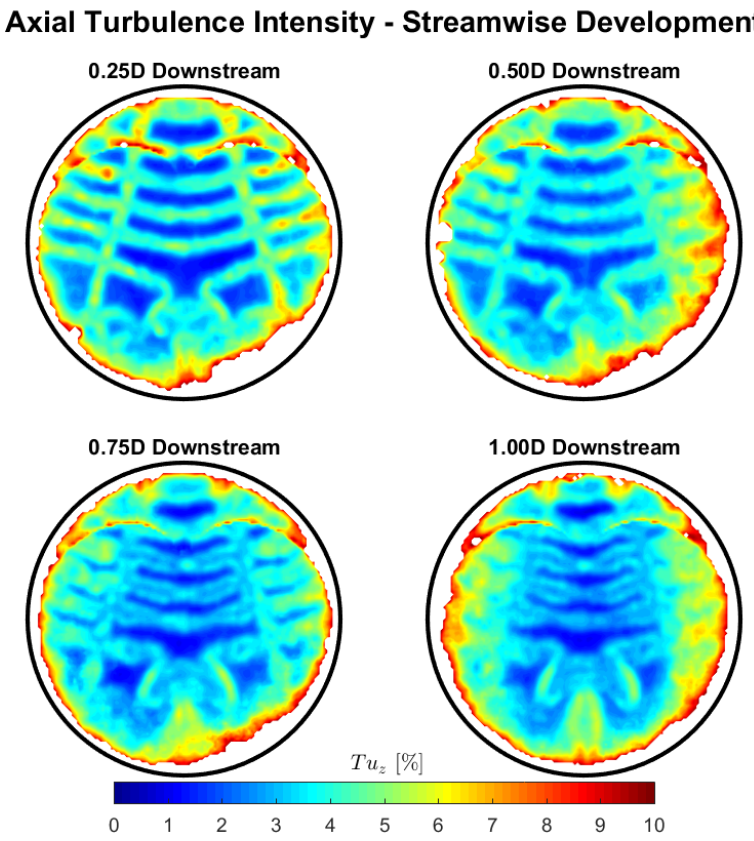

Figure A.2: Axial turbulence intensity.

the StreamVane trailing edge. Areas of high turbulence intensity found near the wall are to be considered artifacts of the experimental setup attributed to laser glare within the clear test section.

A.2.2 Turbulent Length Scales

The turbulent length scales of a flow describe the size of the eddies that are comprised within the flow, characterizing the turbulence in the flow. Two different regions of the flow were chosen for this analysis, to identify the sizes of the eddies related to the wakes of the vanes of the StreamVane, and the eddies related to the twin-vortex feature of the flow, and are highlighted in Figure A.3. The values shown in A.1 were calculated from the correlation maps of a two-point correlation analysis, as described in Bendat and Piersol (2010):

$$L_{horizontal} = \int_0^\infty f(r)dr \qquad L_{vertical} = \int_0^\infty g(r)dr \tag{A.3}$$

Table A.1: Integral length scales for different features of the flow, in millimeters.

		Vane Wake				**Twin-Vortex**			
		0.25D	**0.50D**	**0.75D**	**1.00D**	**0.25D**	**0.50D**	**0.75D**	**1.00D**
Horizontal	C_x	2.9	2.6	2.5	2.9	4.4	4.9	4.4	4.8
	C_y	6.0	2.7	2.1	2.5	2.4	2.4	2.2	2.2
	C_z	7.0	9.2	2.9	3.6	2.9	2.5	1.8	1.6
Vertical	C_x	2.4	2.3	2.3	1.9	2.9	3.1	2.6	2.9
	C_y	4.5	3.0	3.8	3.6	3.1	2.8	2.6	3.0
	C_z	12.2	7.3	3.2	4.9	4.3	4.0	2.4	2.9

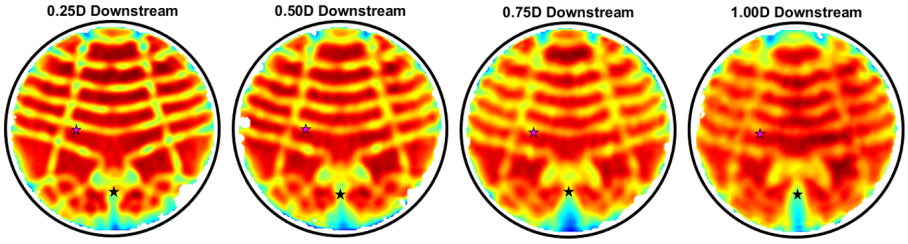

Figure A.3: Regions of reference for two point correlation analysis highlighted in the axial flow.

The most interesting and relevant results of this integral length scale analysis are the ones related to the vane wakes. They are significantly more expressive in the planes right downstream of the StreamVane, 0.25 and 0.50D, and become smaller in the further downstream planes, since the wakes mix with the development of the flow. The velocity component in the x direction, C_x, does not change significantly for any of the cases.

A.2.3 Proper Orthogonal Decomposition (POD)

Proper Orthogonal Decomposition (POD) is a method used to obtain low order models to describe high-dimensional data (Berkooz et. al (1993); Tropea et. al (2007)). POD is commonly used to describe coherent structures in turbulent flows (Lumley (1967); Delville et. al (1999); Holmes et. al (2012)), mainly due to advantages over other classical methods used for large-scale identification and the ability to capture and describe a great amount of the kinetic energy contained in the data (Sirovich (1987); Gordeyev (1999)). For the current analysis, the snapshot POD technique (Ma and Karniadakis (2002); Zhou and Hitt (2011)) was used with the instantaneous PIV image pairs for each measurement plane. With this method, a series of numerical eigenfunctions mathematically described the behavior of the flow. First, the three-dimensional, mean-zero instantaneous velocity

components were calculated. Next, the autocovariance matrix was computed (A.4), where K is the autocavariance matrix, x_i is the data matrix, and x_i^T is the transpose of the data matrix.

$$K = \frac{1}{T}\int_0^T x_i(t)x_i^T(t)dt \tag{A.4}$$

The autocovariance matrix, K, was then represented by an eigenvalue problem (A.5), where u_i is an eigenvector equivalent to the POD mode and λ_i is the eigenvalue equivalent to the POD mode energy.

$$Ku_j = \lambda_j u_j \tag{A.5}$$

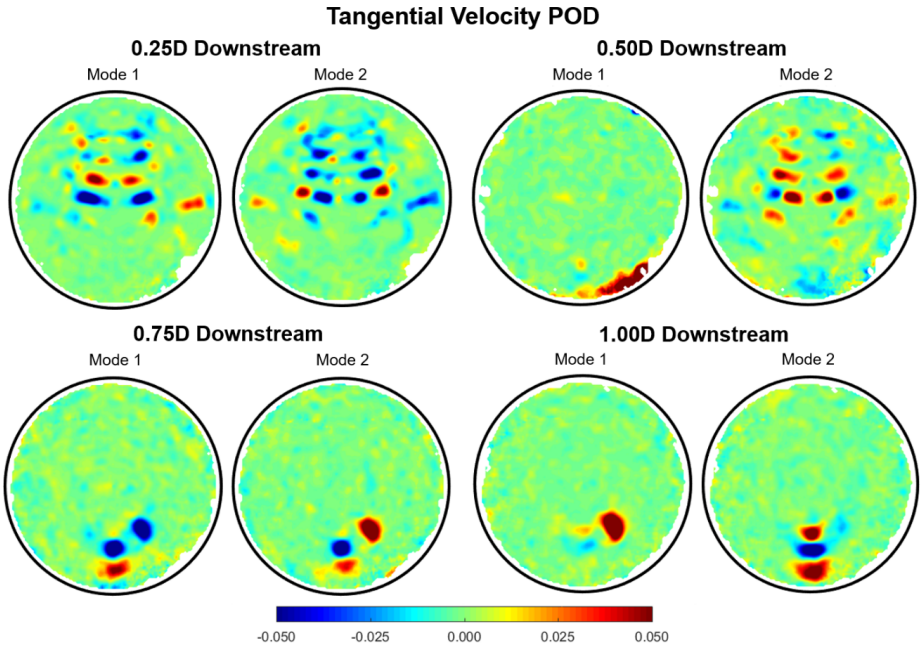

Figure A.4: Contours of the first two POD modes of the tangential velocity component for all measurement planes.

The results for tangential velocity, shown in Figure A.4, and the radial velocity, Figure A.5, indicate a significant contribution of the turbulence introduced by the vane wakes in the planes closest to the trailing edge of the StreamVane, with clear coherent structures in the regions downstream of the vanes, while the 0.75D and 1.00D planes show coherent structures yielding from the large scale motions related to the interactions between the twin vortices.

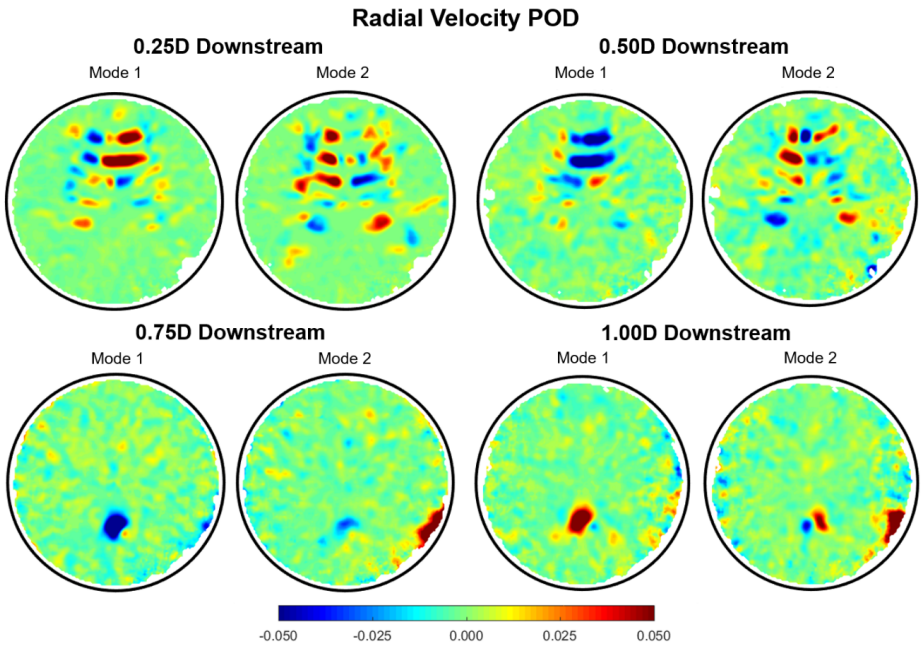

Figure A.5: Contours of the first two POD modes of the radial velocity component for all measurement planes.

Nomenclature

$\tilde{C}_z$	instantaneous axial velocity
$\bar{C}_z$	mean axial velocity
C'_z	root-mean-square (RMS) axial velocity
C_z	zero-mean instantaneous axial velocity
K	autocorrelation matrix
$L_{horizontal}$	horizontal turbulence length scale
$L_{vertical}$	vertical turbulence length scale
t	time
T	integral time scale
Tu_z	axial turbulent intensity
u	eigenvector, POD mode
λ	eigenvalue, POD mode

References

B. Allan and L. Owens. Numerical Modeling of Flow Control in a Boundary-Layer-Ingesting Offset Inlet Diffuser at Transonic Mach Numbers. In *44th AIAA Aerospace Sciences Meeting and Exhibit*, number AIAA 2006-845, 2006.

B. Allan, L. Owens, and J. Lin. Optimal Design of Passive Flow Control for a Boundary-Layer-Ingesting Offset Inlet Using Design-of-Experiments. In *44th AIAA Aerospace Sciences Meeting and Exhibit*, number AIAA 2006-1049, 2006.

J. S. Bendat, A. G. Piersol. *Random Data: Analysis and Measurement Procedures*. John Wiley & Sons, New York, 2010.

G. Berkooz, P. Holmes, J. L. Lumley. The Proper Orthogonal Decomposition in the Analysis of Turbulent Flows. *Annual Review of Fluid Mechanics*, 25:539-575, 1993.

B. L. Berrier, M. B. Carter, and B. G. Allan. High Reynolds Number Investigation of a Flush-Mounted, S-Duct Inlet With Large Amounts of Boundary Layer Ingestion. Technical Report NASA/TP-2005-213766, 2005. URL http://ntrs.nasa.gov/search.jsp?R=20060006399.

J. Delville, L. Ukeiley, L. Cordier, J. P. Bonnet, M. Glauser. Examination of Large-Scale Structures in a Turbulent Plane Mixing Layer, Part 1: Proper Orthogonal Decomposition. *Journal of Fluid Mechanics*, 391:91-122, 1999.

S. Gordeyev. *Investigation of Coherent Structure in the Similarity Region of the Planar Turbulent Jet using POD and Wavelet Analysis.* PhD thesis, University of Notre Dame, 1999.

P. Holmes, J. L. Lumley, G. Berkooz, C. W. Rowley. *Turbulence, Coherent Structures, Dynamical Systems, and Symmetry*. Cambridge University Press, Cambridge, England, 2012.

J. L. Lumley. The Structure of Inhomogeneous Turbulent Flows, in *Atmospheric Turbulence and Radio Propagation*, Moscow: Nauka, pp. 166–178, 1967.

X. Ma, G. E. Karniadakis. A Low-Dimensional Model for Simulating Three-Dimensional Cylinder Flow. *Journal of Fluid Mechanics*, 4588:181-190, 2002.

L. Owens, B. Allan, and S. Gordon. Boundary-layer-ingesting flow control. In *44th AIAA Aerospace Sciences Meeting and Exhibit*, number AIAA 2006-839, 2006.

L. R. Owens, B. G. Allan, and S. A. Gorton. Boundary-Layer-Ingesting Inlet Flow Control. *Journal of Aircraft*, 45(4):1431–1440, 2008.

L. Sirovich. Turbulence and the Dynamics of Coherent Structures. *Quarterly of Applied Mathematics*, 45:561-590, 1987.

C. Tropea, A. Yarin, J. F. Foss. *Springer Handbook of Experimental Fluid Mechanics*. Springer-Verlag, Berlin Heidelberg, Germany, 2007.

X. Zhou, D. L. Hitt. Proper Orthogonal Decomposition Analysis of Coherent Structures in Simulated Reacting Buoyant Jets. *AIAA Journal*, 49:945-952, 2011.

B. Particle Image Velocimetry in Engine Inlets

This appendix summarizes the experimental methods used for measuring distorted flows with particle image velocimetry (PIV) in the inlet of the Pratt and Whitney Canada JT15D-1 research engine located at the Virginia Tech Turbomachinery and Propulsion Research Laboratory.

B.1 Experimental Setup

The full-scale experiments in this work were performed in the inlet of a research engine, shown in Figure B.1. The test rig is comprised of a bellmouth and tunnel sections bolted together to form the inlet for inflow treatment (not shown in figure), a customized PIV test section with optical access, two seed distribution devices, the stereoscopic PIV system (cameras and laser), and the StreamVane mounted in a rotator to allow for measurements across the entire diameter of the inlet.

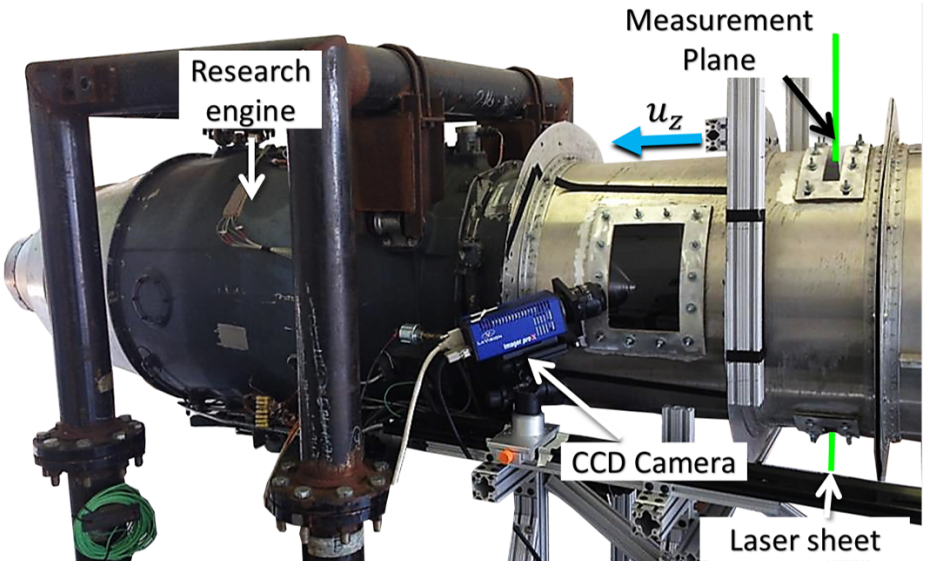

Figure B.1: Full-scale experimental setup.

The PIV test section contains four windows: two for camera access and two for laser entry/dump. For the windows, optically clear, cast acrylic (3 mm thickness for camera windows, and 2 mm thickness for laser windows) with antireflective coating was compressed between layers of sheet metal, and bolted in place using nut plates riveted to the tunnel wall. Weather stripping acts as a gasket to provide sealing. Cameras and windows were shrouded with a black cloth during

testing to reduce glare on the windows. Additionally, since the test cell is open to the outside environment, testing was performed after sunset to minimize light saturation in the second time exposure of image pairs. The spinner and the inside of the tunnel sections were spray painted flat black to minimize glare and laser reflections. Cameras and laser were mounted on an aluminum frame bolted to a metal rail, designed to minimize the movement of the cameras and the laser relative to the test rig.

The flow was seeded by different seeding devices, depending on the experiment. For the experiments in Chapters 3 and 5, two seeders with Di-Ethyl-Hexyl-Sebacate (DEHS) were used, while for Chapter 4, a single Concept Engineering Ltd Colt 4 seeder with Fluid A (glycerol + water) was used. To ensure that particles would follow the flow streamlines, particularly when passing over the StreamVane vanes, they must have Stokes numbers lower than 1, which can be calculated using Equations B.1 and B.2 (Raffel et al., 2007):

$$Stk = \frac{\tau_s u_s}{l_s} \tag{B.1}$$

$$\tau_s = d_p^2 \frac{\rho_p}{18\mu} \tag{B.2}$$

where τ_s is the relaxation time, u_s is the fluid velocity, l_s is the characteristic dimension of the obstacle, d_p is particle diameter, ρ_p is particle density, and μ is the dynamic viscosity of the fluid in which the particles are inserted. Using standard conditions for dry air, and a mean particle diameter of 0.3 μm for both the DEHS and Fluid A particles, and particle densities of 914 kg/m^3 for DEHS (LaVision, 2018; Fischer Scientific, 2018), and 1262 kg/m^3 for Fluid A (Concept Engineering, 2018), the calculated Stokes numbers ranged from 0.0043 for the full-scale experiment with Fluid A, to 0.025 for the small-scale experiment with small-scale experiment with Fluid A. These results are below the limit of a Stokes number of 1, meaning that the particles should follow the streamlines of the flow.

B.1.1 Calibration

Calibration of the camera images was performed to correlate the camera pixel size to the actual real world size of the particle displacement. This was done by removing the top laser window, and clamping the calibration plate to a custom made aluminum mount. A flashlight was used to

illuminate the calibration plate inside the dark tunnel, and calibration was performed through the calibration dialogue on LaVision DaVis. The calibration setup is presented in Figure B.2, and calibration results are presented in each chapter in the experimental methods section.

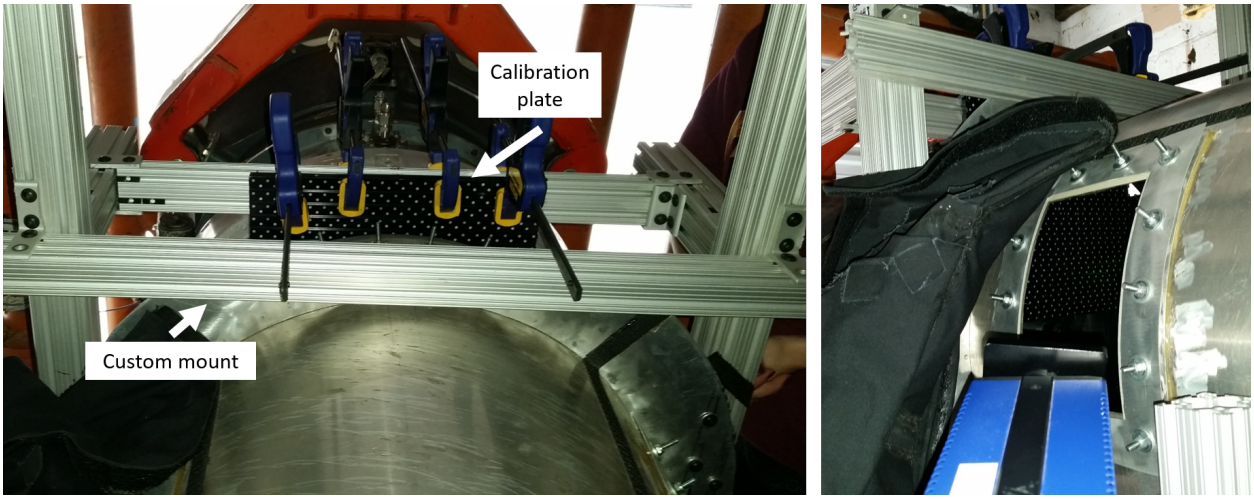

Figure B.2: Calibration setup.

B.1.2 Data Collection

Due to the large diameter of the engine inlet, 0.534 m (21 inches), it was not possible to collect flow data across the entire diameter all at once. To address this issue, the StreamVane was mounted on a custom built rotator which allowed for slices of data to be collected one at a time. The number of images collected was high enough to ensure statistical significance of the mean data results, and is presented in each chapter. The StreamVane was rotated by 30 degrees between each collection position to ensure overlap of the data sets for ease of post-processing and improved data statistics. The position of the laser sheet depended on the measurement plane: for measurement planes upstream of the fan, the data was collected in the top center slice of the inlet diameter, as shown in Figure B.3 left; for the measurement plane that intersected with the spinner, the laser sheet was positioned to the right of the spinner, as shown in Figure B.3 right. The use of the rotator simplified the procedure of acquiring data in the engine inlet, since the StreamVane could be rotated between measurement positions while the engine was running. However, it was still necessary to shut down the engine after every three or four measurement positions to clean the acrylic windows due to seed deposition.

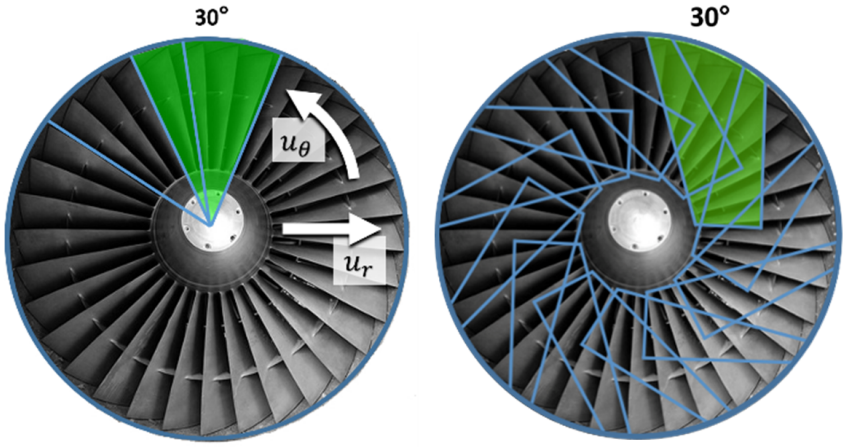

Figure B.3: Data measurement positions.

B.1.3 Data Processing

Once all data was collected, it was processed using stereoscopic cross-correlation on LaVision DaVis. The steps of processing are described in each Chapter due to slight differences in measurement location and data quality. The processed data was exported and further processed on MATLAB. A detailed description of the stitching algorithm used to generate the full diameter plots of data measurements is presented in section 3.2.4 in Chapter 3.

B.1.4 PIV Uncertainties

PIV uncertainty may be affected by several variables in an experimental setup, such as shear, displacement, seeding density, particle diameter, system calibration, timing errors, as well as other systematic and random sources (Raffel et al., 2007). Therefore, quantifying PIV uncertainties can be extremely challenging, and there are several studies that aim at addressing this, such as Nobach and Bodenschatz (2009); Kähler et al. (2012); and Wieneke (2015). DaVis LaVision software calculates uncertainties based on correlation statistics, as described by Wieneke (2015).

Nelson (2014) performed an extensive investigation on the repeatability and influence of external factors such as vibration in the uncertainties of this experimental setup, concluding that those are small, and the uncertainty of the measurements can be estimated by the uncertainties in the particle displacement. To estimate uncertainties in the velocity measurements, the fundamental PIV calculation of velocity was considered:

$$V_p = \frac{\Delta x_p}{\Delta t} \tag{B.3}$$

$$\delta(V_p) = \frac{\partial(\Delta x_p)}{\Delta t} \tag{B.4}$$

where Δx_p is the displacement of particles, and Δt is the time delay between the double-pulsed PIV image frames. To improve the accuracy of particle the particle displacement beyond the resolution of the optical sensors, several image processing techniques that use sub-pixel interpolations have been used (Nobach and Bodenschatz, 2009), yielding an achievable accuracy of 0.1 pixel in ideal conditions. Using the scale factor calculated by the software calibration, it was possible to determine the uncertainty in the particle displacement, assuming no uncertainty in the time delay. Each chapter presents the obtained values in the experimental methods section.

With this approach, the uncertainties obtained in the PIV measurements are dependent on the spatial resolution achieved with the particular experimental setup, ranging from 0.85% of the small-scale experiment bulk velocity to 3.5% of the full-scale experiment bulk velocity. These values may seem high, but are well within the expected for PIV experiments, and even despite higher than what might be achieved locally with other measurement techniques, such as point measurements like pressure probes, doppler global velocimetry (DGV) (Komine, 1990; Meyers et al., 2001), or laser doppler velocimetry (LDV) (Albrecht et al., 2002), the benefit of the spatial resolution obtained by PIV overcomes those differences.

Nomenclature

d_p	particle diameter
l_s	characteristic dimension of the obstacle
Stk	Stokes number
u_s	fluid velocity of the flow
u_z	streamwise velocity
V_p	particle velocity
$\delta(.)$	uncertainty in a given quantity
μ	viscosity
ρ_p	particle density

τ_s relaxation time
Δt time delay between image frames
Δx_p particle displacement between image frames

References

H. E. Albrecht, M. Borys, N. Damaschke, and C. Tropea. *Laser Doppler and Phase Doppler Measurement Techniques*. Springer, 1 edition, 2002.

Concept Engineering. Standard Range of Smoke Generating Systems, Health and Safety Data. June, 2015.

Fisher Scientific. Bis(2-ethylhexyl) sebacate, 97%, ACROS Organics. Accessed on April 2 2018. URL: https://www.fishersci.com/shop/products/bis-2-ethylhexyl-sebacate-97-acros-organics-3/p-4510075.

C. J. Kähler, S. Scharnowski, and C. Cierpka. On the uncertainty of digital PIV and PTV near walls. *Experiments in Fluids*, 52(6):1641-1656, 2012. doi: 10.1007/s00348-012-1307-3.

H. Komine. System for measuring velocity field of fluid flow utilizing a laser-doppler spectral image converter. US Patent Office, 1990.

LaVision. Seeding Particles. Accessed on April 2 2018. URL: https://www.lavision.de/en/applications/fluid-mechanics/piv-system-components/seeding-particles/.

J. F. Meyers, J. W. Lee, and R. J. Schwartz. Characterization of measurement error sources in Doppler global velocimetry. *Measurement Science and Technology*, 12(4):357-368, 2001. doi: 10.1088/0957-0233/12/4/301.

M. Nelson. Stereoscopic PIV Measurements of Swirl Distortion on a Full-Scale Turbofan Engine Inlet. Master's Thesis, Virginia Tech, 2014.

H. Nobach and E. Bodenschatz. Limitations of accuracy in PIV due to individual variations of particle image intensities. *Experiments in Fluids*, 47(1):27-38, 2009. doi: 10.1007/s00348-009-0627-4.

M. Raffel, C. Willert, S. Wereley, and J. Kompenhans. *Particle Image Velocimetry: A Practical Guide*. Springer Berlin Heidelberg, 2 edition, 2007. ISBN 978-3-540-72307-3. doi: 10.1007/978-3-540-72308-0.

B. Wieneke. PIV uncertainty quantification from correlation statistics. *Measurement Science and Technology*, 074002:7-10, 2015. doi: 10.1088/0957-0233/26/7/074002.